NASA
CR
3147-
pt.2
c.1

LOAN COPY: RETU
AFWL TECHNICAL
KIRTLAND AFB, N

0061811

TECH LIBRARY KAFB, NM

NASA Contractor Report 3264

Numerical Method for Predicting Flow Characteristics and Performance of Nonaxisymmetric Nozzles

Part 2 - Applications

P. D. Thomas

CONTRACT NAS1-15084
OCTOBER 1980

NASA

TECH LIBRARY KAFB, NM

0061811

NASA Contractor Report 3264

Numerical Method for Predicting Flow Characteristics and Performance of Nonaxisymmetric Nozzles

Part 2 - Applications

P. D. Thomas
Lockheed Missiles and Space Company, Inc.
Palo Alto, California

Prepared for
Langley Research Center
under Contract NAS1-15084

National Aeronautics
and Space Administration

Scientific and Technical
Information Branch

1980

CONTENTS

Section		Page
1	INTRODUCTION	1
2	MODIFICATIONS TO THE NUMERICAL METHOD	3
	2.1 Brief Outline of the Original Formulation	3
	2.2 Modified Formulation of the Implicit Algorithm	7
	2.3 Modified Scheme for Subsonic Inflow and Outflow Boundary Conditions	12
	2.3.1 Inflow Boundary Points	12
	2.3.2 Outflow Boundary Points	12
	2.4 Implicit Dissipation	13
	2.5 Improved Numerical Grid Generation Technique	16
3	EVALUATION OF NOZZLE THRUST AND DISCHARGE COEFFICIENT	23
	3.1 Thrust	23
	3.2 Discharge Coefficient	27
4	FINAL FORMULATION OF TURBULENCE MODELS	29
	4.1 Two-Dimensional and Axisymmetric Flows	30
	4.1.1 Wall Boundary Layers	32
	4.1.2 Wakes	36
	4.1.3 Mixing Layers and Fully-Developed Jet Region	38
	4.2 General Three-Dimensional Flows	40
5	NUMERICAL EXPERIMENTS	43
	5.1 Computation of Separated Flow	43
	5.2 Effect of Implicit Boundary Conditions and Time Stepsize on the Solution	51
	5.2.1 Implicit Boundary Conditions	51
	5.2.2 Time Stepsize	53
	5.3 Effect of Artificial Explicit Smoothing on the Solution	62
	5.4 Effect of Artificial Implicit Dissipation on Stability and Convergence	64
	5.5 Conclusions	71

Section		Page
6	NOZZLE FLOWFIELD PREDICTIONS AND COMPARISON WITH EXPERIMENTAL DATA	73
	6.1 Internal Flow in a "Two-Dimensional" Converging-Diverging Nozzle	73
	6.1.1 Configuration, Operating Conditions, and Computational Grid	73
	6.1.2 Two-Dimensional Flow Results	79
	6.1.3 Three-Dimensional Flow Results	91
	6.2 Internal and External Flowfield of a Circular Nozzle	98
	6.2.1 Configuration, Operating Conditions, and Computational Grid	98
	6.2.2 Numerical Results	104
7	REFERENCES	113

Section 1
INTRODUCTION

This report summarizes work performed during the second phase of an effort to develop a computer-implemented numerical method for predicting the flow characteristics and performance of three-dimensional jet engine exhaust nozzles. The objective of developing a method for computing the internal and external viscous flowfield of an isolated nozzle has been met. The approach is based on using an implicit numerical method to solve the unsteady Navier-Stokes equations in a boundary-conforming curvilinear coordinate system to obtain the desired time-asymptotic steady state solution. Flow turbulence effects are simulated by means of algebraic turbulence models for the effective turbulent eddy viscosity and Prandtl number. A detailed description of the equations and boundary conditions and of the numerical method have been presented in an earlier report [Ref. 1], along with a general discussion of turbulence models appropriate to the various sub-regions of the nozzle flowfield.

The present final report describes work performed since Reference 1 was written. Recent modifications and improvements to the original numerical algorithm are presented in Section 2. Section 3 gives the equations that are used to derive the nozzle performance parameters such as thrust and discharge coefficient from the computed flowfield data. The final formulation of the turbulence models that are used to simulate flow turbulence effects is presented in Section 4. Section 5 presents the results of numerical experiments performed to explore the effect that various parameters in the numerical method have on both the rate of convergence to steady state and on the final flowfield solution. Detailed flowfield predictions for several three-dimensional nozzle configurations are presented in Section 6 and compared with experimental wind tunnel data.

The numerical method is embodied in a set of three computer codes: RGRIDD, NOZLIC, and NOZL3D. The RGRIDD code constructs the curvilinear coordinate

system and computational grid numerically for nozzles of complex geometric configuration. The NOZLIC code generates a set of flowfield initial conditions on this grid that are used to start a flow computation. The NOZL3D code performs the actual flowfield computation and evaluates the nozzle performance characteristics. A user's guide to the operation of these three codes is contained in a separate volume [Ref. 8].

In the sections that follow, all equations are cast in dimensionless form. Distances are referred to a reference length, velocities are referred to the speed of sound at some reference state, viscosity μ is referred to the molecular viscosity at the reference state, and individual state variables such as density ρ, pressure p, and temperature T are referred to their values at the reference state. The reference state is that at which the Reynolds number Re is defined in terms of the reference length using the reference sound speed as the characteristic velocity.

Section 2
MODIFICATIONS TO THE NUMERICAL METHOD

2.1 BRIEF OUTLINE OF THE ORIGINAL FORMULATION

The original formulation of the numerical method [Ref. 1] starts with the strong conservation-law form of unsteady Navier-Stokes equations in a Cartesian base coordinate system (x y z). The equations are transformed to a boundary-conforming curvilinear coordinate system (ξ,η,ζ), and take the non-dimensional form

$$\hat{q}_\tau + \hat{f}_\xi + \hat{g}_\eta + \hat{h}_\zeta = Re^{-1}(\hat{\theta}_\eta + \hat{\omega}_\zeta) \tag{2.1}$$

where $$\hat{q} = J\vec{q} \tag{2.2}$$

J is the Jacobian of the inverse transformation

$$J = \partial(x,y,z)/\partial(\xi,\eta,\zeta) \tag{2.3}$$

$\vec{q}$ is a vector of conserved variables whose components are the density, the three Cartesian components of the momentum flux vector $\rho\vec{V}$, and the total energy per unit volume, $\hat{f}$, $\hat{g}$, and $\hat{h}$ are inviscid flux vectors; and the terms on the R.H.S. of Eq. (2.1) that are inversely proportional to the Reynolds number Re represent viscous transport processes. Each of the inviscid flux vectors is a linear combination of the flux vectors $\vec{f}$, $\vec{g}$, $\vec{h}$ associated with the Cartesian coordinate direction x, y, z, respectively. The coefficients of these linear combinations are the metrics of the coordinate transformations $\xi(x,y,z,t)$, $\eta(x,y,z,t)$, $\zeta(x,y,z,t)$. For example,

$$\hat{f} = \hat{\xi}_t \vec{q} + \hat{\xi}_x \vec{f} + \hat{\xi}_y \vec{g} + \hat{\xi}_z \vec{h}$$

$$\hat{\xi}_x = J\,\xi_x = y_\eta z_\zeta - y_\zeta z_\eta$$

$$\hat{\xi}_y = J\,\xi_y = z_\eta x_\zeta - z_\zeta x_\eta$$

etc.

The non-dimensional flow variable vector $\vec{q}$ and the inviscid flux vectors $\vec{f}, \vec{g}, \vec{h}$ are defined as follows in terms of the Cartesian components u, v, w, the density ρ, the pressure p, and the total energy per unit volume ε:

$$\vec{q} = (\rho, \rho u, \rho v, \rho w, \varepsilon)^T$$

$$\vec{f} = [\rho u, p' + \rho u^2, \rho uv, \rho uw, u(p' + \varepsilon)]^T$$

$$\vec{g} = [\rho v, \rho vu, p' + \rho v^2, \rho vw, v(p' + \varepsilon)]^T$$

$$\vec{h} = [\rho w, \rho wu, \rho wv, p' + \rho w^2, w(p' + \varepsilon)]^T$$

where $p' = p/\gamma$ and γ is the specific heat ratio.

Similarly, each of the viscous terms $\hat{\theta}, \hat{\omega}$ is a linear combination of the viscous terms associated with each of the Cartesian coordinate directions. The reader is referred to Section 2 of Reference 1 for the mathematical equations that define the viscous terms. We note only that Eq. (2.1) represents the parabolic approximation to the Navier-Stokes equations wherein viscous terms associated with the streamwise coordinate ξ are neglected.

To solve Equation (2.1), the transformed space (ξ, η, ζ) is covered by a uniform grid $(\xi_j, \eta_k, \zeta_\ell)$ such that peripheral grid points lie on the boundaries of the space. The spatially differenced form of the equations is derived to second order accuracy in the mesh spacings $\Delta\xi, \Delta\eta, \Delta\zeta$ by means of the Finite-Volume Method. To each interior grid point of the transformed space there corresponds a cell of volume $\Delta V = \Delta\xi\, \Delta\eta\, \Delta\zeta$ that encloses the point. The difference equations that apply at the point are derived by integrating Eq. (2.1) over the cell volume. This leads to difference equations of the form

$$\frac{d}{d\tau} \int_{\Delta V_{jk\ell}} \hat{q}\, d\xi\, d\eta\, d\zeta + \mu_j\, \delta_j\, \hat{f} + \mu_k\, \delta_k\, \hat{g} + \mu_\ell\, \delta_\ell\, \hat{h} = \ldots \tag{2.4a}$$

$$\Delta V = \Delta\xi\, \Delta\eta\, \Delta\zeta \tag{2.4b}$$

where the viscous terms have been suppressed for brevity, and where $\mu_j \delta_j$ is the centered spatial differential operator for the ξ_j direction

$$\mu_j \delta_j \hat{f} = (\hat{f}_{j+1,k,\ell} - \hat{f}_{j-1,k,\ell})/2 \tag{2.5}$$

and the central difference operators for the k and ℓ directions are defined similarly.

Within the second order spatial accuracy of the remaining terms, the volume integral that appears in the first term of Eq. (2.4) may be represented in terms of the cell-averaged value

$$\hat{q}_{jk\ell} = (\Delta V)^{-1} \int_{\Delta V} \hat{q} \, d\xi \, d\eta \, d\zeta \tag{2.6}$$

which is centered at the grid point $jk\ell$ itself since the grid point is located at the centroid of the cell that surrounds the point.

The final implicit space-time difference equations that govern the change $\Delta\hat{q} = \hat{q}^{n+1} - \hat{q}^n$ over a time step $\Delta\tau = \tau^{n+1} - \tau^n$ are obtained by evaluating the spatially differentiated terms at the advanced time τ^{n+1}, performing a first-order Taylor series expansion about the solution at time τ^n, and factoring the implicit operator. This yields the implicit ADI sequence

$$(I + \Delta\tau \, \mu_j \, \delta_j \, \hat{F})^n \, \Delta\hat{q}^{**} = -(\mu_j \, \delta_j \, \hat{f} + \mu_k \, \delta_k \, \hat{g} + \mu_\ell \, \delta_\ell \, \hat{h})^n \, \Delta\tau + \ldots \tag{2.7a}$$

$$(I + \Delta\tau \, \mu_k \, \delta_k \, \hat{G} + \ldots)^n \, \Delta\hat{q}^{*} = \Delta\hat{q}^{**} \tag{2.7b}$$

$$(I + \Delta\tau \, \mu_\ell \, \delta_\ell \, \hat{H} + \ldots)^n \, \Delta\hat{q} = \Delta\hat{q}^{*} \tag{2.7c}$$

where $\hat{F}$, $\hat{G}$, $\hat{H}$ are Jacobian matrices

$$\hat{F} = \frac{\partial\hat{f}}{\partial\hat{q}} \, , \quad \hat{G} = \frac{\partial\hat{g}}{\partial\hat{q}} \, , \quad \hat{H} = \frac{\partial\hat{h}}{\partial\hat{q}} \tag{2.7d}$$

and where the viscous terms again have been suppressed for brevity. Each step of the ADI sequence in Eq. (2.7) involves solving a block-tridiagonal linear system of equations to obtain the solution at interior grid points.

For grid points located on the boundaries of the computational space ξ,η,ζ, one or more of the five scalar components of Eq. (2.1) are replaced by algebraic boundary conditions. If the latter are nonlinear in time, they are linearized by a first-order Taylor series expansion about the solution $\vec{q}^n$. This yields a linear algebraic subsystem of the form

$$M^n \hat{q} = \vec{m}^n \tag{2.8}$$

The remaining scalar components of Eq. (2.1) (i.e., those scalar flow equations that have not been replaced by the aforementioned algebraic boundary conditions) are differenced by applying the finite-volume method in the same way as described above for interior points. However, to a typical boundary point such as $j = 1$, there corresponds not a full cell, but rather a half-cell whose width in the coordinate direction normal to the boundary is only half the width $\Delta\xi$ of an interior cell. The counterpart of Equations (2.4) take the form

$$\frac{d}{d\tau}\int_{\Delta V} \hat{q}\, d\xi\, d\eta\, d\zeta + \Delta_j \hat{f} + \mu_k \delta_k \hat{g} + \mu_\ell \Delta_\ell \hat{h} = \ldots, \quad j = 1 \tag{2.9a}$$

$$\Delta V = (\Delta\xi/2)\, \Delta\eta\, \Delta\zeta \tag{2.9b}$$

where Δ_j is the forward difference operator such that $\Delta_j = f_{j+1} - f_j$. The volume integral in the first term of Eq. (2.9a) still may be represented in terms of the value $\hat{q}_*$ at the cell centroid

$$\hat{q}_* = (\Delta V)^{-1} \int_{\Delta V} \hat{q}\, d\xi\, d\eta\, d\zeta \tag{2.10}$$

but the centroid is not located at the boundary grid point $j = 1$. However, within the spatial order of accuracy of Eq. (2.9), the value $\hat{q}_*$ may be

evaluated by linear interpolation between the boundary point $j = 1$ and the adjacent interior point $j = 2$.

$$\hat{q}_* = (I + \tfrac{1}{4}\Delta_j)\,\hat{q}' \qquad j = 1 \tag{2.11}$$

where I is the identity operator.

Equation (2.9a) is time-differenced implicitly and linearized in the same way as is Eq. (2.4) for interior points. The appropriate scalar components of the resulting equation are replaced by the linearized algebraic boundary conditions (2.8) and the implicit operator is factored to obtain the counterpart of the sequence (2.7) that applies at boundary points.

2.2 MODIFIED FORMULATION OF THE IMPLICIT ALGORITHM

The original formulation of the algorithm as presented in Reference 1 and summarized in the preceding subsection has two deficiencies: (1) the algorithm is valid only if the curvilinear coordinate transformation has no singular points where the Jacobian J vanishes, and (2) unacceptably large truncation errors can arise at grid points situated along the lines of intersection between boundary surfaces of the computational domain.

As an example where a singular transformation arises, consider the internal flow in an axisymmetric nozzle whose axis of symmetry coincides with the Cartesian x axis, and whose interior wall is of radius $r = r_w(x)$, $0 \le x \le L$. The first quadrant of the flow region interior to the nozzle can be mapped onto a rectangular parallelepiped in a right-handed curvilinear coordinate system ξ, η, ζ by the transformation

$$\begin{aligned} \xi &= \xi(x)\,, & 0 &\le x \le L \\ \eta &= -\theta\,, & 0 &\le \theta \le \pi/2 \\ \zeta &= \zeta(r)\,, & 0 &\le r \le r_w(x) \end{aligned} \tag{2.12}$$

where $\theta = \tan^{-1} y/z$

$$r = \sqrt{y^2 + z^2}$$

One can verify easily that the Jacobian J of this transformation vanishes at the axis of symmetry $y = z = 0$. The axis of symmetry maps onto the face $\zeta = 0$ of the parallelepiped in the transformed space ξ, η, ζ; hence, the transformation is singular at each point of that face.

The numerical mapping technique presented in Section 3 of Reference 1 also can generate curvilinear coordinate systems that have isolated singularities. For example, the quasi-elliptical mapping depicted in Figs. 3-3 and 3-4 of Reference 1 has a singularity at the point A that corresponds to the focus of the ellipse. The quasi-rectangular mapping given in Fig. 3-6 of Ref. 1 for the flow regions interior and exterior to a nozzle whose cross-section is super-elliptical also has singularities at the points of maximum curvature of the internal and external super-ellipses.

The numerical algorithm can be modified to handle isolated singularities such as those in the foregoing examples. Two modifications are necessary: first, as dictated by the finite-volume method, the Jacobian J at any grid point that coincides with a coordinate singularity must be computed as a cell-averaged quantity; and, second, the ADI sequence (2.7) must be modified to yield $\Delta\vec{q}$ directly, rather than $\Delta\hat{q}$, which involves the Jacobian as a factor. We shall deal with these modifications in order.

In general, the flow variable vector $\vec{q}$ is regular and non-zero even in the neighborhood of a coordinate singularity, whereas the compound quantity $\hat{q}$ in in Eq. (2.2) vanishes along with J at the singularity itself. Thus, Eq. (2.6) is a valid representation of the volume integral that appears in the first term of Eq. (2.4a) only at grid points where the ξ, η, ζ coordinate transformation is non-singular. At a singular point, the quantity $\hat{q}$ vanishes locally, whereas the volume integral is non-zero because it includes contributions from all regular points within the finite-volume cell that encloses the singular

point. Since $\vec{q}$ itself is regular, the volume integral in Eq. (2.4a) can be evaluated by applying the mean value theorem

$$(\Delta V)^{-1} \int_{\Delta V_{jk\ell}} \hat{q} \, d\xi \, d\eta \, d\zeta = \vec{q}_{jk\ell} \, J_* \tag{2.13}$$

where the cell-averaged Jacobian J_* is given by

$$J_* = (\Delta V)^{-1} \int_{\Delta V} J \, d\xi \, d\eta \, d\zeta \tag{2.14}$$

The latter is always non-zero for any cell of finite volume ΔV. If the singularity coincides with an interior grid point, then the integral in Eq. (2.14) can be evaluated analytically to second-order accuracy by introducing a local Taylor series expansion for the function $J(\xi, \eta, \zeta)$. If the singularity coincides with a boundary grid point, say $j = 1$, then the counterpart of Eq. (2.13) is

$$(\Delta V)^{-1} \int_{\Delta V} \hat{q} \, d\xi \, d\eta \, d\zeta = \vec{q}_* \, J_* \tag{2.15}$$

where both $\vec{q}_*$ and J_* represent cell-averaged values at the cell centroid, and can be computed individually by linear interpolation between the boundary point and the adjacent interior point (cf. Eq. (2.11)).

The alterations necessary to permit the direct computation of $\Delta\vec{q}$ from the algorithm are merely a special case of the alterations that permit the use of grids that move as a function of time (Ref. 2). One need only expand the term $\Delta\hat{q}$ as follows

$$\Delta\hat{q} = \vec{q}^{\,n} \, \Delta J + J^{n+1} \, \Delta\vec{q}$$

and redefine the Jacobian matrices in Eq. (2.7d) as

$$\hat{F} = \frac{\partial \hat{f}}{\partial \vec{q}}, \quad \hat{G} = \frac{\partial \hat{g}}{\partial \vec{q}}, \quad \hat{H} = \frac{\partial \hat{h}}{\partial \vec{q}}$$

Upon factoring the implicit operator in the implicitly time-differenced and linearized version of Eq. (2.4a), one obtains the ADI sequence

$$(J^{n+1} I + \Delta\tau \mu_j \delta_j \hat{F}^n)\Delta\vec{q}^{**} = -\vec{q}^n \Delta J - (\mu_j \delta_j \hat{f} + \mu_k \delta_k \hat{g} + \mu_\ell \delta_\ell \hat{h}) \Delta\tau + \ldots \tag{2.16a}$$

$$(J^{n+1} I + \Delta\tau \mu_k \delta_k \hat{G}^N + \ldots) \Delta\vec{q}^{\,*} = J^{n+1} \Delta\vec{q}^{\,**} \tag{2.16b}$$

$$(J^{n+1} I + \Delta\tau \mu_\ell \delta_\ell \hat{H}^n + \ldots) \Delta\vec{q} = J^{n+1} \Delta\vec{q}^{\,*} \tag{2.16c}$$

where $\Delta J = 0$ and $J^{n+1} = J^n$ if the grid is stationary in time, i.e., if the transformation $(x,y,z) \rightarrow (\xi, \eta, \zeta)$ is independent of time.

It is important to note that the form given in Eq. (2.8) must be retained when applying algebraic boundary conditions at boundary grid points, or the values of $\Delta\vec{q}^{**}$ and of $\Delta\vec{q}^{*}$ at boundary points will become inconsistent with those at interior points where Eqs. (2.16) are employed. That is, for a stationary grid, the boundary conditions must be written as

$$J M^n \Delta\vec{q} = \vec{m}^n \tag{2.17}$$

The modified algorithm given in Eqs. (2.16) and (2.17) should be valid at grid points that coincide with coordinate singularities as well as at regular points. However, numerical experiments for axisymmetric flow yield poor numerical results for the flow variables at grid points situated along the singular axis of symmetry, although the solution is accurate at all other points. We conjecture that the poor results at the symmetry axis result from a locally large truncation error, inasmuch as care was taken to incorporate the symmetry properties of the flow variables and of the Cartesian coordinates into the computation of the metrics and of the explicit fourth order smoothing terms in the

neighborhood of the axis.* To obtain an accurate solution at points on the axis, we have found it necessary to employ a time-lagging approach in which the flow variables at axis points are extrapolated from those at adjacent points following each time step. Even functions such as the temperature, density, and axial velocity component are extrapolated from those at the two adjacent interior points using a second degree polynomial whose gradient is zero at the axis, and odd functions such as the transverse velocity components are set to zero at the axis.

Locally large truncation errors also are incurred at other types of coordinate singularity, as well as exceptional but non-singular points of the curvilinear coordinate system. Examples of the latter are grid points that lie along the curves of intersection between two families of coordinate surface η = const. and ζ = const. that represent nozzle wall boundaries, such as the interior or exterior corner of a so-called "two-dimensional" nozzle that has flat walls and a rectangular cross-section. Such a corner point has the characteristic feature that the finite-volume cell associated with the point is either a quarter-cell (interior corner) or a three-quarter-cell (exterior corner). To avoid large numerical inaccuracies at such exceptional points, we have employed a time-lagging approach similar to that outlined above for singular points of an axisymmetric flow. For example, at axial corners where two walls intersect, we merely interpolate the temperature and density from the nearest neighboring wall points at the end of each time step.

---

* When the Cartesian x-axis coincides with the flowfield axis of symmetry, the coordinates y, z and their associated velocity components, v, w are odd functions of position relative to the axis, whereas x and all other flow variables are even functions.

2.3 MODIFIED SCHEME FOR SUBSONIC INFLOW AND OUTFLOW BOUNDARY CONDITIONS

2.3.1 Inflow Boundary Points

The scheme outlined in Section 4.2.2 of Reference 1 has been modified slightly to avoid an obvious inconsistency at inflow boundary grid points that lie on the nozzle walls. In the original inflow boundary scheme, four algebraic boundary conditions are applied that specify the total pressure, the total temperature, and the two direction cosines of the velocity vector. The fifth relation that is required to close the system of equations governing the five unknown components of the flow variable vector $\vec{q}$ is obtained from an implicit finite-volume discretization of the mass conservation equation (the first scalar component of Eq. (2.1)). This use of the mass conservation equation to determine the density is invalid at wall points because it is inconsistent with the density that is implied by the total pressure and total temperature through the equation of state. This follows from the fact that total and static temperatures are equal and total and static pressure are equal at wall points where the velocity vanishes. Thus, the algebraic boundary conditions alone are sufficient to determine the flow variables at wall points of the inflow boundary. Note, however, that when the temperature T_w specified as a boundary condition at nozzle walls, the inflow stagnation temperature boundary condition must be equal to T_w at points where the walls intersect the inflow boundary.

2.3.2 Outflow Boundary Points

For cases where one is interested in computing only the flow internal to the nozzle, the outflow boundary is positioned at the nozzle exit plane. When the ambient pressure outside the nozzle is sufficiently high relative to the internal flow stagnation chamber pressure, the flow will be wholly subsonic at the exit plane, and the ambient pressure must be imposed as a boundary condition on the static pressure at the outflow boundary [Ref. 1, Section 2.4.6]. In the original implicit algorithm for outflow boundary grid points, this boundary condition is linearized and used in place of the u-momentum equation. However, this results

in an inconsistent set of equations for the flow variables at grid points located at the nozzle wall, where additional algebraic boundary conditions on the velocity components and on either the wall temperature or heat flux also are imposed. The inconsistency becomes apparent when one observes that, for an adiabatic wall, the continuity and energy equations determine the gas density and temperature at the wall. The corresponding wall pressure implied by the equation of state in general will be inconsistent with the boundary condition on the exit plane pressure. A similar inconsistency exists at wall points when the wall temperature is specified as a boundary condition. The inconsistency can be avoided by retaining the u-momentum equation at all outflow boundary points, and using the imposed exit pressure boundary condition in place of the energy conservation equation. In addition, when the wall temperature T_w is specified as a boundary condition, the algebraic equation $T = T_w$ is used in place of the continuity equation at wall points of the outflow boundary. The physical justification for this procedure is that the gas density at the wall is determined completely by the exit pressure and wall temperature boundary conditions alone.

2.4 IMPLICIT DISSIPATION

The implicit algorithm permits the use of large time steps $\Delta\tau$ without numerical instability, and makes it possible to attain the steady-state solution of Eq. (2.1) in fewer time steps than would an explicit algorithm. However, hundreds of time steps usually are required to achieve convergence to steady state. In an effort to speed convergence, we have introduced artificial dissipative terms into the implicit one-dimensional operators on the L.H.S. of Eqs. (2.16). These dissipative terms are similar to those employed by Steger [Ref. 3], except that they are differenced in a conservative fashion and obey homogeneous boundary conditions. This ensures that the dissipative terms do not alter the global conservation properties of the difference equations [Ref. 1, Section 4.4].

The form of the dissipative term for the j coordinate direction is

$$\vec{d} = \begin{cases} \alpha\, E_j^{\frac{1}{2}}\, J\, \delta_j\, (\Delta\vec{q}) & , \quad j = 1 \\ \alpha\, \delta_j\, J\, \delta_j\, (\Delta\vec{q}) & , \quad 1 < j < j_{max} \\ -\alpha\, E_j^{-\frac{1}{2}}\, J\, \delta_j\, (\Delta\vec{q}) & , \quad j = j_{max} \end{cases} \tag{2.18}$$

where α is a constant; E is the classical shift operator which is defined such that for any mesh function f_j, $E_j^{\pm m} f = f_{j\pm m}$; δ is the classical central difference operator $\delta_j f = (E_j^{\frac{1}{2}} - E_j^{-\frac{1}{2}}) f$; and J is the transformation Jacobian in Eq. (2.3). The central member of Eq. (2.18) applies at interior points, and the first and last members apply at boundary points that are not situated at flowfield symmetry planes. For such symmetry boundary points, the dissipative terms are modified to account for the symmetry properties of $\vec{q}$ and of J. With the addition of the dissipative term (2.18), the implicit operator on the left side of Eq. (2.16a) for interior points assumes the form

$$(J^{n+1}\, I + \alpha\, \delta_j\, J^{n+1}\, \delta_j\, I + \Delta\tau\, \mu_j\, \delta_j\, \hat{F}^n)\, \Delta\vec{q} = \ldots$$

Similar dissipative terms are added to the implicit operators in Eqs. (2.16b) and (2.16c) for the η and ζ coordinate directions. These dissipative terms do not affect the final steady state solution, because $\Delta\vec{q}$ vanishes at steady state. Furthermore, they do not alter the unconditional numerical stability of the algorithm.

The introduction of the implicit dissipative terms is equivalent to appending terms of the form

$$\alpha(\Delta\xi)^2 \left(J\, \vec{q}_{\tau\xi}\right)_\xi \tag{2.19}$$

to the right side of the Navier-Stokes Equations (2.1). That is, a Taylor series expansion of Eq. (2.16) with the dissipative terms yields a modified partial differential equation which, to lowest order in $\Delta\tau$, $\Delta\xi$, $\Delta\eta$, $\Delta\zeta$ is identical to Eq. (2.1) with three additional terms of the form (2.19), one for each coordinate direction. The steady state solution of the Navier-Stokes equations is unaffected by the additional terms because all time-derivative terms vanish at steady state.

Numerical experiments indicate that the artificial implicit dissipative terms have a favorable effect on the convergence rate when dissipation coefficient α is of the order of unity (see Section 5.4). However, initial experimentation with the dissipative terms displayed a tendency to produce oscillations in the spatial distribution of computed flow variables across a subsonic inflow boundary. To damp these oscillations, which have a wavelength of twice the mesh spacings, $\Delta\eta$, $\Delta\xi$, we have found it necessary to filter the computed flow variable distribution at the inflow plane following the second and third steps of the ADI sequence (2.16) This is accomplished by the one-dimensional low-pass filters

$$\begin{aligned} \overline{\Delta\vec{q}^{*}} &= \mu_k^2 \Delta\vec{q}^{*} \\ \overline{\Delta\vec{q}} &= \mu_\ell^2 \Delta\vec{q} \end{aligned} \tag{2.20}$$

where μ denotes the classical central averaging operator

$$\mu_k = \tfrac{1}{2}(E_k^{\frac{1}{2}} + E_k^{-\frac{1}{2}})$$

Eqs. (2.20) apply only at interior points of the inflow plane. No filter is applied at the boundaries of the inflow plane unless those boundaries coincide with flowfield symmetry planes. For example, the intermediate solution $\Delta\vec{q}^{*}$ is not filtered over k at boundary points such as $k = 1$, k_{max} unless those points are located at symmetry planes, in which case the appropriate filter is $\Delta\vec{q}^{*} = E_k^{\pm\frac{1}{2}}\mu_k\Delta\vec{q}^{*}$, where the plus sign applies at $k = 1$ and the minus sign applies at $k = k_{max}$.

The described filters are applied only to the first, second, and fifth components of the flow variable vectors $\Delta\vec{q}$ and $\Delta\vec{q}^{*}$. The transverse momentum components $\Delta\rho v$, $\Delta\rho w$ are recomputed from the filtered component $\Delta\rho u$ using the inflow boundary conditions on the direction cosines of the velocity vector (see Section 2.3.1 above).

2.5 IMPROVED NUMERICAL GRID GENERATION TECHNIQUE

A general technique for generating a boundary-conforming curvilinear coordinate system ξ,η,ζ and computational grid suitable for geometrically complex nozzle configurations has been given in Section 3 of Reference 1. In this technique, a three-dimensional grid is built up by constructing a sequence of two-dimensional grids in successive cross-sectional planes $\xi(x)$ = const. Within each such y-z cross-sectional plane, the transverse coordinate system η,ζ and computational grid is generated numerically as the solution to an elliptic boundary value problem governed by the following elliptic system of equations

$$\alpha(y_{\eta\eta}+\varphi y_\eta)-2\beta y_{\eta\zeta}+\gamma(y_{\eta\zeta}+\psi y_\zeta) = 0 \tag{2.21a}$$

$$\alpha(z_{\eta\eta}+\varphi z_\eta)-2\beta z_{\eta\zeta}+\gamma(z_{\zeta\zeta}+\psi z_\zeta) = 0 \tag{2.21b}$$

where

$$\alpha = y_\zeta^2+z_\zeta^2 \tag{2.22a}$$

$$\beta = y_\eta y_\zeta+z_\eta z_\zeta \tag{2.22b}$$

$$\gamma = y_\eta^2+z_\eta^2 \tag{2.22c}$$

Equations (2.21) are solved numerically on a uniform, rectangular grid η_k, ζ_ℓ

$$\eta_k = (k-1)\Delta\eta \qquad ,k = 1,2,\ldots$$

$$\zeta_\ell = (\ell-1)\Delta\zeta \qquad ,\ell = 1,2,\ldots$$

to obtain the Cartesian coordinates (y,z) of the grid point in physical space that corresponds to each point (η_k,ζ_ℓ) in the computational space. The boundary values for Eq's. (2.21) are the y,z coordinates of grid points on the boundaries of the flow region in the physical domain. These boundary grid points may be distributed unequally along the boundaries in any fashion. The parameters φ,ψ in Eq's. (2.21) are evaluated locally at the boundaries in terms of the given boundary values (y,z) by using limiting forms of the elliptic equations. These parameters then are interpolated into the interior of the domain from the boundaries, and the elliptic system is solved numerically by a standard successive line over-relaxation technique. This results in a grid point distribution throughout the physical domain that is controlled entirely by the priori selection of the grid point distribution along the boundaries of that domain.

The described procedure always yields a boundary-conforming transformation in which the boundaries of the flow region in the physical domain are coordinate curves η = const. or ζ = const. of the curvilinear coordinate system. In the original technique (Ref. 1, Section 3), the parameters φ and ψ were evaluated from the boundary values using limiting forms of Eq's. (2.21) that were obtained by assuming that partial derivatives with respect to the curvilinear coordinate transverse to the boundary vanish locally at the boundary. For example, for a boundary ζ= const., the ζ-differentiated terms were dropped from Eq's. (2.21) to obtain the limiting forms

$$y_{\eta\eta}+\varphi y_\eta = 0 \tag{2.23a}$$

$$z_{\eta\eta}+\varphi z_\eta = 0 \tag{2.23b}$$

These equations then were used to evaluate the parameter φ locally at each grid point on the boundary in terms of the boundary values of y,z by replacing the differential operators by central difference operators

$$y_\eta \sim \frac{\mu_k \delta_k y}{\Delta\eta} \tag{2.24a}$$

$$y_{\eta\eta} \sim \frac{\delta_k^2 y}{(\Delta\eta)^2} \tag{2.24b}$$

To avoid locally large numerical errors at points where $|y_\eta|$ is small, Eq. (2.23a) was used only at points where $|y_\eta| \geq |z_\eta|$, whereas Eq. (2.23b) was used at points where $|y_\eta| < |z_\eta|$ (Ref. 1, Section 3).

The described procedure for evaluating the parameters φ,ψ from the boundary values was found to yield excellent computational grids for a variety of nozzle configurations. However, that procedure rests on a weak assumption, namely, that the derivatives in the direction transverse to the boundary can be dropped from the equations. One can show that these transverse derivatives actually vanish identically only when the boundary is both straight and is parallel to one of the Cartesian coordinate axes y or z. When this is not the case, the transverse derivatives are non-zero at the boundary. We recently have discovered that it is

possible to derive a universally valid limiting form of the elliptic system at the boundaries simply by imposing a local constraint on the angle of intersection between the two families of coordinate curves ξ = const. and η = constant. In particular one may impose the constraint that the two families be orthogonal everywhere along the boundaries*. This remarkable result can be proved as follows.

Consider the case where we wish to evaluate the function φ in Eq's. (2.21a,b) at a boundary $\zeta=\zeta_b$= constant. Upon eliminating the function ψ between the two equations, one obtains a single equation that can be cast in the form

$$\alpha\left[z_\zeta(y_{\eta\eta}+\varphi y_\eta)-y_\zeta(z_{\eta\eta}+\varphi z_\eta)\right] = z_\zeta^2\left[2\beta\left(\frac{y_\zeta}{z_\zeta}\right)_\eta-\gamma\left(\frac{y_\zeta}{z_\zeta}\right)_\zeta\right] \tag{2.25}$$

Now, the ratio y_ζ/z_ζ is merely the slope dy/dz of the family of coordinate curves η = const. that are transverse to the boundary curve $\zeta = \zeta_b$. We are at liberty to impose the constraint that the transverse coordinate curves η = const. be locally straight (i.e., have zero curvature) in the neighborhood of the boundary. This constraint may be stated in the form

$$\left(\frac{y_\zeta}{z_\zeta}\right)_\zeta = 0 \quad \text{at } \zeta = \zeta_b \tag{2.26}$$

We now impose the further constraint that these transverse coordinate curves η = const. be locally orthogonal to the boundary $\zeta = \zeta_b$. The orthogonality condition may be found as follows. Let $\vec{r} = (y,z)$ denote the radius vector in the Cartesian y-z plane. Then the local tangent vector to a coordinate curve η = const. is

---

* Note that this does not necessarily imply that the curvilinear coordinates will be orthogonal in the interior.

$$\vec{r}_\zeta = (y_\zeta, z_\zeta) \tag{2.27a}$$

Similarly the local tangent vector to a coordinate curve ζ = const. is

$$\vec{r}_\eta = (y_\eta, z_\eta) \tag{2.27b}$$

The two families of coordinate curves then are orthogonal if and only if

$$\vec{r}_\eta \cdot \vec{r}_\zeta = 0 \tag{2.28}$$

The orthogonality condition (2.28) may be expressed in the form

$$y_\eta y_\zeta + z_\eta z_\zeta = 0 \qquad \text{at } \zeta = \zeta_b \tag{2.29}$$

When we evaluate Eq. (2.25) at the boundary $\zeta = \zeta_b$, the second term in brackets on the R.H.S. vanishes by virtue of Eq. (2.26); the first term in those brackets also vanishes since $\beta = 0$ by virtue of the orthogonality relation (2.29). The latter relation may be used to eliminate all ζ-differentiated terms from the L.H.S. of Eq. (2.25). This yields a limiting form of the elliptic system that is valid at the boundary $\zeta = \zeta_b$, and that can be solved directly for the parameter φ

$$\varphi = -(y_\eta y_{\eta\eta} + z_\eta z_{\eta\eta})/(y_\eta^2 + z_\eta^2) \quad \text{on } \zeta = \zeta_b \tag{2.30}$$

This represents a universally valid equation that can be used to compute the numerical value of φ at each grid point on the boundary in terms of the boundary values y,z once the differential operators are replaced by the difference oprators (2.24). The corresponding expression that determines the parameter ψ along boundaries η = const. can be obtained directly from Eq. (2.30) by the substitution $\varphi,\eta \rightarrow \psi,\zeta$. The values of the parameters throughout the interior of the η,ζ domain then are found by linear interpolation as in the original method. For example, $\varphi(\zeta,\eta)$ is computed from its values at the two boundaries ζ = const. by linear interpolation along lines η = const. in the rectangular computational domain η,ζ. This ensures that the final grid obtained from a numerical solution of the elliptic system (2.21) will reflect the boundary value distribution, and will have the desirable property that the two families of grid lines are locally orthogonal at the boundaries of the physical flow region.

It is instructive to explore the geometric interpretation of Eq. (2.30), which is used to evaluate the parameter φ along a boundary $\zeta = \zeta_b$ = const. in terms of the pre-assigned boundary values of y,z. That equation can be re-cast in the form

$$s_{\eta\eta}+\varphi s_\eta = 0 \qquad \text{on } \zeta = \zeta_b \tag{2.31a}$$

where s denotes the arc length along the boundary curve $\zeta = \zeta_b$

$$ds = \sqrt{dx^2+dy^2} \tag{2.31b}$$

Eq. (2.31a) clearly possesses exponential solutions if φ is constant. Thus, the use of Eq. (2.30) to evaluate the parameter φ at each point along the boundary $\zeta = \zeta_b$ is equivalent to constructing a local exponential curve-fit to the arc length between the pre-assigned boundary grid points. The interpolation of the parameters φ,ψ into the interior of the computational domain simply extends the range of the curve-fit. The elliptic equation system (2.21) then merely provides a reliable, automatic means for translating the parameters into a local exponential curve-fit at each interior point that reflects the boundary value distribution, and that has the properties of regularity and monotonicity required of non-singular coordinate transformations. The resulting grid has the further desirable property that the two families of grid lines are locally orthogonal at the boundaries of the physical flow region.

As a final observation, we point out that the general method has the flexibility to allow one to control at will the angle of intersection between the two families of grid lines at boundaries. This can be accomplished as follows. In place of the orthogonality condition (2.28), we use the generalized condition

$$\vec{r}_\eta \cdot \vec{r}_\zeta = \left|\vec{r}_\eta\right| \left|\vec{r}_\zeta\right| \cos\Theta \qquad \text{on } \zeta = \zeta_b \tag{2.32}$$

where Θ denotes the local angle of intersection between the boundary curve $\zeta = \zeta_b$ and the family of transverse coordinate curves η = const. A more convenient representation of this condition is

$$y_\eta y_\zeta + z_\eta z_\zeta = (y_\eta z_\zeta - y_\zeta z_\eta)\cot\Theta \qquad \text{on } \zeta = \zeta_b \tag{2.33}$$

which satisfies Eq. (2.32) identically. Upon inserting the zero-curvature constraint (2.26) into Eq. (2.25), all ζ-differentiated terms in the resulting equation can be eliminated with the aid of Eq. (2.33). This yields the following equation for the parameter φ.

$$\varphi = -2\frac{(\sin\Theta)_\eta}{\sin\Theta} - \frac{(y_\eta - z_\eta\cot\Theta)y_{\eta\eta} + (z_\eta + y_\eta\cot\Theta)z_{\eta\eta}}{y_\eta^2 + z_\eta^2} \tag{2.34}$$

This last equation can be used in the same fashion as Eq. (2.30) to compute numerically the parameter φ in terms of η-derivatives of the pre-assigned boundary values y,z and of any pre-assigned distribution of Θ as a function of position along the boundary curve $\zeta = \zeta_b$.

Section 3
EVALUATION OF NOZZLE THRUST AND DISCHARGE COEFFICIENT

3.1 THRUST

There are two methods that can be used to compute the nozzle performance characteristics from the converged steady-state flowfield solution. For example, the net thrust may be computed by integrating the sum of the axial components of pressure force and viscous shear stress over the surfaces of the nozzle wall. Alternatively, the thrust may be computed from a global momentum balance. We shall employ the latter method because it involves only the integration of the Cartesian components of the momentum flux vector over the peripheral faces of the computational space; whereas the former method requires that computed velocity field be differentiated numerically in order to determine the wall shear stress.

The fact that a global momentum balance can be used to evaluate force components such as thrust is a formal consequence of the global conservation properties of the system of partial differential equations that govern the flow, namely, the Navier-Stokes equations (2.1). These global conservation properties can be derived simply by taking the volume integral of Eq. (2.1) over the entire computational space ξ, η, ζ. As a concrete example, let us consider the internal flow in an isolated three-dimensional nozzle with the right-handed curvilinear coordinate system ξ, η, ζ defined so that the surfaces $\xi = \xi_o$ and $\xi = \xi_{max}$ represent the inflow and outflow boundaries, respectively; the surfaces $\eta = \eta_o$ and $\eta = \eta_{max}$ represent the left and right sidewalls, respectively; and the surfaces $\zeta = \zeta_o$ and $\zeta = \zeta_{max}$ represent the upper and lower walls, respectively. The volume integral of Eq. (2.1) over the computational space $\xi_o \leq \xi \leq \xi_{max}$, $\eta_o \leq \eta \leq \eta_{max}$, $\zeta_o \leq \zeta \leq \zeta_{max}$ then may be written as

$$\frac{d}{d\tau}\int \hat{q}\, d\xi\, d\eta\, d\zeta + \int \hat{f}_{\xi}\, d\xi\, d\eta\, d\zeta$$

$$+ \int (\hat{g} - Re^{-1}\, \hat{\theta})_{\eta}\, d\eta\, d\zeta\, d\xi \tag{3.1}$$

$$+ \int (\hat{h} - Re^{-1}\, \hat{\omega})_{\zeta}\, d\zeta\, d\xi\, d\eta = 0$$

The first term in Eq. (3.1) vanishes at steady state. The volume integral in each of the remaining terms reduces to the difference of two surface integrals because the argument of the volume integral is a perfect differential with respect to one of the three spatial coordinates. The final result may be written in the following form

$$\int [\hat{g}(\xi, \eta_{max}, \zeta) - Re^{-1}\, \hat{\theta}\, (\xi, \eta_{max}, \zeta)]\, d\zeta\, d\xi$$

$$- \int [\hat{g}(\xi, \eta_0, \zeta) - Re^{-1}\, \hat{\theta}(\xi, \eta_0, \zeta)]\, d\zeta\, d\xi$$

$$+ \int \hat{h}(\xi, \eta, \zeta_{max}) - Re^{-1}\, \hat{\omega}(\xi, \eta, \zeta_{max})]\, d\xi\, d\eta \tag{3.2}$$

$$- \int [\hat{h}(\xi, \eta, \zeta_0) - Re^{-1}\, \hat{\omega}\, (\xi, \eta, \zeta_0)]\, d\xi\, d\eta$$

$$= \int \hat{f}(\xi_0, \eta, \zeta)\, d\eta\, d\zeta - \int \hat{f}(\xi_{max}, \eta, \zeta)\, d\eta\, d\zeta$$

Equation (3.2) is a formal expression of the steady state global conservation principles for the entire computational space. If we examine the first scalar component of this vector equation, each of the terms on the left side of the equation represents the net flow of mass through one of the four nozzle walls. Similarly, in the fifth scalar component of (3.2), each term on the left represents the net energy flux through one of the nozzle walls. In the middle three

components of Eq. (3.2), each term on the left represents the x, y, or z component of the total force acting on a wall. This includes the viscous shear force, which is represented by the term that is inversely proportional to the Reynolds number Re in the argument of the surface integral.

The terms collected on the R.H.S. of Eq. (3.2) have a corresponding physical interpretation as the net flux of mass, momentum, and energy through the nozzle inlet and exit planes. Thus if we define a "generalized force vector" $\vec{F}$ whose five components represent, respectively, the net mass flux through the nozzle walls, the three Cartesian components of the net force acting on the nozzle walls, and the net energy flux through the nozzle walls; then $\vec{F}$ can be computed from the equation

$$\vec{F} = \int \hat{f}(\xi_0, \eta, \zeta)\, d\eta\, d\zeta - \int \hat{f}(\xi_{max}, \eta, \zeta)\, d\eta\, d\zeta \tag{3.3}$$

which is simply a restatement of Eq. (3.2).

In the general case where both the interior flow and the external flow about a bilaterally symmetric nozzle are computed numerically, the nozzle structure is embedded entirely within the computational space. The curvilinear coordinate system then is defined such that the surface $\xi = \xi_0$ represents the inflow boundary and $\xi = \xi_{max}$ represents the outflow boundary, which is situated downstream of the nozzle structure; $\eta = \eta_0$ and $\zeta = \zeta_0$ represent flowfield symmetry planes; and the surfaces $\eta = \eta_{max}$ and $\zeta = \zeta_{max}$ represent outer freestream boundaries. The steady-state volume integral of Eq. (2.1) over the computational space then yields the following equation for the generalized force vector $\vec{F}$ acting on the nozzle structure

$$\begin{aligned}\vec{F} = &\int \hat{f}(\xi_0, \eta, \zeta)\, d\eta\, d\zeta - \int \hat{f}(\xi_{max}, \eta, \zeta)\, d\eta\, d\zeta \\ &- \int \hat{g}(\xi, \eta_{max}, \zeta)\, d\zeta\, d\xi - \int \hat{h}(\xi, \eta, \zeta_{max})\, d\xi\, d\eta\end{aligned} \tag{3.4}$$

The viscous terms do not appear in the last two integrals on the right of this equation because those terms vanish in the inviscid freestream (Ref. 1, Section 2.4.4).

The surface integrals in Eqs. (3.3) and (3.4) can be evaluated numerically from the computed flow variables by sequential application of one-dimensional trapezoidal integration formulas for the two coordinate directions along the surface. The trapezoidal formula is appropriate because it is consistent with the second order spatial accuracy of the numerical algorithm that is used to compute the flowfield.

We shall usually define the Cartesian coordinate system so that the x axis is oriented in the general streamwise direction. The second component of the generalized force vector $\vec{F}$ then represents the net thrust. The first and fifth components of the generalized force vector represent the net mass and energy fluxes at the walls of the nozzle. The net wall mass flux should be identically zero if the walls are impermeable. Similarly, for adiabatic wall boundary conditions, the net energy flux through the walls should also vanish identically. The extent to which these components of $\vec{F}$ differ from zero when evaluated numerically then provides a measure of the global accuracy of the flowfield computation.

We observe that the described method of computing the generalized force vector from surface integrals over the boundaries of the computational space is valid only if the algorithm that is employed to compute the flowfield does not compromise the global conservation principles that are satisfied by the partial differential equations (2.1). That is, the difference equations derived from (2.1) using the algorithm must obey the same global conservation principles, or Eqs. (3.3) and (3.4) will be invalid. Great care has been taken in the numerical computation of boundary conditions and in the formulation of artificial smoothing and dissipative operators to ensure that the composite numerical algorithm does indeed possess the same global conservation properties enjoyed by the original partial differential equations.

3.2 DISCHARGE COEFFICIENT

The nozzle discharge coefficient C_W is defined as the ratio of the total mass flow rate through the nozzle to the flow rate that would exist if the flow in the nozzle were isentropic [Ref. 4, p. 99]. According to one-dimensional isentropic nozzle flow theory, the dimensionless isentropic flow rate per unit area at the throat of a nozzle under flow conditions is [Ref. 4, p. 85]

$$\rho u = \left(\frac{2}{\gamma+1}\right)^{\frac{1}{2}\left(\frac{\gamma+1}{\gamma-1}\right)}$$

where γ is the specific heat ratio of the gas and the dimensionless density and velocity are referred to the stagnation chamber density and sound speed, respectively. The discharge coefficient is then given by the equation

$$C_W = \frac{W_T}{A_T}\left(\frac{\gamma+1}{2}\right)^{\frac{1}{2}\left(\frac{\gamma+1}{\gamma-1}\right)} \tag{3.5}$$

where W_T denotes the actual mass flow rate at the nozzle throat and A_T is the cross-sectional area of the nozzle at the throat. The latter two quantities may be computed from the final steady-state flowfield solution as follows.

We assume that the curvilinear coordinate transformation has the form $\xi = \xi(x)$, so that the surfaces ξ = const. represent cross-sectional planes. Let $\xi = \xi_T$ denote the throat location in the curvilinear coordinate system; the surfaces $\eta = \eta_0$ and $\zeta = \zeta_0$ represent flowfield symmetry planes; and the surfaces $\eta = \eta_W$ and $\zeta = \zeta_W$ represent complementary portions of the interior surface of the nozzle wall. The first component f_1 of the flux vector $\hat{f}$ can be interpreted physically as the mass flux in the ξ coordinate direction. The total mass flow rate at the throat then is simply

$$W_T = \int_0^{\zeta_W}\int_0^{\eta_W} f_1(\xi_T, \eta, \zeta)\, d\eta\, d\zeta \tag{3.6}$$

An analogous expression for the throat cross-sectional area can be obtained by noting that the normal vector to any surface ξ = const. has the Cartesian representation

$$\vec{n} = \nabla\xi \tag{3.7}$$

whence the element of area in such a surface is [Ref. 5]

$$dA = J|\nabla\xi| = \sqrt{\hat{\xi}_x^2 + \hat{\xi}_y^2 + \hat{\xi}_z^2} \tag{3.8}$$

Thus, the throat cross-sectional area is simply

$$A_T = \int_0^{\zeta_W} \int_0^{\eta_W} \sqrt{\hat{\xi}_x^2 + \hat{\xi}_y^2 + \hat{\xi}_z^2} \; d\eta \; d\zeta \tag{3.9}$$

where the metrics $\hat{\xi}_x$, $\hat{\xi}_y$, $\hat{\xi}_z$ are evaluated at the throat location $\xi = \xi_T$.

The surface integrals that appear in Eqs. (3.6) and (3.9) can be evaluated numerically in the same fashion as outlined in the preceding subsection for the surface integrals in the equations for the generalized force vector $\vec{F}$.

Section 4
FINAL FORMULATION OF TURBULENCE MODELS

The viscous terms on the R.H.S. of Eq. (2.1) involve the Prandtl number and a non-dimensional viscosity coefficient μ, which is referred to the dimensional viscosity at some reference state at which the Reynolds number Re is defined. For laminar flow, these are molecular transport properties, which we shall denote by the subscript e. For air at moderate temperatures, the Prandtl number is approximately constant

$$Pr_e = 0.72 \tag{4.1}$$

and the variation of viscosity with temperature may be approximated by a power law

$$\mu_e = T^m \tag{4.2a}$$

or may be computed from the Sutherland law

$$\mu_e = \frac{T^{3/2}}{T + 110.3/T_r(°K)} \tag{4.2b}$$

where the dimensionless temperature T is referred to the dimensional reference temperature T_r at which the Reynolds number Re is defined.

For turbulent flow, the viscosity is taken as the sum of the molecular value and a turbulent eddy viscosity

$$\mu = \mu_e + \mu_t \tag{4.3a}$$

where the dimensionless eddy viscosity is normalized by the reference value of μ_e that is used in evaluating the Reynolds number. The thermal conductivity,

which is proportional to the ratio between μ and Pr, is also taken as the sum of laminar and turbulent contributions

$$\frac{\mu}{Pr} = \frac{\mu_e}{Pr_e} + \frac{\mu_t}{Pr_t} \tag{4.3b}$$

where μ_t and Pr_t are obtained from some sort of turbulence model. Such models generally employ a constant value for the turbulent Prandtl number

$$Pr_t = 0.9 \tag{4.4}$$

whereas the eddy viscosity μ_e is strongly dependent on the character of the flow; e.g., boundary layer, shear layer, wake, or jet. The models that are used here for nozzle flows are presented below. The models are discussed first in the context of two-dimensional and axisymmetric flows, and are later generalized to more complicated three-dimensional flows.

4.1 TWO-DIMENSIONAL AND AXISYMMETRIC FLOW

In the present application, we require a turbulence model that is valid in the nozzle wall boundary layers; in the wake region behind a nozzle wall, side-plate, or wedge-plug; in the near-field mixing layer between the external flow and the nozzle exhaust stream, and in the far-field fully-developed jet region. Standard engineering turbulence models for the eddy viscosity are restricted to one or another of the described sub-regions of the flowfield, and must be patched together to provide a composite model. A general discussion of engineering models that apply in the various sub-regions has been given in Section 6 of Reference 1. These standard models were designed originally for use in analytical or simple numerical solutions for flows where the turbulent region is essentially a two-dimensional thin layer adjoining a region of spatially uniform, inviscid flow. In this type of solution, the boundaries of the turbulent region are relatively well-defined (such as the wall and the outer edge of a wall boundary layer) and determine the length scale in terms

of which the turbulence model is formulated. In complicated numerical solutions such as the nozzle flows of interest here, this need to locate the physical edge of a boundary layer, shear layer, or wake poses considerable difficulty; both because there generally are substantial flow gradients even in inviscid regions, and because spatial and temporal oscillations often exist in the computed flow variables at grid points. The difficulty, already severe in two-dimensional flows, can become extreme in three-dimensional flows where the geometry of a shear layer, for example, may be so complicated that it is not clear how one ought to proceed in order to find the boundaries of the layer and use that information to define a local length scale. Furthermore, computational accuracy can be highly uncertain because the engineering turbulence models generally are quite sensitive to the numerical value of the local length scale.

Baldwin and Lomax [Ref. 6] recently have presented a turbulence model for two- or three-dimensional wall boundary layers and wakes that does not require finding the boundaries of the turbulent region. This model is based directly on the engineering turbulence models described in Section 6 of Reference 1, but uses the spatial distribution of vorticity to determine the length scale in terms of which the eddy viscosity is computed. We shall employ a modified version of this model for the nozzle wall boundary layers and for the near-wake region downstream of the trailing edge of a nozzle wall, side-plate, or wedge-plug. For mixing layers and for the fully-developed jet region, we have developed a simple Prandtl mixing length type of model in which the turbulent length scale is defined in terms of the vorticity distribution, rather than in terms of the physical width of the mixing layer or jet. To facilitate the description of the models, we first define the character of the curvilinear coordinate system that is used for two-dimensional or axisymmetric flow.

We orient the x-axis of the Cartesian base coordinate system in the general streamwise direction. For two-dimensional flow in the x-z plane, the flow is invariant with respect to y. The right-handed boundary-conforming curvilinear coordinate system is defined such that $\xi = \xi(x)$, $\eta = \eta(y)$, $\zeta = \zeta(x,z)$. For

axisymmetric flow, the curvilinear coordinates are defined as in Eqs. (2.12), so that η is the azimuthal coordinate. The turbulence models to be used in the various sub-regions of the flowfield are presented below in terms of the described coordinate system. For convenience, the models will be presented in terms of a turbulent kinematic viscosity ν_t that is scaled by the reference Reynolds number. The dimensionless eddy viscosity coefficient that enters into Eq. (4.3) is obtained from ν_t by the following equation

$$\mu_t = \rho \, Re \, \nu_t \tag{4.5}$$

4.1.1 Wall Boundary Layers

The Baldwin-Lomax turbulence model [Ref. 6] is a two-layer model in which ν_t is given by

$$\nu_t = \begin{cases} (\nu_t)_{inner} & , \quad s \leq s_c \\ (\nu_t)_{outer} & , \quad s > s_c \end{cases} \tag{4.6}$$

where s denotes the normal distance from the wall and s_c is the least value of s at which the inner and outer viscosities are equal. The viscosity for the inner region is defined by

$$\nu_t = \ell^2 \, |\vec{\omega}| \tag{4.7a}$$

$$\ell = ks \, [1 - \exp(-s^+/A^+)] \tag{4.7b}$$

$$s^+ = \frac{s}{\mu_{ew}} \sqrt{Re \, \rho_w \, \tau_w} \tag{4.7c}$$

where $$\vec{\omega} = \nabla \times \vec{V} \tag{4.8}$$

is the vorticity, the subscript w denotes conditions at the wall, the wall shear stress is given by

$$\tau_w = \mu_{ew} |\vec{\omega}|_w \tag{4.9}$$

and the constants are

$$\begin{aligned} k &= 0.4 \\ A^+ &= 26 \end{aligned} \tag{4.10}$$

The corresponding formula for the outer region is

$$(\nu_t)_{outer} = C_1 \, F \, F_k(s) \tag{4.11a}$$

$$C_1 = 0.0269 \tag{4.11b}$$

$$F = \begin{cases} K^2 s_m f_m & , \quad K < 1 \\ s_m f_m & , \quad K \geq 1 \end{cases} \tag{4.11c}$$

$$K = U/2f_m \tag{4.11d}$$

where U is the maximum velocity in the profile

$$U = \max_s |\vec{V}(s)| \tag{4.12}$$

$F_k(s)$ is the Klebanoff intermittency factor

$$F_k(s) = [1 + C_2 \, (C_3 \, s/s_m)^6]^{-1} \tag{4.13a}$$

$$C_2 = 5.5 \qquad C_3 = 0.3 \tag{4.13b}$$

and where the quantities s_m and f_m are defined at the maximum point of the function

$$f(s) = s|\vec{\omega}| \, [1 - \exp(-s^+/A^+)] \tag{4.14}$$

In a numerical solution where both s and f are known only at discrete grid points, Baldwin and Lomax [Ref. 6] recommend that the true maximum be found by employing a three-point quadratic fit to the function $f(s)$ in the neighborhood of the apparent maximum that occurs on the grid.

This model has been used successfully in the computation of two- and three-dimensional flows with either attached or separated boundary layers [Ref. 6]. To apply the model to two-dimensional and axisymmetric flows in the curvilinear coordinate system ξ, η, ζ described earlier, we make several approximations that sharply reduce the computational labor. First, we assume that the ζ coordinate is approximately orthogonal to the wall, so that the normal distance s can be approximated as the arc length along ζ coordinate curves. If $\vec{r}$ denotes the radius vector in the Cartesian coordinate system, then the vector that is locally tangent to a ζ coordinate curve is

$$\vec{r}_\zeta = (x_\zeta, y_\zeta, z_\zeta) \tag{4.15}$$

The elemental arc length along the curve is then

$$s_\zeta = |\vec{r}_\zeta| = \sqrt{x_\zeta^2 + y_\zeta^2 + z_\zeta^2} \tag{4.16}$$

and the distance along the ζ coordinate curve can be obtained by integration of Eq. (4.16) from the wall outward.

The second approximation that we shall use relates to the computation of the vorticity vector in Eq. (4.8). The latter can be expanded in terms of the curvilinear coordinate system by means of the chain rule to obtain the equivalent expression

$$\vec{\omega} = \nabla \times \vec{V} = \nabla\xi \times \vec{V}_\xi + \nabla\eta \times \vec{V}_\eta + \nabla\zeta \times \vec{V}_\zeta \tag{4.17}$$

For a two-dimensional flow in the surface η = const., one can show easily that the dominant contribution to the magnitude of the vorticity vector in Eq. (4.17) comes from the component that is normal to the surface η = const. This statement also holds for axisymmetric flows in which η represents the azimuthal coordinate. The unit normal vector to a surface η = const. is

$$\vec{n} = \nabla\eta/|\nabla\eta| \tag{4.18}$$

and the vorticity component in this direction is the inner product

$$\vec{n} \cdot \vec{\omega} \tag{4.19}$$

By invoking the well-known vector identity governing successive inner and cross products, (4.17) and (4.19) can be combined to yield the result

$$\vec{n} \cdot \vec{\omega} = [(\nabla\eta \times \nabla\xi)\cdot\vec{V}_\xi + (\nabla\eta \times \nabla\zeta)\cdot\vec{V}_\zeta]/|\nabla\eta| \tag{4.20}$$

The first term in brackets in this last equation involves quantities that we already have neglected in deriving the parabolized Navier-Stokes equations (2.1) [Ref. 1, Section 2.3], and we shall neglect this term here as well. In fact, one can see from Eq. (4.20) itself that the first term involves velocity derivatives with respect to the streamwise coordinate ξ; i.e., in the direction along the wall. Such derivatives are always small in a boundary layer compared to derivatives $\vec{V}_\zeta$ in the direction away from the wall, and can safely be neglected. With this approximation, the dominant part of the vorticity magnitude can be written in the very simple form

$$|\vec{\omega}| = \frac{|\vec{r}_\xi \cdot \vec{V}_\zeta|}{J|\nabla\eta|} = \frac{|x_\xi u_\zeta + y_\xi v_\zeta + z_\xi w_\zeta|}{\sqrt{\hat{n}_x^2 + \hat{n}_y^2 + \hat{n}_z^2}} \tag{4.21}$$

where we have made use of the identity

$$\nabla\eta \times \nabla\zeta = J^{-1}\,\vec{r}_{\xi} \tag{4.22}$$

which is a property of the coordinate transformation $x,y,z \rightarrow \xi, \eta, \zeta$.

The numerical implementation of the above turbulence model is accomplished as follows. The spatial derivatives in Eqs. (4.16) and (4.21) are approximated by central difference operators at interior grid point and by the appropriate forward or backward difference operator at boundary grid points. The arc length s is computed from s_{ζ} by using the trapezoidal quadrature formula. Finally, the true maximum point of the function f in Eq. (4.14) is found as a function of the ζ coordinate; i.e., by operating in the computational coordinate system (ξ, η, ζ) in which the grid spacing is always uniform, rather than in physical space where the grid spacing is nonuniform with respect to the arc length s. The ζ coordinate will always be stretched with respect to the physical coordinate s in order to resolve the flowfield gradients that exist in the boundary layer, and a local quadratic fit to the function $f(\zeta)$ is performed more easily and more accurately than a corresponding fit to the function $f(s)$. Once the maximum point ζ_m is found, a similar quadratic fit to the function $s(\zeta)$ is used to determine the corresponding value $s_m = s(\zeta_m)$.

4.1.2 Wakes

Baldwin and Lomax [Ref. 6] state that the formulation in Eqs. (4.11) - (4.14) for the outer region of a boundary layer also can be used in wakes if the bracketed exponential factor is omitted from Eq. (4.14), and U is redefined as the difference between the maximum and minimum velocities in the wake region

$$U = |\vec{V}|_{max} - |\vec{V}|_{min} \tag{4.23}$$

Although it is not so stated in Reference 6, the transverse coordinate s presumably is reckoned from the point of minimum velocity. For an asymmetric wake, this would imply that the regions on either side of the velocity minimum

are to be treated separately. If this were done, it follows from Eqs. (4.11) and (4.14) that the turbulent viscosity would be discontinuous at the point of minimum velocity. Furthermore, Baldwin (in a private communication) has stated that computational instabilities were encountered in attempting to use the outer formulation alone in the near wake of an airfoil because the grid is most refined near the velocity minimum where the value of ν_t is greatest. The instability can be avoided (according to Baldwin) by arbitrarily using the same two-layer formulation as in the boundary layer, with the bracketed exponential factor omitted from Eq. (4.7b). Because the resulting inner formulation is inconsistent with other wake turbulence models, we shall employ a different model for the inner region of the wake, i.e., near the velocity minimum. This model employs the Prandtl mixing length formula (4.7a) but the mixing length ℓ is defined as

$$\ell = C\, U/|\vec{\omega}|_{max} \tag{4.24}$$

where U is given by Eq. (4.23), C is a constant and

$$|\vec{\omega}|_{max} = \max_{s \geq 0} |\vec{\omega}(s)|$$

is the maximum vorticity magnitude in the section of the wake under consideration, since the two sections on either side of the velocity minimum are treated separately. Note that ν_t in Eq. (4.7a) remains virtually continuous at the border between wake sections even though the latter are treated separately, because $|\vec{\omega}|$ as computed from Eq. (4.21) essentially vanishes at the velocity minimum.

For a wake, the constant C in Eq. (4.24) has the value

$$C_{wake} = 0.255 \tag{4.25}$$

This value was obtained as follows.

In any turbulence model such as that of Eqs. (4.7a) and (4.24), the constants must be evaluated from experimental data for the specific type of flow under

consideration. This is done for wake turbulence models by requiring that the wake spreading rate predicted by the model match that measured experimentally. An analytical wake solution based on a mixing length model is given in Schlichting [Ref. 7, p. 600]. In this solution, the mixing length is defined differently from Eq. (4.24), and is evaluated so as to match the measured wake spreading rate behind a circular cylinder transverse to the flow. We have used the wake velocity profile from the analytical solution to deduce the value of C in Eq. (4.25) that matches the experimental spreading rate when the mixing length is defined by Eq. (4.24).

Schlichting [Ref. 7, p. 603] also gives an analytical wake solution based on a different eddy viscosity model in which ν_t is given by

$$\nu_t = \kappa b U \tag{4.26}$$

where b is the wake width and κ is a constant that is determined to match the measured wake spreading rate. This model, unlike the mixing length model, assumes ν_t to be constant throughout the wake. Yet, the velocity profile from this analytical solution can be used to deduce a value for the constant C in the mixing length model that is in very close agreement with the value in Eq. (4.25). The value $C_{wake} = 0.259$ is obtained by simply requiring that the mixing length model yield the same value for ν_t at the maximum vorticity point in the wake as does the model (4.26) from which the analytical velocity profile is derived. This means that we can calibrate the Prandtl mixing length model for a given type of flow by using the analytical solution from the simpler model (4.26) once the latter has been calibrated to agree with experiments for that type of flow. We shall make use of this calibration technique below in modeling ν_t for mixing layers and jets.

4.1.3 Mixing Layers and Fully-Developed Jet Region

As discussed in Section 6 of Reference 1, we had intended to employ the constant eddy diffusivity model (4.26) in mixing layers and in the fully-developed region

of the exhaust jet. This type of model in which ν_t is a constant is difficult to link to other models for adjoining flow regions without having large discontinuities in the spatial distribution of ν_t. For this reason, we favor the Prandtl mixing length model given in Eq. (4.7a). There, ν_t is proportional to the local vorticity, which tends to be small both in inviscid regions and near the border between turbulent sub-regions that require different turbulence models. We shall apply a one-layer model of the type (4.7a) for a mixing layer or jet. As in the inner region of a wake, we determine the mixing length scale from the velocity extrema and the maximum vorticity (Eq. (4.24)), but the constant C must be calibrated separately for each type of flow.

Mixing Layers

Schlichting [Ref. 7, p. 598] gives an analytical solution for the two-dimensional mixing layer based on the constant eddy viscosity model (4.26), with the constant κ selected to match experimental data on the width of the turbulent region. We have calibrated the mixing length model by the technique described in Section 4.1.2; that is, by requiring that the mixing length model yield the same value for ν_t at the maximum vorticity point in the layer as does the constant eddy viscosity model. The resulting value of the constant C in Eq. (4.24) is

$$C_{mix} = 0.136 \tag{4.27}$$

Fully-Developed Jet

The region downstream of the point where the inner edge of the mixing layer between the external flow and the nozzle exhaust stream penetrates to the flow centerline is known as the fully-developed jet. Since we are interested primarily in three-dimensional flows, we assume that this region far downstream of the nozzle exit is essentially similar to that for a round (axisymmetric) jet. Accordingly, we calibrate the mixing length model from the analytical solution

for the round jet based on the constant eddy viscosity model [Ref. 7, p. 607], by again requiring that the mixing length model yield the same value for ν_t at the point of maximum vorticity. This gives the following value for the constant in Eq. (4.24)

$$C_{jet} = 0.129 \tag{4.28}$$

The latter is very close to the value in Eq. (4.27) for a mixing layer. Since the turbulence models are only approximate, in programming the models for numerical solution, we simply have used the same value

$$C = 0.13 \tag{4.29}$$

for both mixing layers and jets.

4.2 GENERAL THREE-DIMENSIONAL FLOWS

For axisymmetric three-dimensional flows, the turbulence model equations given in the preceding section are obtained by viewing the flow as essentially two-dimensional in an azimuthal coordinate surface η=const. We denote the turbulent viscosity so obtained as $\nu_t^{(\zeta)}$, since Eq. (4.21) for the vorticity magnitude involves $\vec{V}_\zeta$ in which derivatives of the velocity are taken with respect to the ζ coordinate direction within a surface η = const. For general three-dimensional flows governed by the parabolized Navier-Stokes equations (2.1) in which the viscous terms associated with the streamwise coordinate ξ are neglected, there are two principal cross-stream coordinate directions η, ζ. In this case, we use the same quasi-two-dimensional approach to obtain $\nu_t^{(\zeta)}$ based on regarding the flow as two-dimensional within a coordinate surface η = const., and apply a similar quasi-two-dimensional approach to compute a second value $\nu_t^{(\eta)}$ based on regarding the flow as two-dimensional in a surface ζ = const. The equations for $\nu_t^{(\eta)}$ are obtained from Eqs. (4.6) - (4.29)by the substitution $(\eta, \zeta)\rightarrow(\zeta, \eta)$. To obtain a single composite value for ν_t at each point of flowfield, we arbitrarily combine the quasi-two-dimensional values by using the root-mean-square

$$\nu_t = \left\{ [\nu_t^{(\eta)}]^2 + [\nu_t^{(\zeta)}]^2 \right\}^{\frac{1}{2}} \tag{4.30}$$

In mixing layers and jet regions, both $\nu_t^{(\eta)}$ and $\nu_t^{(\zeta)}$ are obtained from the same formulation. However, in wall boundary layers and near wake regions, a certain arbitrariness exists in the quasi-two-dimensional approach. Consider, for example, a wall boundary layer. The boundary-conforming character of the curvilinear coordinate transformation is such that a wall is represented as either a surface η = const., a surface ζ = const, or as a composite of intersecting surfaces of each type. Over any portion of a wall that is represented as a surface ζ = const., the nature of the transformation is such that coordinate lines along which ζ alone varies are nearly orthogonal to the wall in the boundary layer, and the boundary layer formulation given in Eqs, (4.16) - (4.21) applies for computing $\nu_t^{(\zeta)}$. Within each wall-like coordinate surface ζ = const., the boundary layer formulation (4.6) - (4.21) with the substitution $(\eta,\zeta) \rightarrow (\zeta, \eta)$ also is used to compute $\nu_t^{(\eta)}$ in boundary layer regions where this surface ζ = const. intersects a wall that is represented as a member of the other family of coordinate surfaces η = const. However, a different model is necessary when this is not the case. An example is an axisymmetric flow where η is the azimuthal coordinate and the wall is a surface ζ = const. [cf. Eq. (2.12)]. The boundary layer formulation then is appropriate for $\nu_t^{(\zeta)}$, but is inappropriate for $\nu_t^{(\eta)}$ since the ζ = const. surfaces are wall-like coordinate surfaces that do not intersect the wall. In such cases, we arbitrarily use the mixing layer formulation to compute $\nu_t^{(\eta)}$. This always yields a value of $\nu_t^{(\eta)}$ that is dominated by the value of $\nu_t^{(\zeta)}$ obtained from the boundary layer formulation, and ensures that the composite value in Eq. (4.30) will recover the correct result, namely, $\nu_t^{(\zeta)}$, within the boundary layer. The same approach is used in two-dimensional wake regions in that the quasi-two-dimensional value of ν_t for the coordinate surfaces transverse to the wake is obtained from the mixing layer formulation.

SECTION 5

NUMERICAL EXPERIMENTS

A number of numerical experiments have been performed for two-dimensional internal and external flows to test various aspects of the implicit numerical method. These experiments are described in the following subsections. Section 5.1 demonstrates that the numerical method is capable of computing internal flows with boundary layer separation. Section 5.2 gives the results of computations that have been performed to investigate the effects of implicit boundary conditions and of time stepsize on the rate of convergence to steady state and on the final steady state solution. Section 5.3 gives the results of parametric calculations to investigate the sensitivity of the solution to the magnitude of the explicit smoothing coefficient. Section 5 demonstrates that the artificial implicit dissipative terms described in Section 2.4 have a favorable effect on the numerical stability and on the rate of convergence to steady state. The major conclusion drawn from these experiments are summarized in Section 5.5.

5.1 COMPUTATION OF SEPARATED FLOW

To demonstrate that the numerical method is capable of computing internal flows with boundary layer separation, we have performed an internal flow computation for a two-dimensional converging-diverging nozzle whose wall is composed of two cosine-shaped segments. The nozzle shape and computational grid are shown in Fig. 5-1. The computation is for laminar flow at a Reynolds number based on stagnation conditions of 10^5, a Prandtl number of unity, and viscosity proportional to temperature. The grid is 15 x 15 in the x and z directions, stretched exponentially in the z direction to resolve the nozzle wall boundary layer. That is, the curvilinear coordinate transformation is defined by the equations

$$z/z_{max}(x) = \left[\exp(\sigma\zeta/\zeta_{max})-1\right]/\left[\exp(\sigma)-1\right]$$

$$\zeta = (\ell-1)\Delta\zeta \quad , \Delta\zeta = 1 \quad , \ell = 1,2,\ldots, l_{max}$$

where σ is a constant stretching coefficient, and $z_{max}(x)$ is the wall shape.

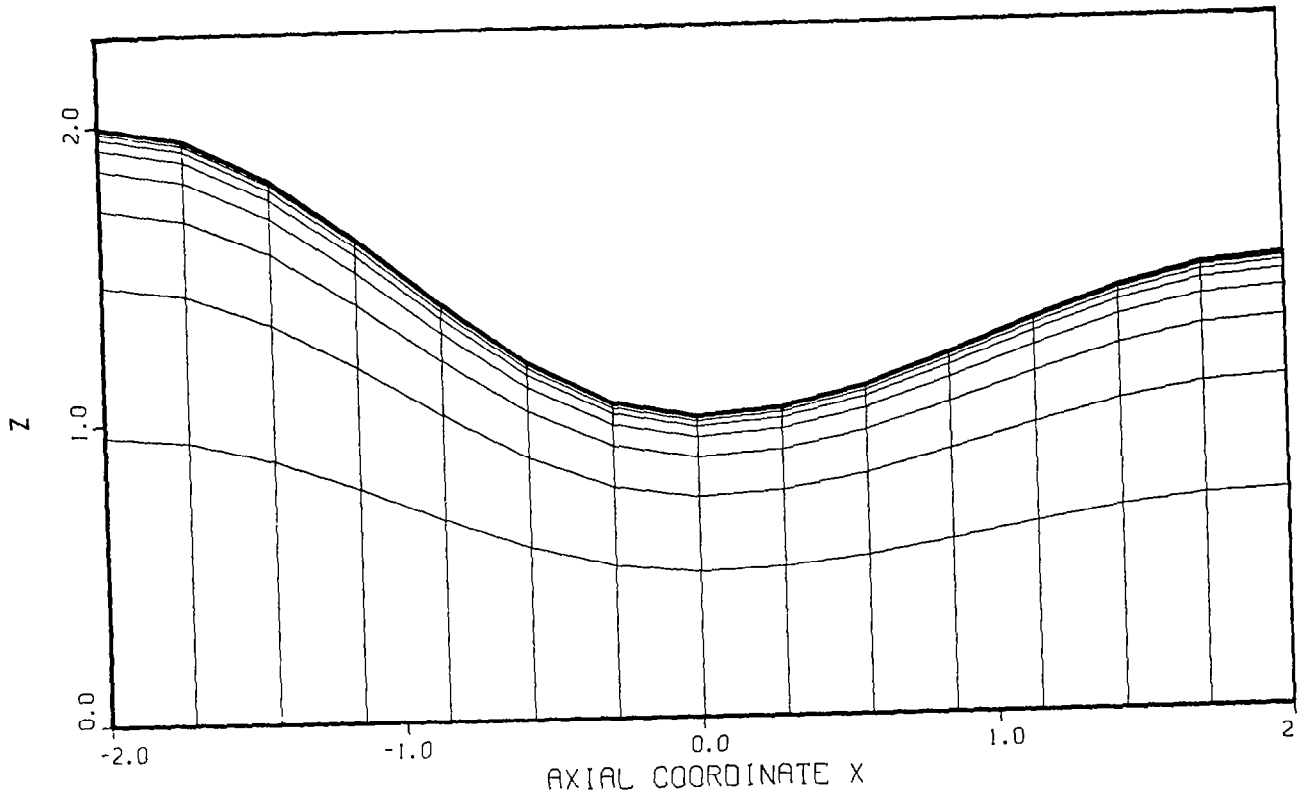

Figure 5-1 Computational Grid for Cosine Nozzle

Crude a priori estimates of the boundary layer thickness indicated the latter to be approximately one percent of the local nozzle height over most of the length of the nozzle wall. To resolve this thin region, the stretching parameter σ was selected to produce a grid spacing at the wall that is a factor of 5000 smaller than the grid spacing at the centerline.

The computation has been performed using the implicit inflow, outflow, symmetry, and adiabatic wall boundary condition computation schemes described in Sections 2.4 and 4.2 of Reference 1 and in Section 2.3 herein.

The initial conditions are as follows. The nozzle is assumed to be choked at the throat. The pressure, density, temperature, and streamwise velocity (averaged over the cross section) are computed from one-dimensional inviscid isentropic flow theory for the nozzle area variation. These inviscid core conditions are applied over the lower half of the grid $0<\zeta<\zeta_{max/2}$, assuming that the streamlines are parallel to the grid lines ζ = constant. The velocity components at the nozzle wall $\zeta = \zeta_{max}$ are set to zero to satisfy the no-slip viscous wall boundary conditions. The velocity components at the remaining grid points are linearly interpolated in ζ between $\zeta_{max/2}$ and ζ_{max}. The Crocco relation is used to compute temperature from velocity in this region. Density follows from the equation of state by taking the pressure as uniform over the nozzle cross section at each x station.

Convergence to steady state was obtained in 300 time steps using a constant step-size $\Delta\tau = 0.05$, which corresponds to a Courant number $Co(\zeta) = 530$. The computed longitudinal pressure distributions along the wall and centerline are shown in Fig. 5-2, together with the pressure distribution predicted by one dimensional isentropic flow theory (Ref. 4) for the nozzle area variation. Pressures shown are referred to stagnation pressure. As one might expect, the computation shows a substantial recompression at the wall near the exit plane that is induced by the locally concave wall shape. The inviscid core flow is supersonic in this region, and the adverse pressure gradient causes boundary layer separation between $x \approx 1.4$ and the exit plane. The longitudinal velocity profile in the separated region is smooth, as shown in Fig. 5-3, and displays the classic flow reversal in the near-wall region that one expects from boundary layer theory. In the figure, velocity is referred to the stagnation sound speed.

The vertical profiles of pressure and velocity at the geometric throat, $x = 0$, are given in Figs. 5-4 and 5-5, and show substantial nonuniformities due to the two dimensionality of the flow.

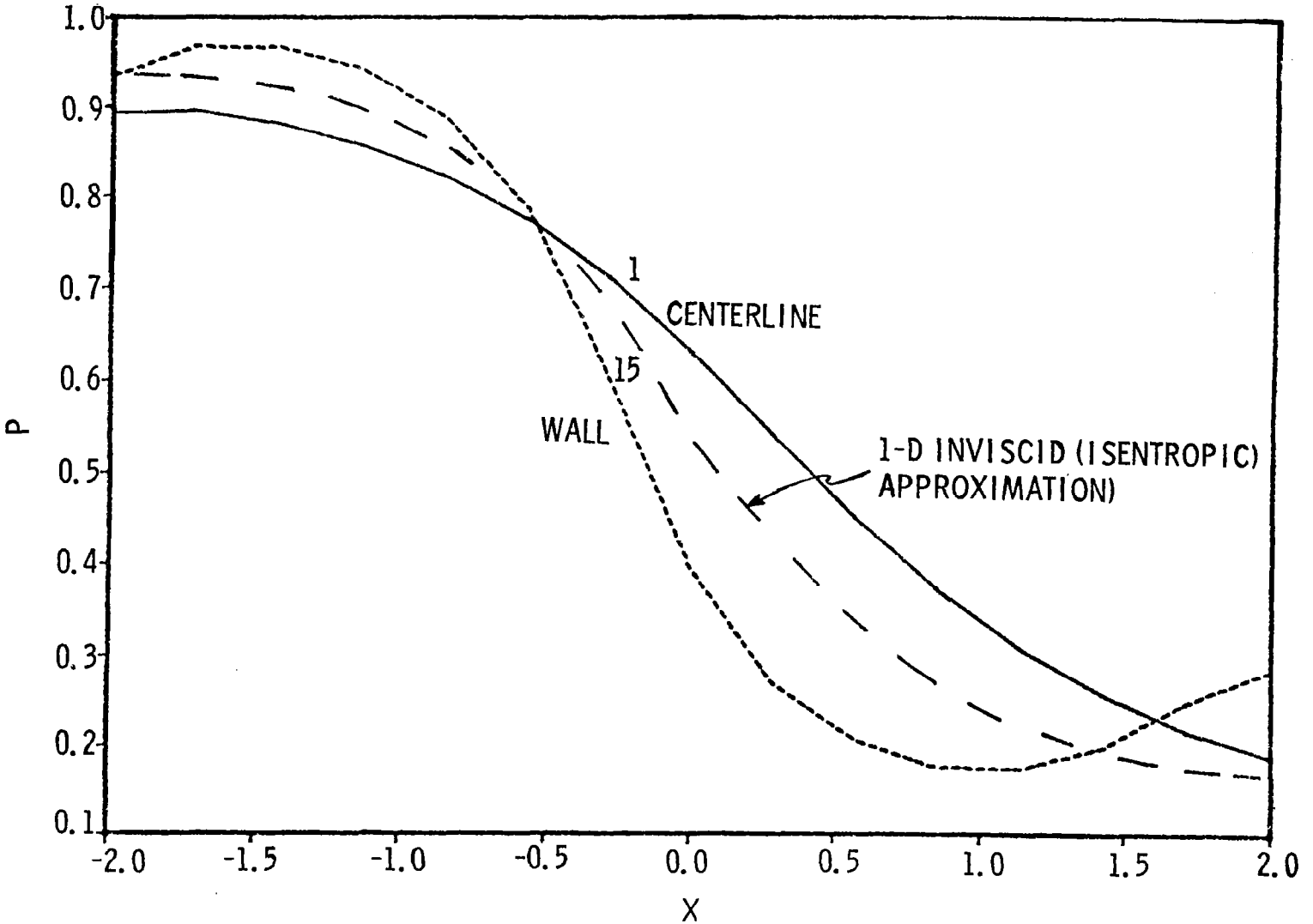

Figure 5-2 Longitudinal Distributions of Pressure, Cosine Nozzle, Re = 10^5.

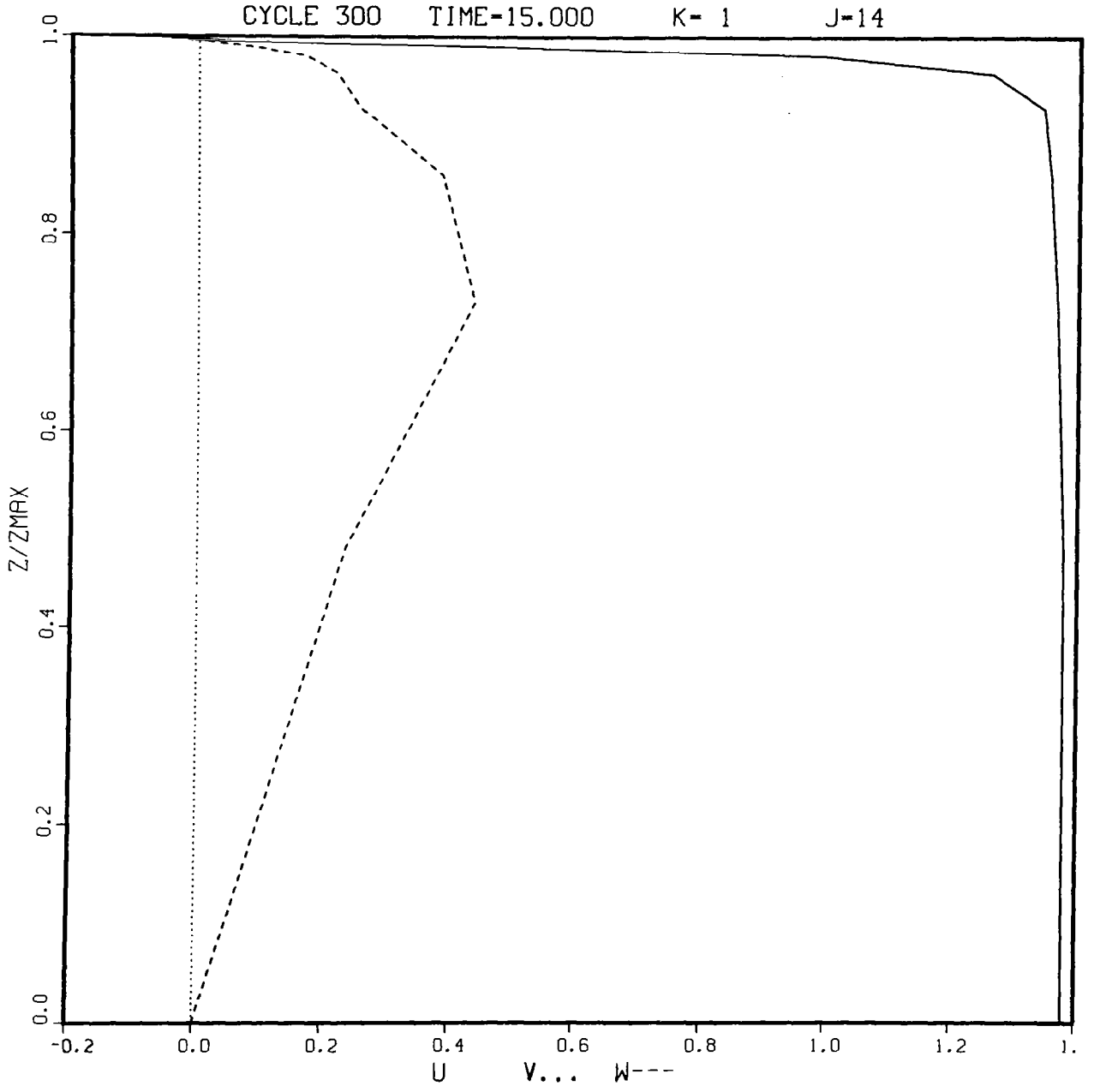

Figure 5-3a Velocity Profiles Across Cosine Nozzle in Separated Region, Re = 10^5.

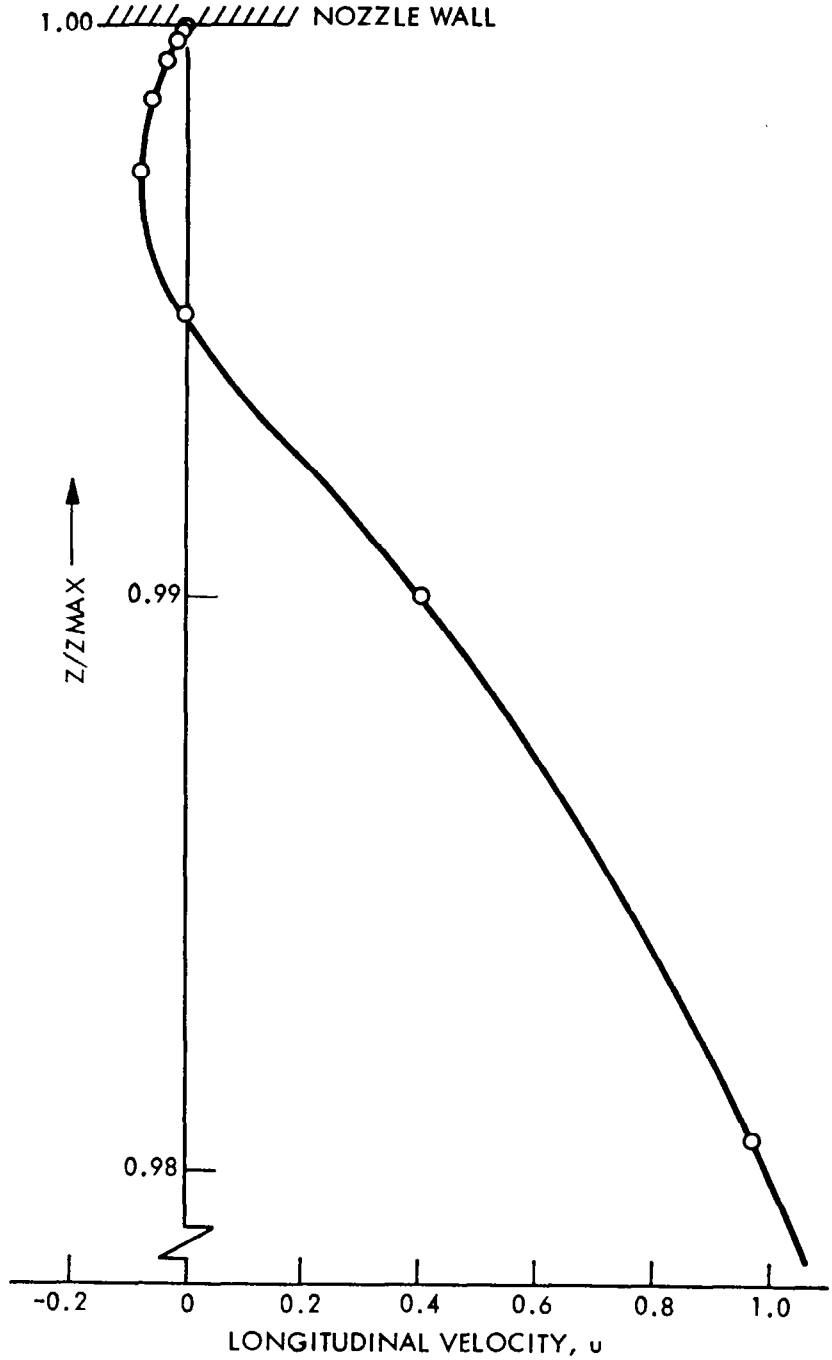

Figure 5-3b Magnified View of Longitudinal Velocity Profile in Separated Region, Cosine Nozzle, Re = 10^5.

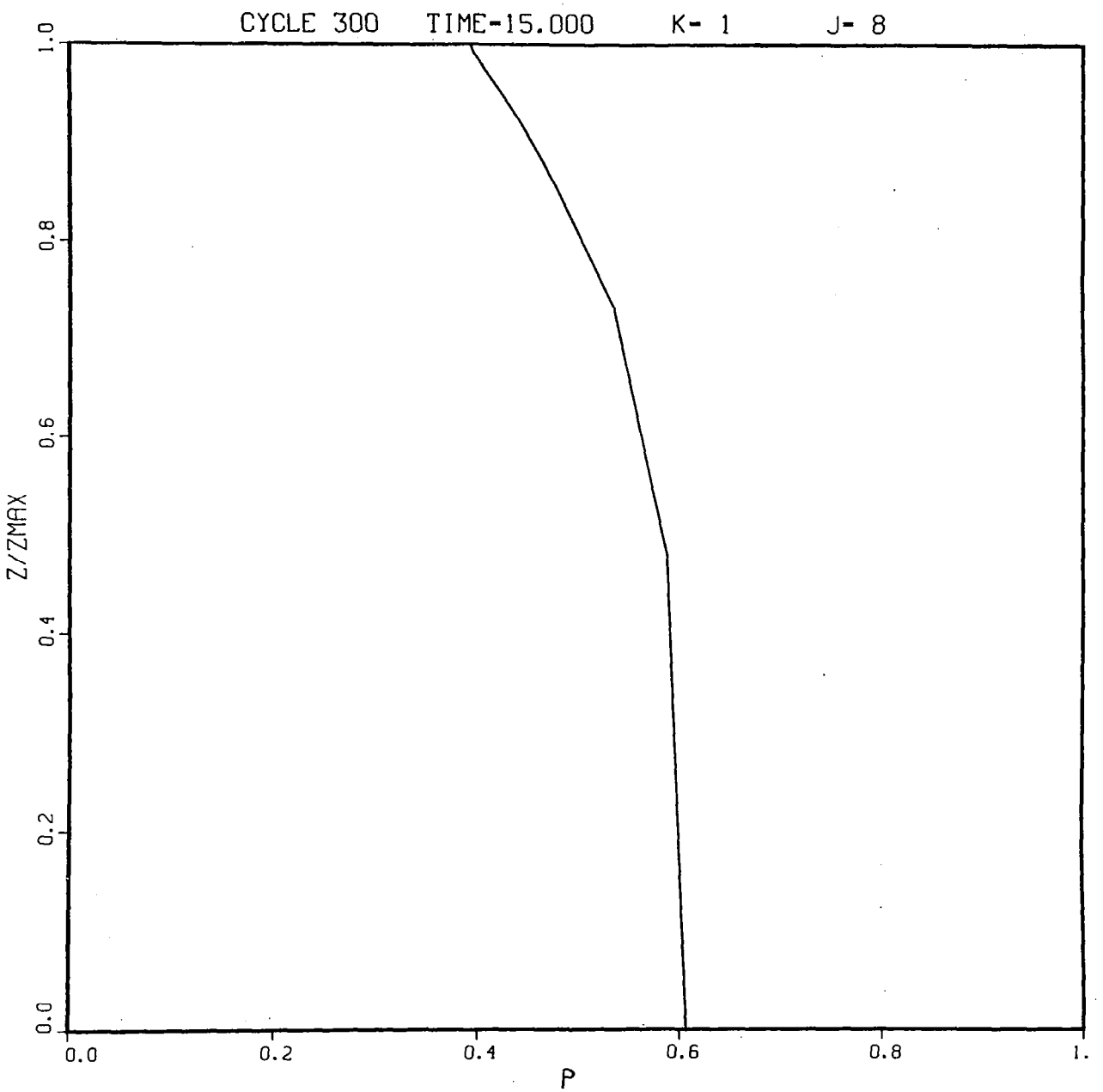

Figure 5-4 Pressure Profile Across Cosine Nozzle at Throat, x = 0.

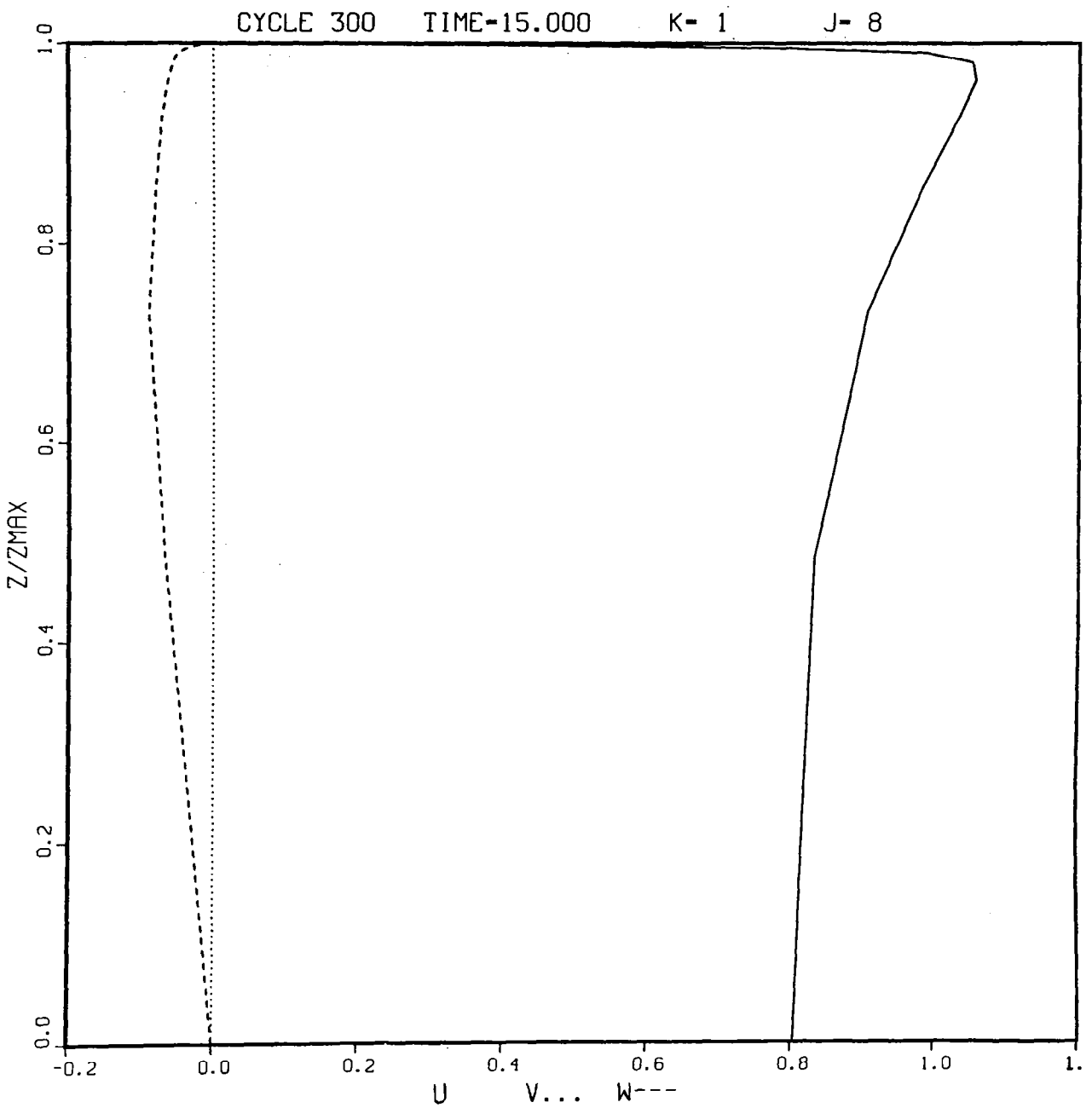

Figure 5-5 Velocity Profiles Across Cosine Nozzle at Throat, x = 0.

5.2 EFFECT OF IMPLICIT BOUNDARY CONDITIONS AND TIME STEPSIZE ON THE SOLUTION

5.2.1 Implicit Boundary Conditions

A set of numerical experiments has been performed to explore whether the use of implicit boundary conditions has any significant effect on the rate of convergence to steady state or on the final steady state solution. These tests were made for two-dimentional laminar flow over an adiabatic flat plate at a freestream Mach Number $M_\infty = 0.1$, Reynolds Number $Re_\infty = 10^5$, Prandtl Number $Pr = 1$, and viscosity proportional to temperature. The grid and initial conditions are as described in Ref. 1, Section 5. In one case, implicit wall, freestream, and outflow boundary conditions were employed as described in Ref. 1, Sections 2.4 and 4.2. In the other case, time-lagged explicit boundary conditions were applied as follows. During each time step, the flow variables $\vec{q}^{n+1} = \vec{q}^n + \Delta\vec{q}$ are computed implicitly at interior grid points by assuming that $\Delta\vec{q} = 0$ at boundary grid points. The flow variables at boundary points are then updated at the end of the step by extrapolation of the solution $\vec{q}^{n+1}$ from interior points. At wall boundary points, the velocity components $(u,v,w)^{n+1}$ are set to zero and the wall pressure is computed from the normal momentum equation. For a flat plate, the latter equation implies that the pressure gradient in the wall-normal direction vanishes, hence the pressure at each wall point is set equal to that at the adjacent interior point. To satisfy the adiabatic wall conditions the gas temperature at the wall is extrapolated quadratically with zero gradient using the temperature at the two nearest interior points along the wall-normal grid line. At the downstream outflow boundary, $\vec{q}^{n+1}$ is extrapolated linearly from the two nearest interior points along each grid line transverse to the outflow boundary. At the lateral outer boundary, the freestream values of pressure, temperature, and streamwise velocity component u are imposed, and the transverse momentum flux components ρv and ρw are extrapolated linearly from interior points.

Numerical solutions for the two cases, implicit vs. time-lagged boundary conditions, showed no significant difference in either convergence rate or in the final steady-state solution as obtained with a constant time stepsize $\Delta\tau = 0.01$. The latter corresponds to a Courant number $Co = 40$ based on the minimum mesh spacing in the direction normal to the plate. Both cases converged within 300 steps and yielded steady-state drag coefficients that differed by only 0.07%. However, attempts to increase the time stepsize revealed that the solution with implicit boundary conditions remains numerically stable with time stepsizes significantly greater

than those attainable with time-lagged boundary conditions.

With implicit boundary conditions, the computation remains stable and converges well for a time step as large as $\Delta\tau = 0.1$ (Co = 400). With time-lagged boundary conditions, the computation is unstable for $\Delta\tau = 0.05$ (Co = 100). We have not attempted to determine the precise stability boundaries for the two cases, because our experience has shown that the stability boundary depends upon the flow conditions. With $M_\infty = 3$, for example, the flat plate flow computation is unstable at $\Delta\tau = 0.05$ (Co = 300), even with implicit boundary conditions.

As shown in the next section, the solution usually converges to steady state more rapidly, i.e., in fewer steps, the larger the stepsize $\Delta\tau$. Because the use of implicit boundary conditions permits a larger stepsize, we conclude that implicit boundary conditions significantly improve overall computational efficiency by allowing convergence to be attained in fewer steps than would be required with time-lagged boundary conditions.

In addition to the described experiments comparing implicit and time-lagged boundary conditions, we have performed some test computations to evaluate the sensitivity of the solution to the placement of the lateral outer boundary at which freestream pressure, temperature, and streamwise velocity component, u, are imposed as boundary conditions, but the transverse momentum components are computed implicitly from the transverse momentum equations. The results of these tests have been reported in detail in Ref. 9, and we merely summarize them here.

For supersonic flow, $M_\infty>1$, the solution was found to be insensitive to the location of the outer boundary as long as the latter was positioned far enough above the plate to enable the shock wave generated by the viscous interaction to be captured in the mesh.

For subsonic flow, $M_\infty<1$, the solution again was insensitive to the placement of the outer boundary. The overall solution and the computed drag coefficient differed by less than 0.1% when the outer boundary was shifted inward from ten boundary layer thicknesses above the plate to as little as two boundary layer thicknesses above the plate. The convergence histories were also virtually identical for the two cases. Similar computations in which all freestream conditions were imposed at the lateral outer boundary displayed a markedly different behavior. As much as a factor of three more time steps were required to attain convergence to steady state, and the final solution was quite sensitive to the placement of the outer boundary. The

computed drag coefficient was found to vary with boundary position, and the velocity profiles within the boundary layer showed a serious distortion that did not arise when the transverse momentum components were computed implicitly at the outer boundary.

5.2.2 Time Stepsize

As indicated in Ref. 1, a linear stability analysis shows that the implicit numerical algorithm is unconditionally stable for arbitrarily large values of the time step $\Delta\tau$. In practice, we have found that for a given type of flow, there is a limiting value of the time step beyond which the algorithm is unstable. The instability is attributed to nonlinear effects that are unaccounted for by linear stability theory. The evidence suggests that the instability may be associated with the streamwise coordinate direction $\xi(x)$ in which viscous effects are small and have been neglected in the governing equations (2.1). This hypothesis is based on the following observations.

Let $Co(\xi)$ denote the Courant number based on the inviscid flux vector $\hat{f}$ for the streamwise ξ direction

$$Co(\xi) = |\lambda|_{max} \, \Delta\tau/\Delta\xi \tag{5.1}$$

where λ is an eigenvalue of the Jacobian matrix $\hat{F}$ in Eq. (2.7d) and where the maximum is taken over all five eigeuvalues and over all grid points. The Courant numbers $Co(\eta)$ and $Co(\zeta)$ associated with the transverse directions η,ζ are similarly defined in terms of the eigenvalues of the Jacobian matrices $\hat{G}$ and $\hat{H}$.

One can show that most explicit algorithms for the Navier-Stokes equations are subject to the stability criterion

$$\max\{Co(\xi),\ Co(\eta),\ Co(\zeta)\} \leq 1 \tag{5.2}$$

as long as the grid is locally fine enough to resolve the steep flow gradients that exist within viscous regions such as wall boundary layers and mixing layers. Note that the transverse Courant numbers are usually much greater than the streamwise one because of the much smaller transverse physical grid spacing needed to resolve the steep transverse gradients that occur in viscous regions.

$$Co(\eta),\ Co(\zeta) >> Co(\xi) \tag{5.3}$$

In contrast, the implicit algorithm remains stable for $Co(\eta)$, $Co(\zeta) >> 1$. However, with no artificial implicit dissipation (see Sections 2.5 and 5.4), we have found that the implicit algorithm tends to become unstable when the streamwise Courant number is of the order of unity or greater

$$\left[Co(\xi)\right]_{unstable} \gtrsim O(1) \tag{5.4}$$

This still gives the algorithm a great advantage over explicit schemes. For relatively simple external and internal flows, one can obtain a crude estimate of the stable range of $\Delta\tau$ from Eq. (5.4) when $\xi = \xi(x)$ by using the approximation

$$Co(\xi) \approx c(1+M)\Delta\tau/\Delta x \tag{5.5}$$

where Δx is the physical grid spacing in the streamwise x direction and c and M are the dimensionless local sound speed and Mach number, respectively. For example, for external flows such as the flat plate boundary layer addressed earlier, the flow variables are referred to freestream conditions and Eq. (5.5) can be evaluated at the freestream boundary $c = c_\infty = 1$, $M = M_\infty$ using the smallest grid spacing $(\Delta x)_{min}$. For internal nozzle flows where the flow variables are referred to stagnation conditions, the streamwise grid is usually finest near the throat where $M \approx 1$, $c \approx \sqrt{2/(\gamma+1)}$.

External Flow Experiments

We have performed a few numerical experiments to investigate the effect of the time stepsize on the rate of convergence for the $M_\infty = 0.1$ adiabatic flat plate boundary layer problem described in Section 5.1.1. For a 15 x 15 ξ-ζ grid, the stable range of $\Delta\tau$ as estimated from Eq.'s (5.4) and (5.5) is

$$(\Delta\tau)_{stable} \lesssim 0.065$$

as noted in Section 5.1.1, the solution has been found to be stable for $\Delta\tau$ as large as $0.1\left[Co(\zeta) = 400\right]$ and unstable for $\Delta\tau = 0.5\left[Co(\zeta) = 2000\right]$. Table 5.1 summarizes convergence data obtained from two computations with stepsizes that differed by a factor of five within the stable range. The first column in the table gives the stepsize, and the second column gives the time step number n at which the data in the remaining columns apply. The third column gives the L_2

residual R, which is defined as the volume integral over the computational space of the square of the set of steady-state terms in the Navier-Stokes equations (2.1) and the smoothing terms, normalized by the total volume

$$R = (5\nu)^{-1}\int\left[\hat{f}_\xi+(\hat{g}-Re^{-1}\hat{\theta})_\eta+(\hat{h}-Re^{-1}\hat{\omega})_\zeta+\begin{pmatrix}\text{explicit}\\ \text{smoothing}\end{pmatrix}\right]^2 d\xi d\eta d\zeta \qquad (5.6)$$

$$\nu = \int d\xi d\eta d\zeta$$

The factor of one-fifth is introduced so that the residual represents an average over the five scalar components of the vector equation (2.1). The fourth column in the table lists the maximum relative change over the n'th step that occurred in any of the principal flow variables ρ, ρu, and ε at any point in the grid. During the later stages of convergence, this turns out to be the variable ρu at one of the interior grid points adjacent to the wall. Note that this quantity strongly affects the local velocity gradient and hence the computed wall shear stress. This means that the computed skin friction drag represents a very sensitive indicator of whether the solution actually has attained convergence. The data in the last two columns of Table 5-1 are derived from this value $|\Delta q/q|_{max}$. The fifth column contains an estimate of the instantaneous degree of unsteadiness in the solution

$$|q_\tau/q|_{max} \approx |(\Delta q/\Delta\tau)/q|_{max} = \frac{1}{\Delta\tau}|\Delta q/q|_{max} \qquad (5.7)$$

whereas in the last column, this quantity is scaled by the square of the time step.

From Table 5-1, one can see that, after a given number of time steps, the solution for the larger time step is much nearer convergence. All three measures of convergence, the residual, the maximum relative Δq, and the degree of unsteadiness q_τ/q, are much smaller for $\Delta\tau = 0.05$ than for $\Delta\tau = 0.01$. The entries in the last column of the table are nearly independent of the stepsize for a fixed number of time steps n. This implies that, during the late stages of the calculation where the solution is near steady state, the remaining degree of unsteadiness $|q_\tau/q|_{max}$ is inversely proportional to the square of the stepsize. We infer that the convergence rate is quadratic in the stepsize $\Delta\tau$, and that convergence is attained much more rapidly the larger the stepsize.

TABLE 5-1

Convergence Data for Adiabatic Flat Plate Boundary Layer, $M_\infty = 0.1$, $Re_\infty = 10^5$

Stepsize, $\Delta\tau$	Step Number, n	Residual, R	$\lvert\Delta q/q\rvert_{max}$	$\lvert q_\tau/q\rvert_{max}$	$(\Delta\tau)^2\lvert q_\tau/q\rvert_{max}$
0.01	137	1.53^{-9}	1.72^{-3}	1.72^{-1}	1.72^{-5}
0.05	137	7.90^{-11}	3.15^{-4}	6.3^{-3}	1.58^{-5}
0.01	300	9.70^{-10}	3.24^{-4}	3.24^{-2}	3.24^{-6}
0.05	300	1.11^{-11}	5.38^{-5}	1.08^{-3}	2.69^{-6}

Internal Flow Experiments

The time stepsize also has a strong effect on the convergence rate for internal flows. As an illustration, we present some results for a two-dimensional computation of internal laminar flow in the vertical symmetry plane of a so-called "two-dimensional" converging-diverging nozzle that has been tested experimentally in the static test facility of the NASA Langley 16-foot Transonic Wind Tunnel. The nozzle configuration is described in detail in Section 6.1. We note here only that the actual nozzle has straight sidewalls and a rectangular cross section of constant width. The inlet section is of constant height. This is followed by a straight-walled converging section that is connected to a straight diverging section by a circular arc that forms the geometric throat region.

The present two-dimensional flow test computation is for nozzle operating conditions corresponding to the nozzle design condition with a stagnation pressure of 1 atm. and a stagnation temperature of 295 Kelvin. The Reynolds number based on stagnation chamber conditions and throat half-height is 930,000. Although one would expect turbulent flow at this large a Reynolds number, the computation assumes laminar flow with a Sutherland viscosity law, a Prandtl number of 0.72, and adiabatic wall boundary conditions. The flow is computed in the upper half of the vertical plane of symmetry $y = 0$, $z \geq 0$, which is covered by a 23x15 grid in the x(j) and z(1) directions, respectively. The vertical (z) grid is stretched exponentially to resolve the nozzle wall boundary layer. The initial conditions used to start the computation were obtained in the same fashion as for the cosine nozzle test case discussed in Section 5.1.

Two computations were performed, each starting from the same initial conditions. The first case was run for 500 steps with a constant stepsize $\Delta\tau = 0.05$, which corresponds to a Courant number of 500 based on the minimum grid spacing in the z direction. The solution at step 500 is only partially converged, as can be seen from Figs. 5-6 and 5-7, which show the first two components of the "generalized force vector" $\vec{F}$ (see section 3) as a function of the time step counter NC. Figure 5-6 displays F_1 the net mass flow through the nozzle (i.e., the difference between the mass flows through the nozzle inlet and exit planes), normalized by the product of the stagnation density, stagnation sound speed, and the square of the nozzle throat half-height. The net mass flux should vanish at ateady state. The final mass flow is out of balance by over 1.2%, and it is apparent that the solution has not yet converged. The dimensionless thrust F_2 shown in Fig. 5-7 also shows some variation throughout the course of the run.

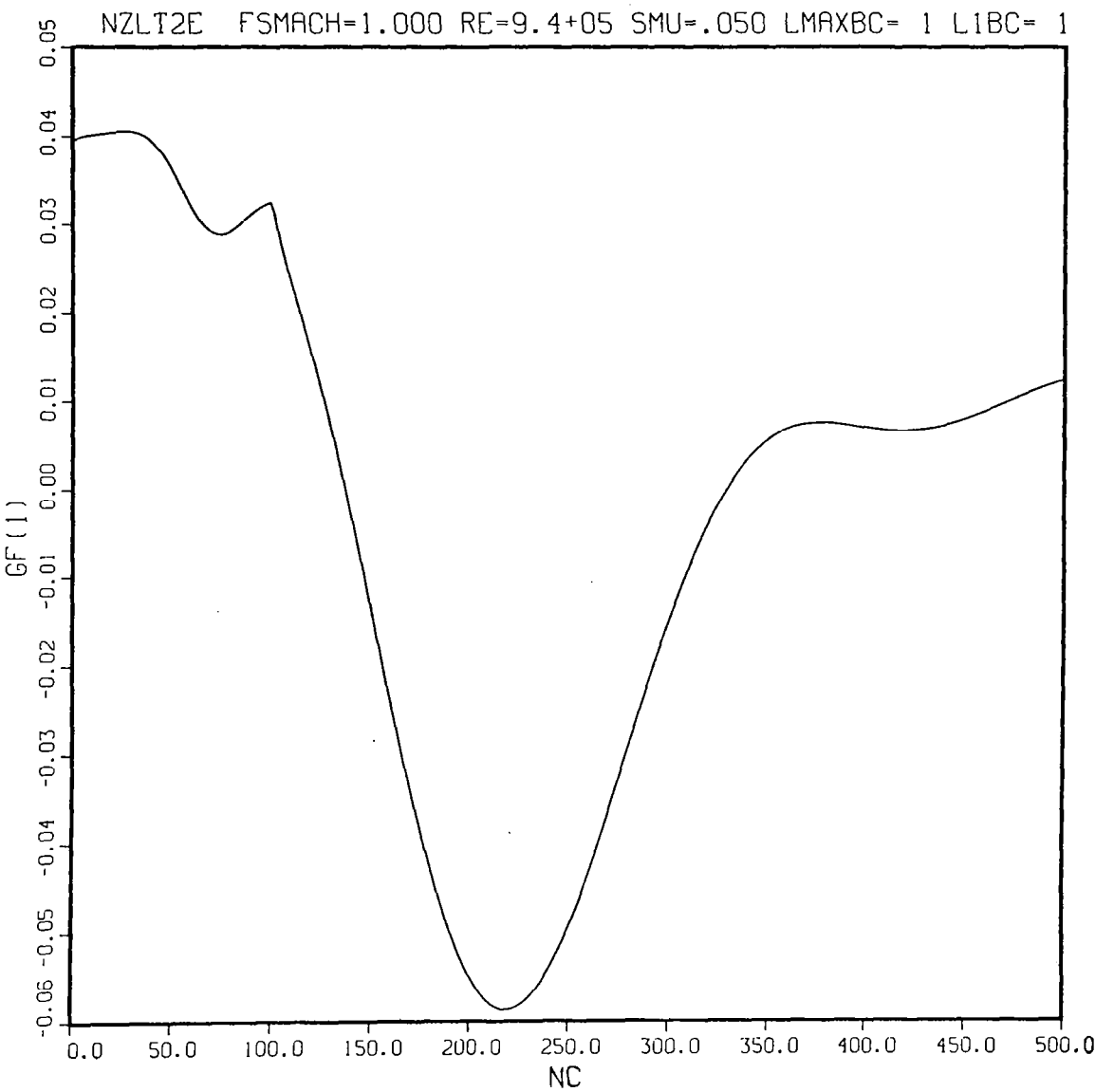

Figure 5-6 Convergence History of Net Mass Flow for 2-D Nozzle with Laminar Flow. Constant Time Stepsize $\Delta\tau$ = 0.05.

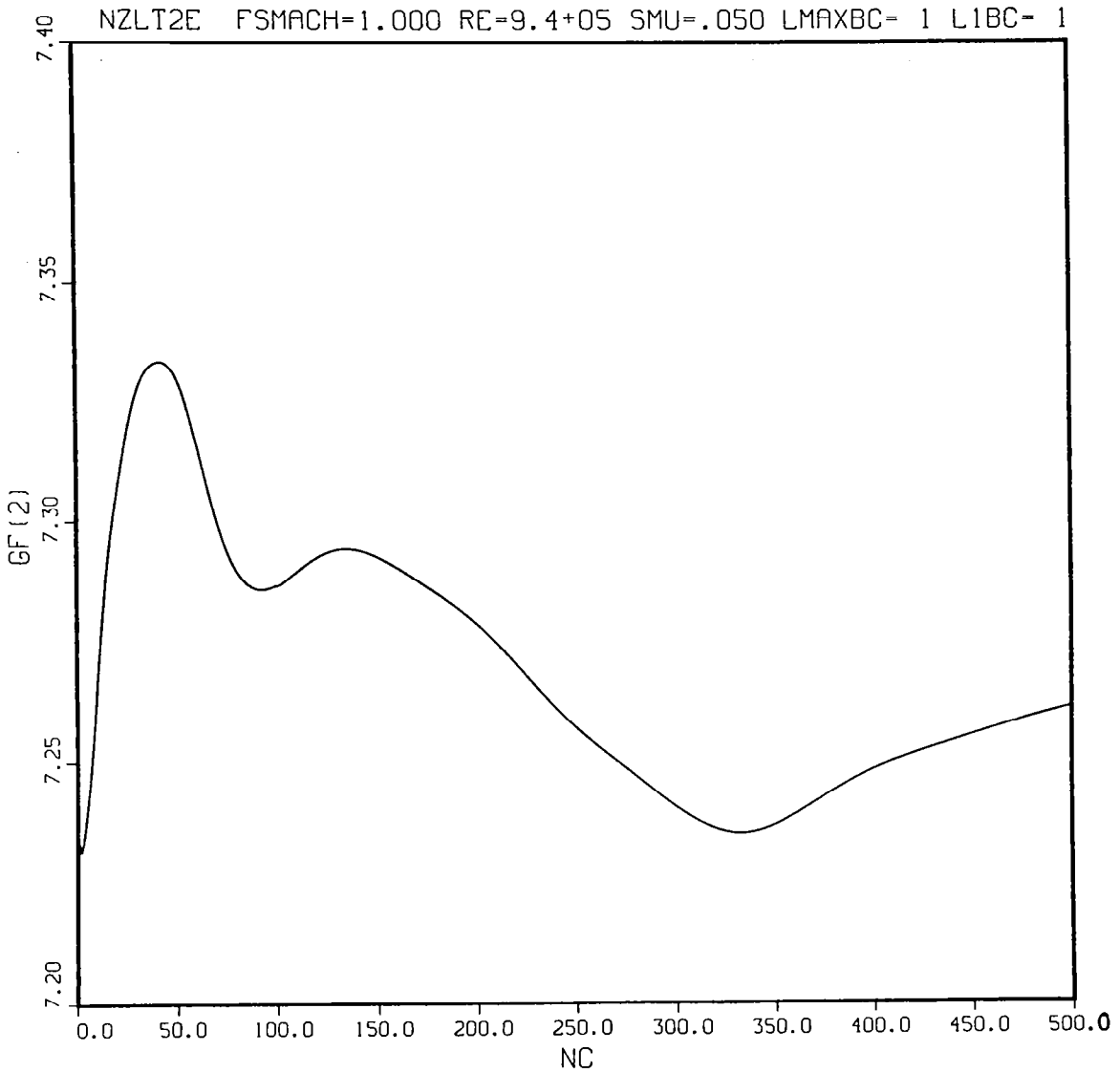

Figure 5-7 Convergence History of Net Thrust for 2-D Nozzle with Laminar Flow. Constant Time Stepsize $\Delta\tau$ = 0.05.

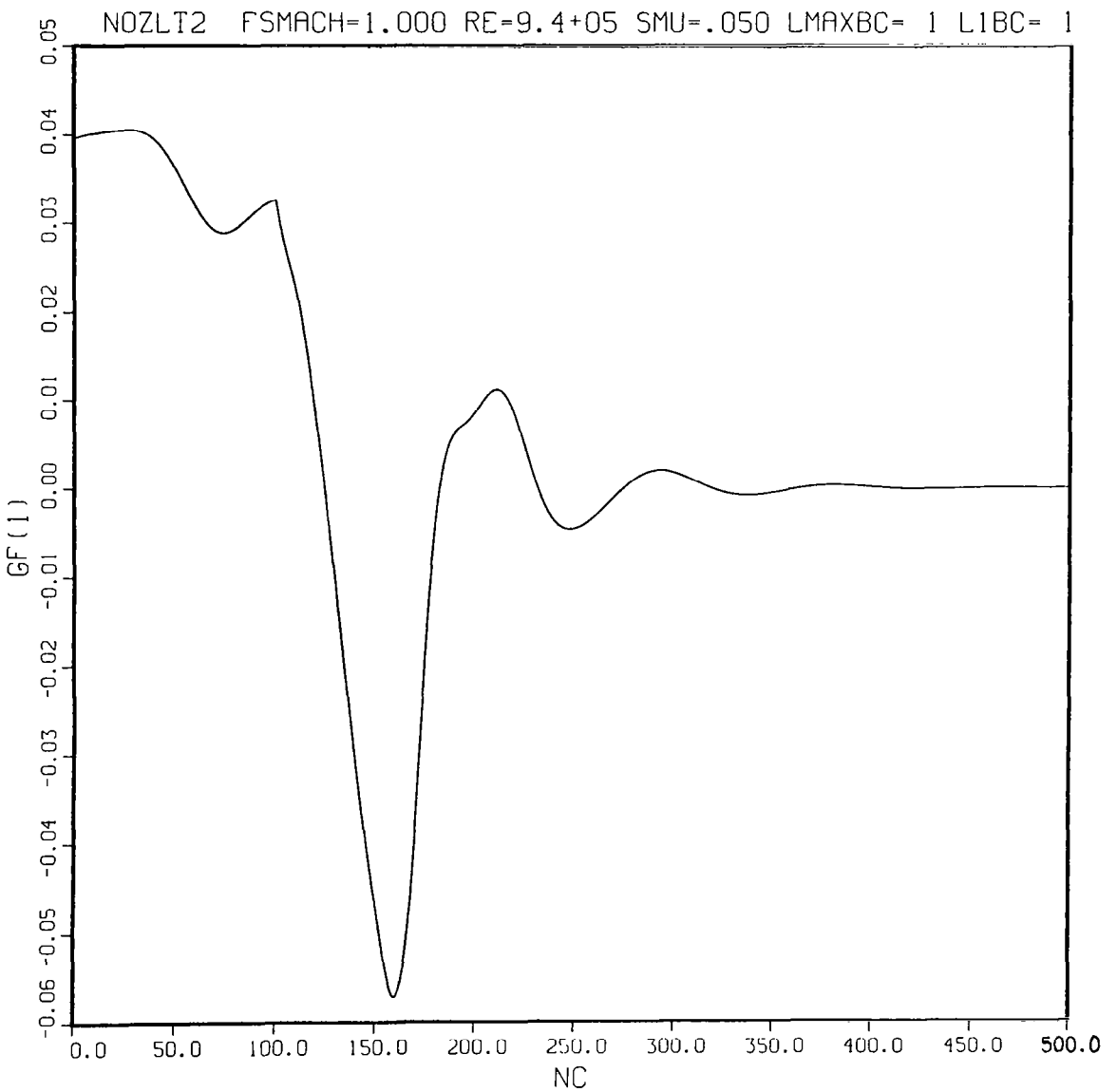

Figure 5-8 Convergence History of Net Mass Flow for 2-D Nozzle with Laminar Flow. Variable Time Stepsize Increasing from $\Delta\tau$ = 0.05 to 0.3.

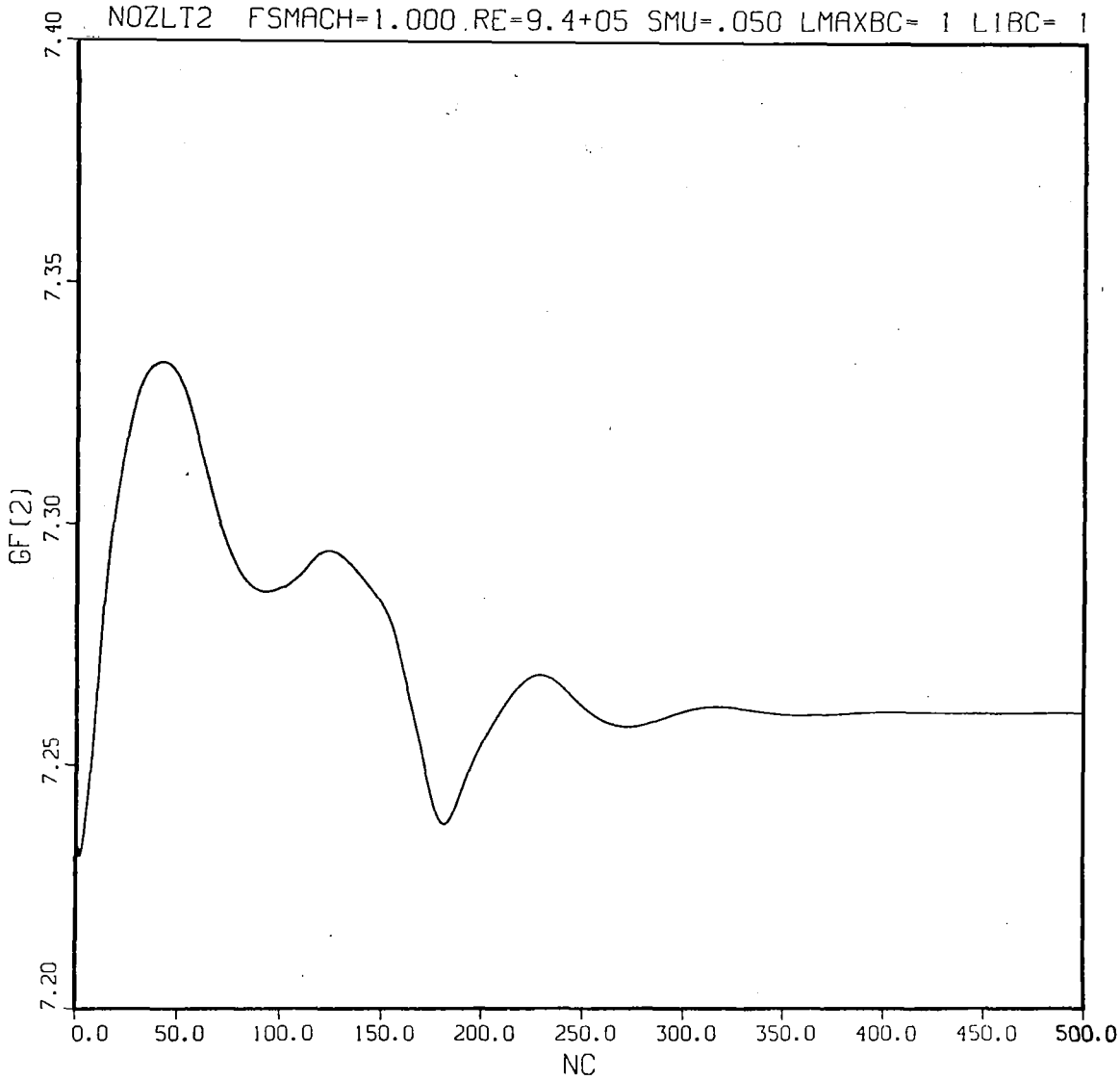

Figure 5-9 Convergence History of Net Thrust for 2-D Nozzle with Laminar Flow. Variable Time Stepsize Increasing from $\Delta\tau$ = 0.05 to 0.3.

Figures 5-8 and 5-9 display the corresponding results from a second 500 step run in which the stepsize $\Delta\tau$ was increased automatically by the factor 1.1 after each step during which the maximum relative change $|\Delta q/q|_{max}$ was less than 1%. The stepsize increased gradually from its initial value $\Delta\tau = 0.05$ to a maximum value $\Delta\tau = 0.3$ during the first 250 steps, and remained at that value for the remaining 250 steps. The largest stepsize $\Delta\tau = 0.3$ corresponds to a Courant number $Co(\zeta) = 2600$. The solution is essentially at steady state after 500 such increasing steps. The final net mass flow is out of balance ($F_1 = 0$) by less than 0.001%, and the thrust is steady to five significant figures. Additional results from this converged case are given later in Section 6.1 and compared with the wind tunnel data.

5.3 EFFECT OF ARTIFICIAL EXPLICIT SMOOTHING ON THE SOLUTION

Earlier numerical experiments with the implicit algorith showed that the solution is not entirely insensitive to the explicit fourth-order smoothing terms which are incorporated to control short wavelength spatial oscillations (Ref. 1, Sections 4.3 and 5.3). An array of numerical experiments has been performed to study parametrically the variation in the steady state solution when the magnitude of the smoothing coefficient is changed.

A set of three smoothing terms is added explicitly to the R.H.S. of Eq. (2.16a). Each term represents a conservative fourth-order difference operator acting in one of the three coordinate directions ξ,η,ζ. According to a linear stability analysis (Ref. 1, Section 4.3), the coefficients of these terms are subject to the stability criterion

$$8\sum_{i=1}^{N} (\beta_i \Delta\tau)\left[1+\kappa_i\right] \leq 1 \tag{5.8a}$$

$$\kappa_i = \frac{\Delta x_i}{2} \max_{x_i} \frac{\partial \ell n J}{\partial x_i} \tag{5.8b}$$

where x_i, $i = 1, 2, 3$ represent the three directions ξ,η,ζ, $\beta_i\Delta\tau$ denotes the smoothing coefficient for each direction, and $N = 2$ or 3 for two or three-dimensional flow. In the numerical implementation, the product $\beta_i\left[1+\kappa_i\right]$ is taken to be the same for all directions. The stability bound on the coefficient for each direction then is

$$\beta_i \Delta\tau \leq 1/8N(1+\kappa_i) \tag{5.9}$$

We define a relative smoothing coefficient SMU as

$$SMU = \beta_i \Delta\tau/(\beta_i \Delta\tau)_{max} \tag{5.10}$$

where $(\beta_i \Delta\tau)_{max}$ denotes the upper bound obtained by invoking the equality in (5.9). The quantity SMU is used as an input to the computer program to specify the smoothing coefficient $(\beta_i \Delta\tau)$ for each direction as a fraction of the maximum stable value determined by inequality (5.9)

$$\beta_i \Delta\tau = SMU/8N(1+\kappa_i) \quad , \quad 0 \leq SMU \leq 1 \tag{5.11}$$

Note that, for a fixed value of SMU, the magnitude of the explicit smoothing terms relative to the actual spatially differentiated terms in the Navier-Stokes equations (2.1) depends upon the time stepsize $\Delta\tau$. The reason is that the smoothing terms are appended to the R.H.S. of Eq. (2.16a), in which the true spatially differentiated terms of the Navier-Stokes equations are multiplied by the factor $\Delta\tau$. This fact has been accounted for in Eq. (5.8) by defining the coefficient $(\beta_i \Delta\tau)$ of the smoothing term for each direction to include $\Delta\tau$ as a factor. The magnitudes of the artificial smoothing terms relative to the actual terms in the Navier-Stokes equations then depends on the quantities β_i, and would be independent of the time stepsize if each β_i were taken as constant and independent of $\Delta\tau$. However, this would cause the stability criteria (5.8) or (5.9) to be violated for sufficiently large values of $\Delta\tau$. In terms of the quantity SMU, the stability criteria require that the coefficient $\beta_i \Delta\tau$ satisfy Eq. (5.11). Since β_i itself governs the magnitude of the artificial smoothing terms relative to the actual Navier-Stokes terms, it follows from Eq. (5.11) that these relative magnitudes will be preserved under a change in $\Delta\tau$ only when the ratio $SMU/\Delta\tau$ is held fixed, rather than when SMU itself is held fixed. That is, the ratio $SMU/\Delta\tau$ and not SMU itself governs the relative magnitudes of the smoothing terms and the true Navier-Stokes terms.

We have performed an array of numerical experiments for the adiabatic flat plate laminar flow problem to determine the sensitivity of the steady-state solution to the magnitude of the smoothing strength $SMU/\Delta\tau$ for a range of freestream Mach numbers $0.1 \leq M_\infty \leq 3$. The Reynolds number is 10^5, the Prandtl number is unity, and viscosity is proportional to the temperature.

Table 5-2 displays the variation in the computed steady-state drag coefficient C_D with smoothing coefficient for various freestream Mach numbers. For each M_∞, the last column in the table gives the percentage by which the drag coefficient for a given value of $SMU/\Delta\tau$ differs from the drag computed with $SMU/\Delta\tau = 1$. The results indicate that the solution is fairly insensitive to the magnitude of the smoothing coefficient, except at the lowest Mach number considered. For very low-speed flows, it appears that the accuracy of the solution is degraded significantly unless the ratio $SMU/\Delta\tau$ is of the order of unity or less.

The smoothing coefficient also was observed to have some effect on the rate of convergence to steady state at both the lowest and highest Mach numbers considered. Transient oscillations in C_D were damped out somewhat more quickly with $SMU/\Delta\tau = 10$. In the supersonic case, $M_\infty = 3$, such behavior is to be expected because the smoothing terms supply the dissipative mechanism that enables computation of the embedded shock wave induced by the displacement effect of the viscous boundary layer [see Ref. 1, Section 5.2].

5.4 EFFECT OF ARTIFICIAL IMPLICIT DISSIPATION ON STABILITY AND CONVERGENCE

It has been noted in Section 5.2.2 above that, for the "parabolized" Navier-Stokes equations (2.1) wherein the viscous terms associated with the streamwise coordinate ξ are neglected, the implicit algorithm tends to become unstable for large time steps $\Delta\tau$ at which the streamwise Courant number $Co(\xi)$ is much greater than the order of unity. We have performed some numerical experiments which show that the introduction of artificial implicit dissipation (see Section 2.4) extends the regime of stability to Cournat numbers $Co(\xi) >> 1$ when the dissipation coefficient α is of the order of unity. This allows steady-state solutions to be attained in fewer time steps because the rate of convergence is generally greater the larger the time stepsize.

The results of these experiments for adiabatic flat plate laminar flow at various freestream Mach numbers are summarized in Table 5-3. The table contains the results of two runs for each Mach number M_∞. The first run employed no implicit dissipation ($\alpha = 0$) and a stepsize $\Delta\tau$ for which the streamwise Courant number $Co(\xi)$ is of the order of unity. The second run used a dissipation coefficient $\alpha = 1$ and a variable step $\Delta\tau$, starting with the same initial flowfield and the same initial values of $\Delta\tau$ and SMU (the explicit smoothing coefficient) as in the first run. The time step during the second run was increased automatically by the factor

TABLE 5-2

Effect of Explicit Smoothing Coefficient on Steady State Drag Coefficient Adiabatic

Flat Plate, $Re_\infty = 10^5$, $Pr = 1$, $\mu_e = T$

Mach No. M_∞	$\Delta\tau$	SMU	SMU/$\Delta\tau$	$C_D \times 10^3$	% Variation
0.1	0.05	0.5	10	4.1423	+3.7
		0.05	1	3.9940	0.0
		0.005	0.1	3.9831	-0.27
0.8	0.05	0.5	10	4.0727	+0.45
		0.05	1	4.0546	0.0
		0.005	0.1	4.0529	-0.04
3.0	0.01	0.1	10	4.6633	+0.7
		0.01	1	4.6309	0.0
		0.001	0.1	4.6287	-0.05

TABLE 5-3

Effect of Implicit Dissipation ($\alpha>0$) on Stability and Convergence of Adiabatic Flat Plate*

Boundary Layer Computations $Re_\infty = 10^5$, $Pr = 1$, $\mu = T$

M_∞	α	$\Delta\tau_i$	$\Delta\tau_f$	$Co_f(\xi)$	$Co_f(\zeta)$	$(SMU/\Delta\tau)_f$	$C_{Df} \times 10^3$	$(NC)_f$	$(NC)_s$
0.1	0	5^{-2}	5^{-2}	0.77	2.0^{+2}	1.0	3.9940	1	277
	1	5^{-2}	2.4^{+2}	3.7^{+3}	9.8^{+5}	3.3^{-3}	3.9894	94	139
0.8	0	5^{-2}	5^{-2}	1.25	2.0^{+2}	1.0	4.0546	1	42
	1	5^{-2}	1^{+2}	2.5^{+3}	4.1^{+5}	8.0^{-3}	4.0608	85	36
1.5	0	3^{-2}	3^{-2}	1.0	1.3^{+2}	1.0	4.1825	1	89
	1	3^{-2}	70	2.3^{+3}	2.9^{+5}	8.8^{-2}	4.2028	93	122

* All runs were for 200 steps

1.1 following each step during which $|\Delta q/q|_{max}$ was less than 1%, until the time stepsize reached a pre-assigned maximum value $\Delta\tau_f$, at which point the stepsize was held fixed for the remainder of the run. Whenever $\Delta\tau$ was raised in this fashion, the explicit smoothing coefficient SMU also was raised by the same factor until it reached a maximum value SMU = 0.8. The latter bound was imposed to avoid violating the stability criterion for the smoothing terms [Eq. (5.11) of Section 5.3]. The various columns in Table 5-3 list in order the freestream Mach number M_∞; the initial and final stepsizes $\Delta\tau_i$ and $\Delta\tau_f$; the streamwise Courant number $Co_f(\xi)$ as estimated from Eq. (5.5) using $\Delta\tau_f$; the Courant number $Co_f(\zeta)$ based on $\Delta\tau_f$, on the maximum eigenvalue of $\partial\hat{h}/\partial\hat{q}$, and on the minimum grid spacing in the wall normal direction; the final value of the explicit smoothing strength $(SMU/\Delta\tau)_f$; the final drag coefficient C_{Df} at the last time step of the run; the time step index $(NC)_f$ at which the time stepsize reached its maximum value $\Delta\tau_f$; and the time step index $(NC)_s$ at which the drag coefficient first attained a value within $\pm 0.1\%$ of C_{Df} and stayed in that range for the remainder of the run. This last entry in the table has been included merely to provide some quantitative measure of the convergence rate. Note that, for a given M_∞, the final values of C_{Df} differ slightly between the runs with fixed and variable stepsize $\Delta\tau$ because the ratio $(SMU/\Delta\tau)_f$ could not be held fixed and still satisfy the stability criterion (5.11) in the variable-step run.

For each freestream Mach number in the table, a run of fixed stepsize $\Delta\tau$ for which $Co(\xi) \approx 10$ was attempted without implicit dissipation ($\alpha = 10$) and was found to be unstable. In contrast, all of the variable-step runs with $\alpha = 1$ remained stable and converged rapidly for a maximum value of $Co_f(\xi) \approx 3000$. The drag coefficient histories for these three runs are displayed in Figs. 5-10 to 5-12. We haven't determined the maximum value of $Co(\xi)$ that can be attained with $\alpha = 1$ for various Mach numbers. However, an attempted variable-step run at $M_\infty = 0.1$ with no pre-assigned bound on $\Delta\tau$ eventually became unstable at a value $Co(\xi)$ somewhat in excess of 4000.

Implicit dissipation is potentially useful only for obtaining steady-state solutions. The artificial terms destroy the time-accuracy of the computation and lead to a physically unrealistic transient behavior. Neither does the implicit dissipation always ensure either stability or faster convergence to steady state. For

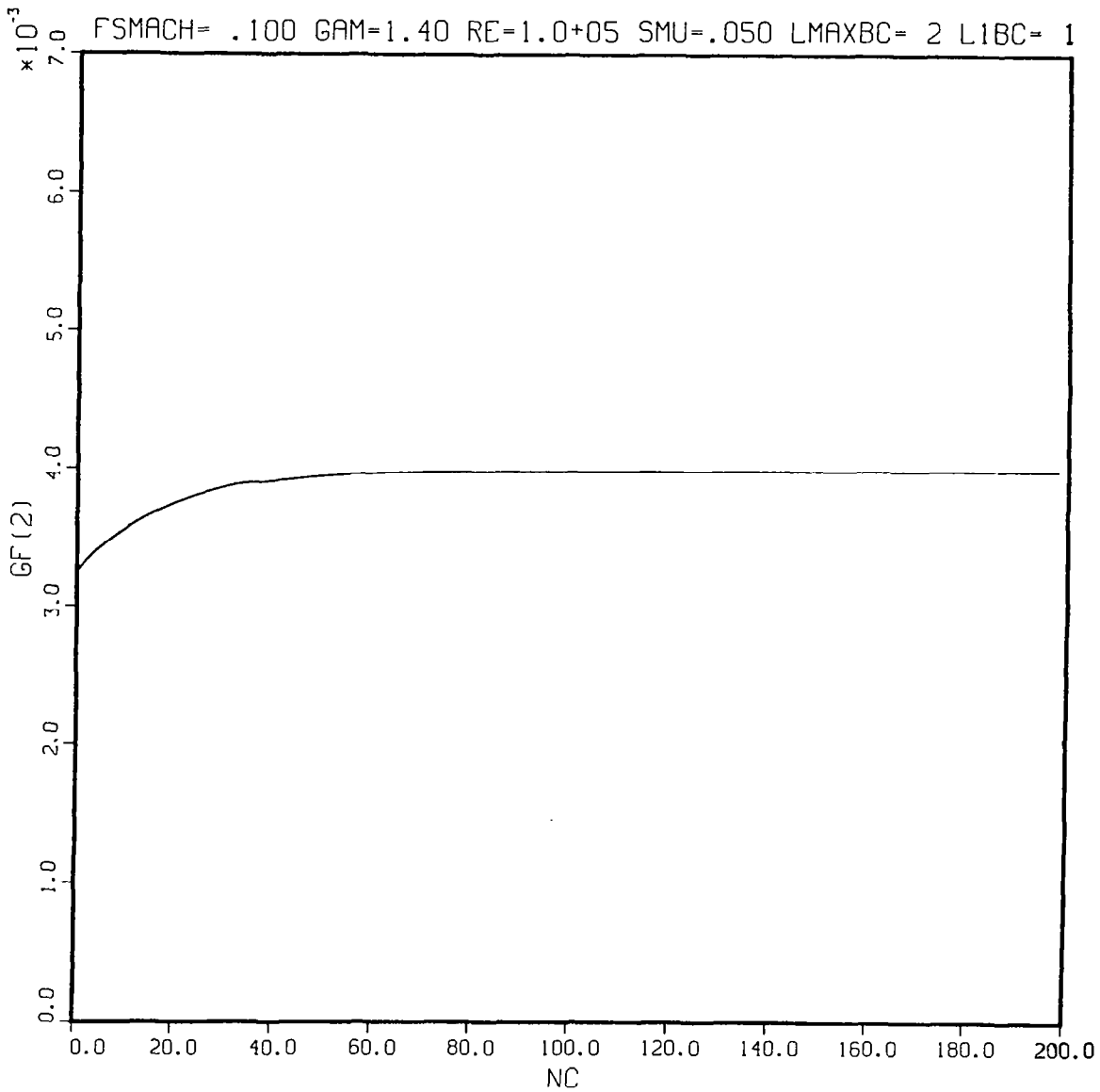

Figure 5-10 Flat Plate Drag Coefficient History Computed with Implicit Dissipation $\alpha = 1$, $(\Delta\tau)_{max} = 240$. $M_\infty = 0.1$, $Re_\infty = 10^5$.

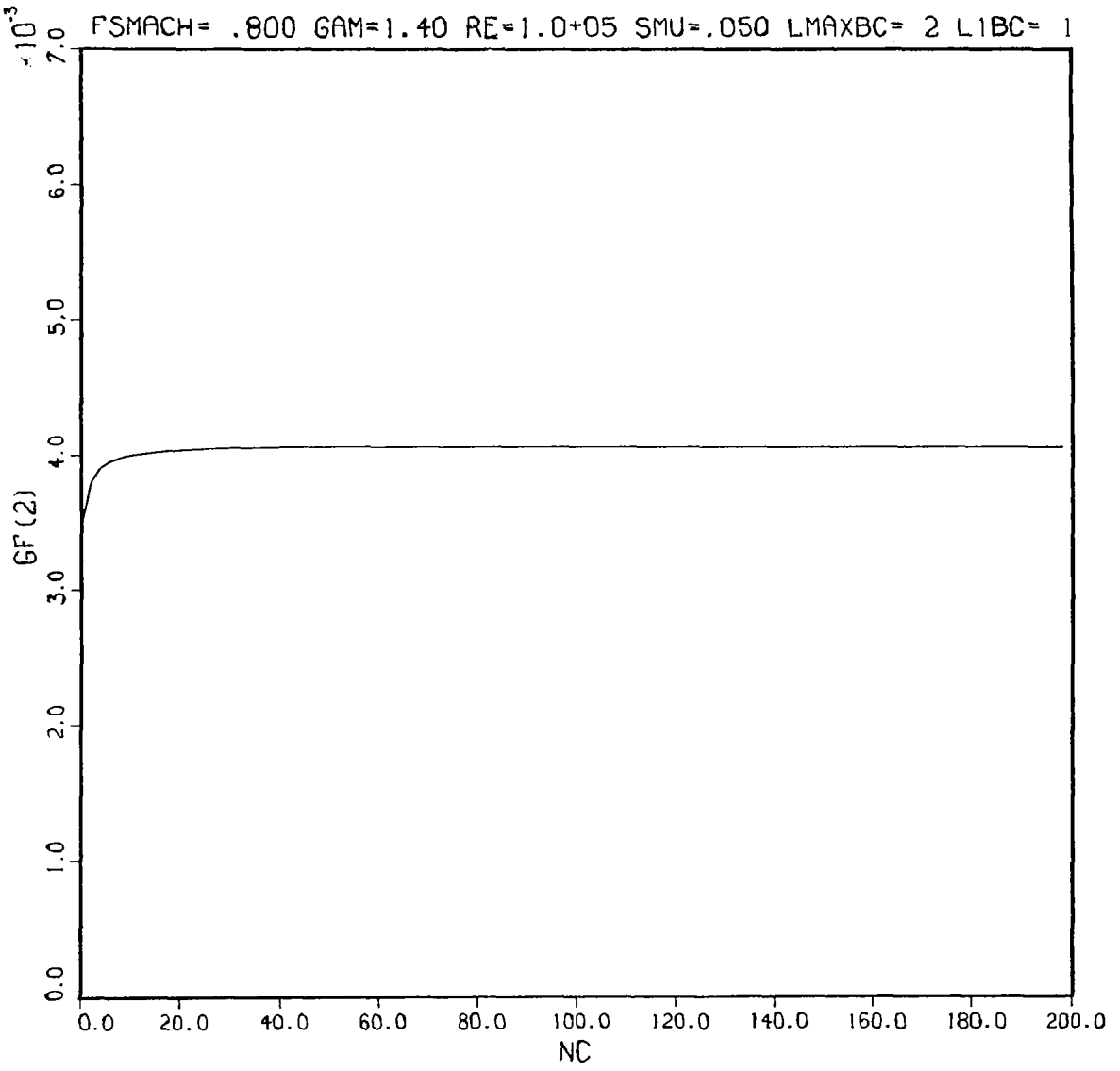

Figure 5-11 Flat Plate Drag Coefficient History Computed with Implicit Dissipation $\alpha = 1$, $(\Delta\tau)_{max} = 100$. $M_\infty = 0.8$, $Re_\infty = 10^5$.

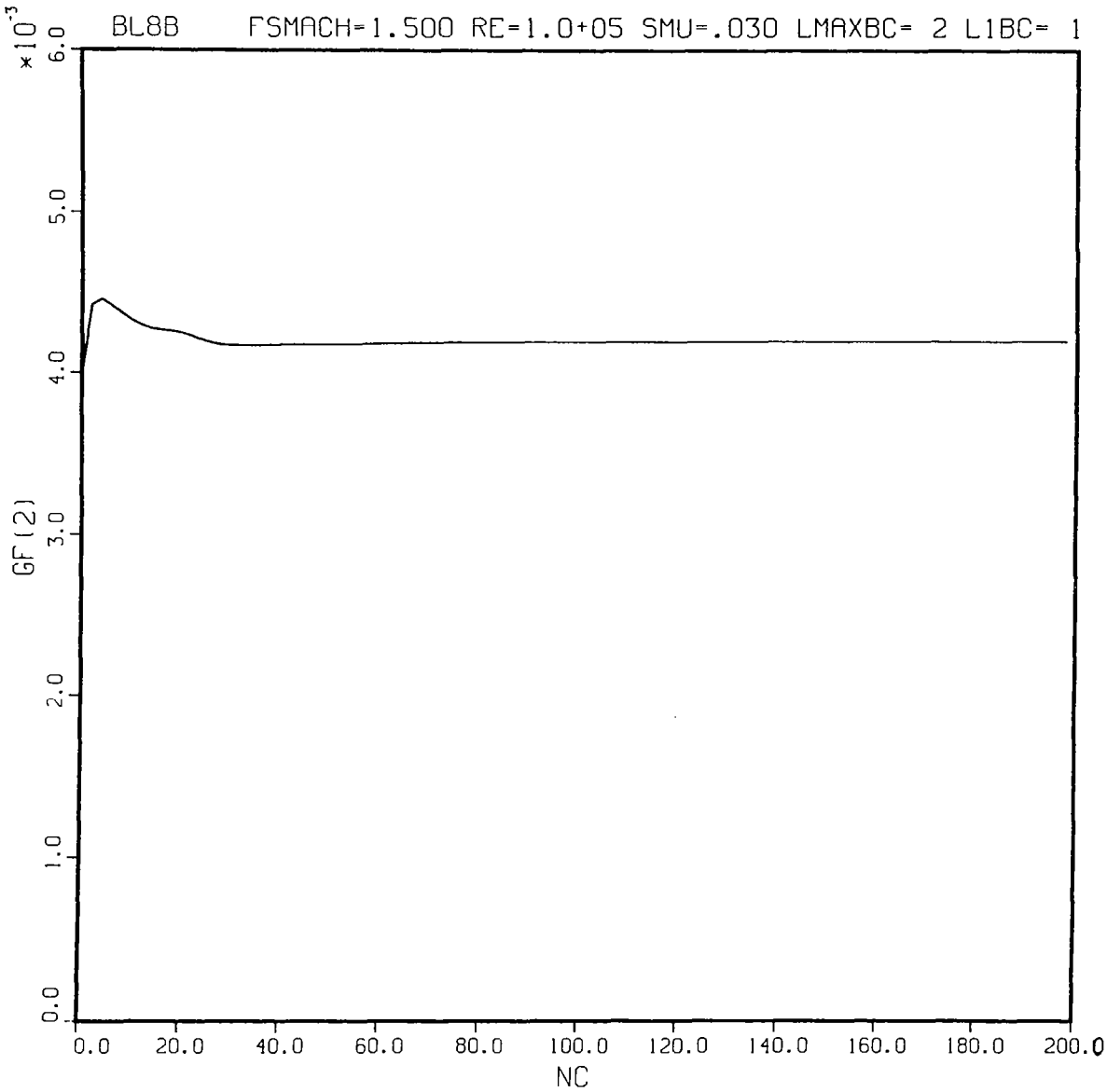

Figure 5-12 Flat Plate Drag Coefficient History Computed with Implicit Dissipation $\alpha = 1$, $(\Delta\tau)_{max} = 70$. $M_\infty = 1.5$, $Re_\infty = 10^5$.

example, we performed a run at $M_\infty = 3$ using $\alpha = 1$ and a constant stepsize $\Delta\tau = 0.01\left[Co(\xi) = 0.56\right]$ that failed to reach steady state in 200 steps; whereas, as indicated in line 5 of Table 5-3, the corresponding run with $\alpha = 0$ converged adequately in the same number of steps. A similar run for $M_\infty = 3$ with an increasing stepsize became unstable at $\Delta\tau = 0.02$. This suggests that the implicit dissipation described in Section 2.4 may have a destabilizing effect for supersonic flows with embedded shock waves. In another example, an internal nozzle flow computation starting from very crude initial flowfield conditions proved unstable with $\alpha = 1$ for a small, fixed stepsize $\Delta\tau\left[Co(\xi) \approx 1\right]$, but was stable with $\alpha = 0$. In the light of the results shown in Table 5-3, these examples suggest that the implicit dissipation can enhance both stability and convergence for subsonic and transonic flows if very large time steps are employed, and if the initial conditions either are approximately correct, or are first regularized by a short preliminary run with $\alpha = 0$ using shorter time steps. The applicability of implicit dissipation to supersonic flows with embedded shock waves requires further investigation.

5.5 CONCLUSIONS

The principal conclusions that have emerged from the numerical experiments described in the preceding subsections are summarized below.

1. It has been demonstrated that the implicit numerical method is capable of computing viscous flows with boundary layer separation.
2. Implicit boundary conditions are superior to explicit time-lagged boundary conditions in that they allow the use of larger time stepsize without numerical instability. For external flows, implicit freestream boundary conditions wherein the momentum components transverse to the boundary are computed implicitly from the transverse momentum equations are vastly superior to the simple method where all freestream conditions are imposed at the freestream boundary. The latter conditions retard convergence to steady state, and seriously degrade the accuracy of the computed flowfield.
3. In general, larger time stepsizes give faster convergence to steady state. Although a linear stability analysis indicates the implicit algorithm to be unconditionally stable, experience indicates that the algorithm tends to become unstable at time stepsizes for which the streamwise Courant number exceeds the order of unity. Numerical experiments indicate that, within the stable range, the convergence rate is quadratic in the time stepsize.

4. The algorithm involves artificial explicit fourth order smoothing terms. Numerical experiments show that the accuracy of the solution is fairly insensitive to the magnitude of the smoothing coefficient, except for very low-speed subsonic flows. For such flows, the accuracy is degraded significantly unless the ratio of the smoothing coefficient to the time stepsize is of the order of unity or less.
5. Numerical experiments indicate that, under favorable conditions, the introduction of artificial implicit dissipation extends the regime of numerical stability to streamwise Courant numbers far in excess of unity. This yield faster convergence to steady state when large time stepsizes are used ($Co \gg 1$). However, the implicit dissipation must be used with caution. It destroys the time-accuracy of the solution and cannot be employed in cases where the unsteady behavior of the flow is of interest. The present numerical experiments suggest that the implicit dissipation is most effective for subsonic and transonic flows. Further investigation is recommended to study its behavior for supersonic flow with embedded shock waves.

SECTION 6

NOZZLE FLOWFIELD PREDICTIONS AND COMPARISON WITH EXPERIMENTAL DATA

Laminar and turbulent flowfield computations have been performed for several three-dimensional nozzles that have been tested experimentally in the NASA Langley 16-foot Transonic Wind Tunnel. The first computation is for internal flow in a so-called "two-dimensional" converging-diverging nozzle with flat sidewalls and a rectangular cross-section. The second computation is for the combined internal and external flowfields of a circular, converging nozzle in a high subsonic external flow. The results of these computations are presented below.

6.1 Internal Flow in a "Two-Dimensional" Converging-Diverging Nozzle

6.1.1 Configuration, Operating Conditions, and Computational Grid

The nozzle configuration and dimensions are shown in Fig. 6-1. The configuration is bilaterally symmetric with flat sidewalls and a rectangular cross section. The inlet section is of constant height. This is followed by a straight-walled converging section that is connected to a straight-walled diverging section by a circular arc that forms the geometric throat region. The exit-to-throat area ratio is 1.0891 for a design exit Mach number of 1.35. The corresponding design exit pressure and temperature from one-dimensional isentropic flow theory are $p = 0.337$ and $T = 0.733$, normalized by the stagnation chamber pressure and temperature, respectively. The operating conditions correspond to the design condition with a stagnation pressure of 1 atm. and a stagnation temperature of 295 Kelvin. The Reynolds number based on stagnation conditions and throat half-height is 9.3×10^5 as computed from the Sutherland viscosity law. The working fluid is air ($\gamma = 1.4$, $Pr = 0.72$).

For the flow computation, the origin of the Cartesian coordinate system is positioned at the geometric center of the throat. The x axis coincides with the intersection of the vertical and horizontal symmetry planes.

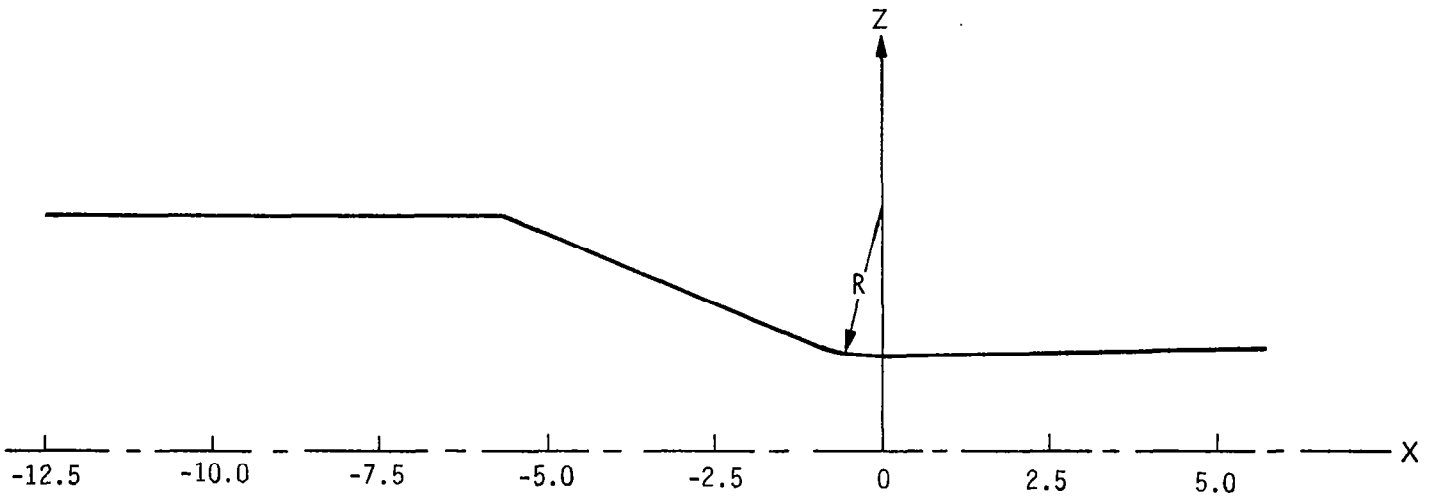

NOZZLE WIDTH = 10.16 cm

R = 2.7374 cm

EXIT AREA RATIO = 1.0891

	COORDINATES (cm.)	
	X	Z
	-5.7785	3.5202
	-1.0401	1.5740
THROAT	0.0	1.3686
	0.0579	1.3693
	5.7785	1.4905

Figure 6-1 Configuration and Coordinates of Two-Dimensional Nozzle

The latter coincide with the coordinate planes $y = 0$ and $z = 0$. Symmetry boundary conditions are applied at these planes, and the flow is computed in the quarter-space $y \geq 0$, $z \geq 0$. The inflow boundary is positioned at $x = -4$ in., and the outflow boundary is at the nozzle exit. The flow region between these planes, the symmetry planes, and the nozzle walls is covered by a 23 x 10 x 15 grid in the x, y, and z directions, respectively. The streamwise (x) grid spacing is nonuniform with a relatively fine spacing near the throat, and the grid in each cross-sectional plane is exponentially stretched in both the y and z directions to resolve the wall boundary layers. The computational coordinate system thus has the form $\xi = \xi(x)$, $\eta = \eta(y)$, $\zeta = \zeta(z)$. The transverse grid spacings Δy, Δz are several thousand times smaller at the walls than at the symmetry planes. Side and end views of the grid are displayed in Fig. 6-2a and 6-2b, and an orthographic projection of the three-dimensional grid is given in Fig. 6-2c. All dimensions shown are referred to the throat half-height.

Laminar and turbulent flow computations have been performed for two-dimensional flow in the vertical plane of symmetry, and a laminar flow calculation has been performed on the three-dimensional grid shown in Fig. 6.2. All computations employ adiabatic wall boundary conditions. Initial conditions are obtained as follows. The inviscid core flow is obtained from one-dimensional isentropic flow theory for the nozzle area variation. These core flow conditions are applied over the central part of the grid in each cross-sectional plane $1 \leq \ell \leq \ell_{max}/2$, assuming that the local velocity vector is oriented along the streamwise grid lines. Velocities on the remaining part of the grid are linearly interpolated in k and ℓ to zero at the walls. Pressure is taken as uniform over each cross-sectional plane. Temperature in the nonuniform velocity region near the walls is obtained from velocity through the Crocco relation, and density follows from the equation of state. The resulting total pressure, total temperature, and transverse (v, w) distributions over the inflow plane are used as inflow boundary conditions for the flowfield computation (see Section 2.3.1). The numerical results of the computations are presented below in dimensionless form. Dimensions are referred to the throat half-height, which is the reference length in terms of which the Reynolds

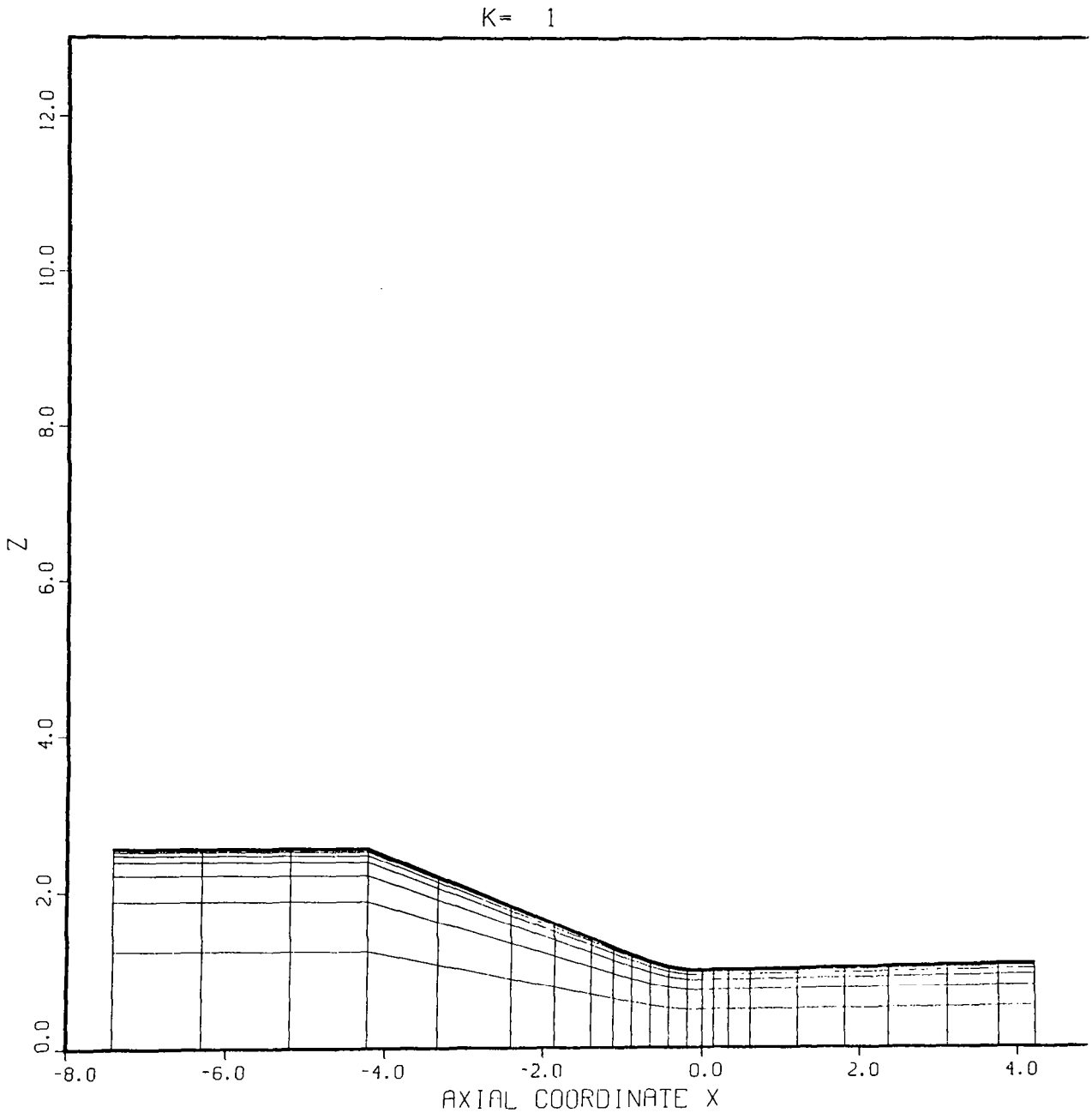

Figure 6-2a Side View of Computational Grid for Two-Dimensional Nozzle

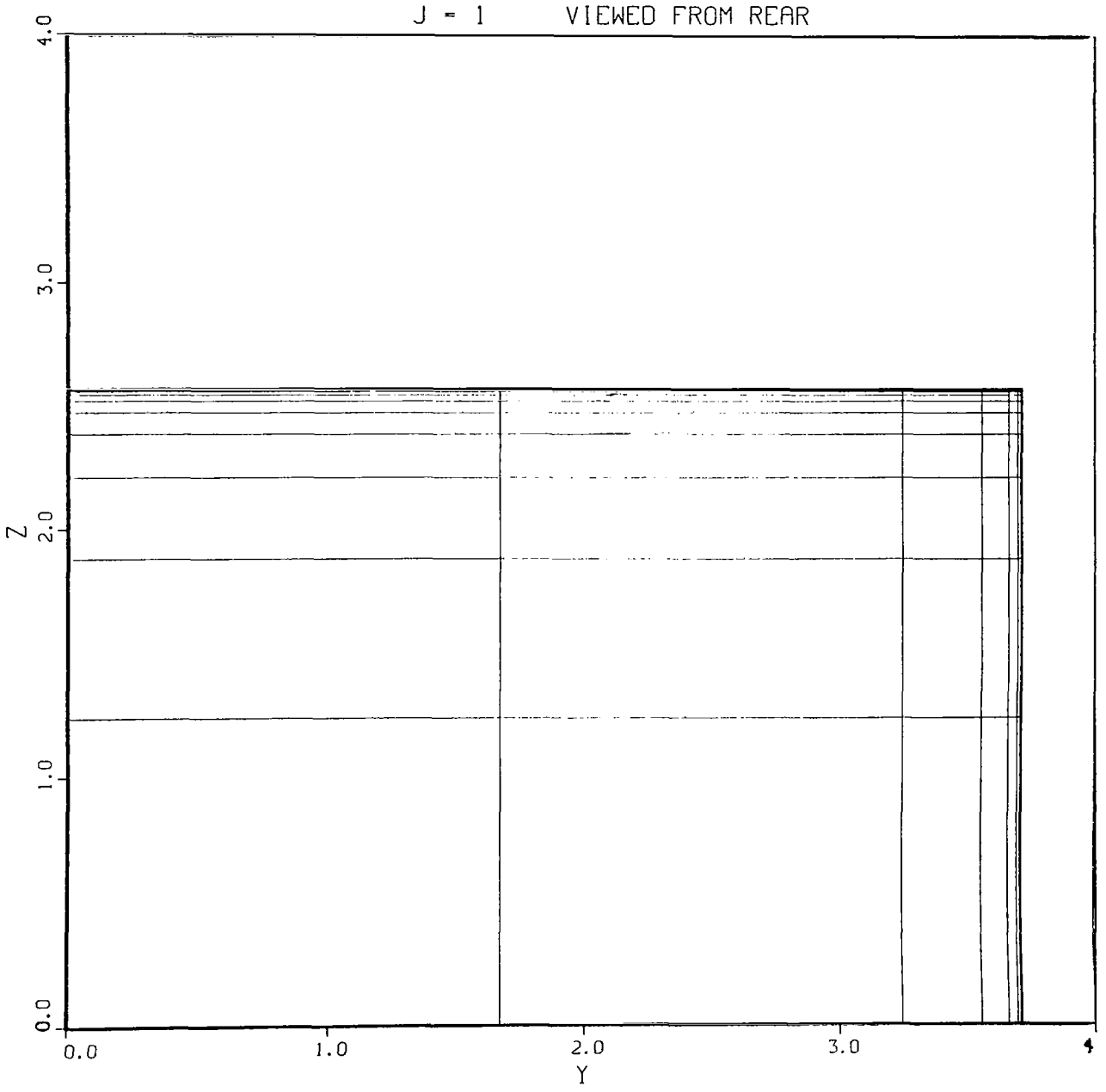

Figure 6-2b End View of Computational Grid for Two-Dimensional Nozzle

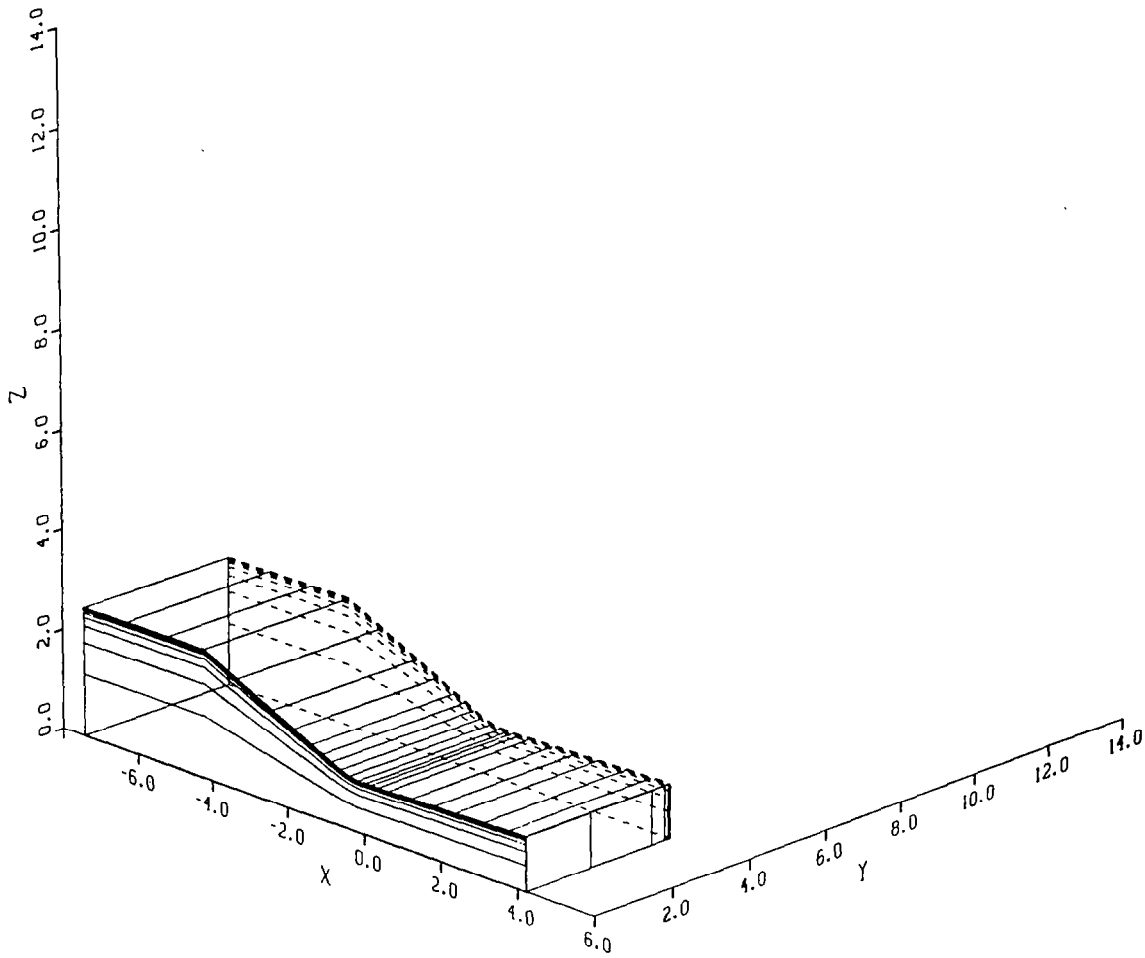

Figure 6-2c Orthographic View of Grid for Two-Dimensional Nozzle

number is defined. Pressure, density, and temperature are referred to the corresponding stagnation conditions, and velocities are referred to the stagnation sound speed.

6.1.2 Two- Dimensional Flow Results

Laminar Flow

The convergence history of this laminar flow computation has already been discussed in Section 5.2. Convergence was attained in 500 variable time steps. The first 100 of these were of constant size $\Delta\tau = 0.05$, the next 70 were of increasing size, and the final 280 were constant at $\Delta\tau = 0.3[Co(\zeta) = 2600]$. The computation took about 3 1/2 min. of CPU time on a CDC 7600 machine. The computed discharge coefficient is $C_w = 0.9972$, and the dimensionless thrust is 7.2612. The latter is referred to $\rho_0(c_0L)^2/2$ where the subscript denotes stagnation conditions, c is the sound speed, and L is the reference length (the throat half-height).

The nozzle wall pressure distribution is shown in Fig. 6-3, along with preliminary experimental data from the wind tunnel test (Ref. 10). The two sets of data represent pressure measurements on the upper and lower walls of the test nozzle. The computed pressure distribution has the same qualitative behavior as the data, including a slight recompression downstream of the geometric throat. The computation is in good quantitative agreement with the data in the subsonic and transonic region, but systematically under-predicts the data by about 5% in the supersonic region downstream of the throat. We shall see later that a turbulent flow computation agrees slightly better with the data in this region.

The computed pressure distributions along the wall and the nozzle center-line displayed in Fig. 6-4 show a substantial difference in the subsonic and transonic region.

Turbulent Flow

The turbulent flow computation employed the converged laminar flowfield as initial conditions. The initial stepsize $\Delta\tau = 0.05$ increased by a factor of 6 over the first 75 steps and was held constant for 325 more steps,

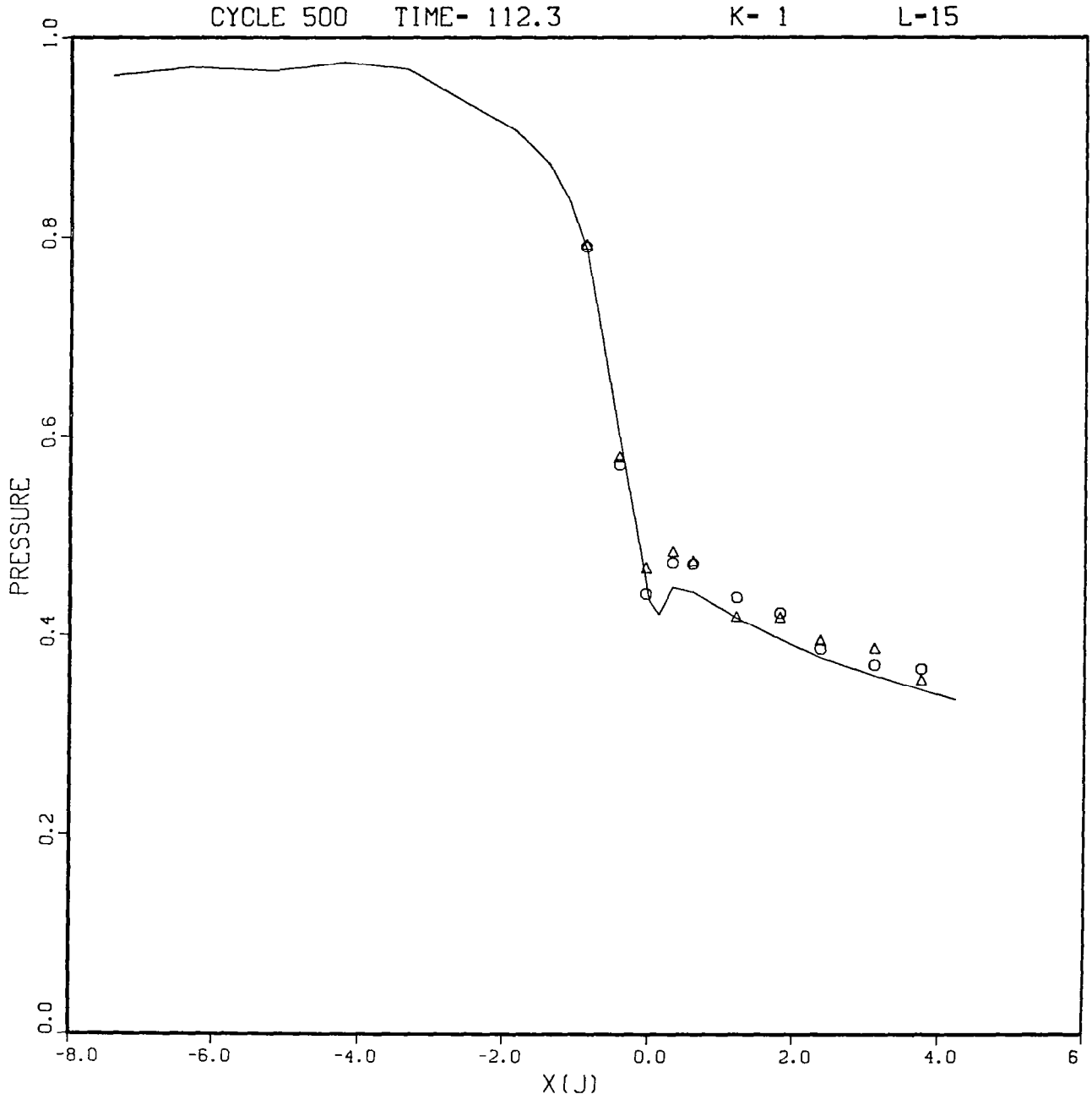

Figure 6-3 Comparison of 2-D Laminar Flow Wall Pressure Distribution With Experimental Data of Ref. 10. Data Points: Circles, Upper Flap; Triangles, Lower Flap. Computation: Solid Line.

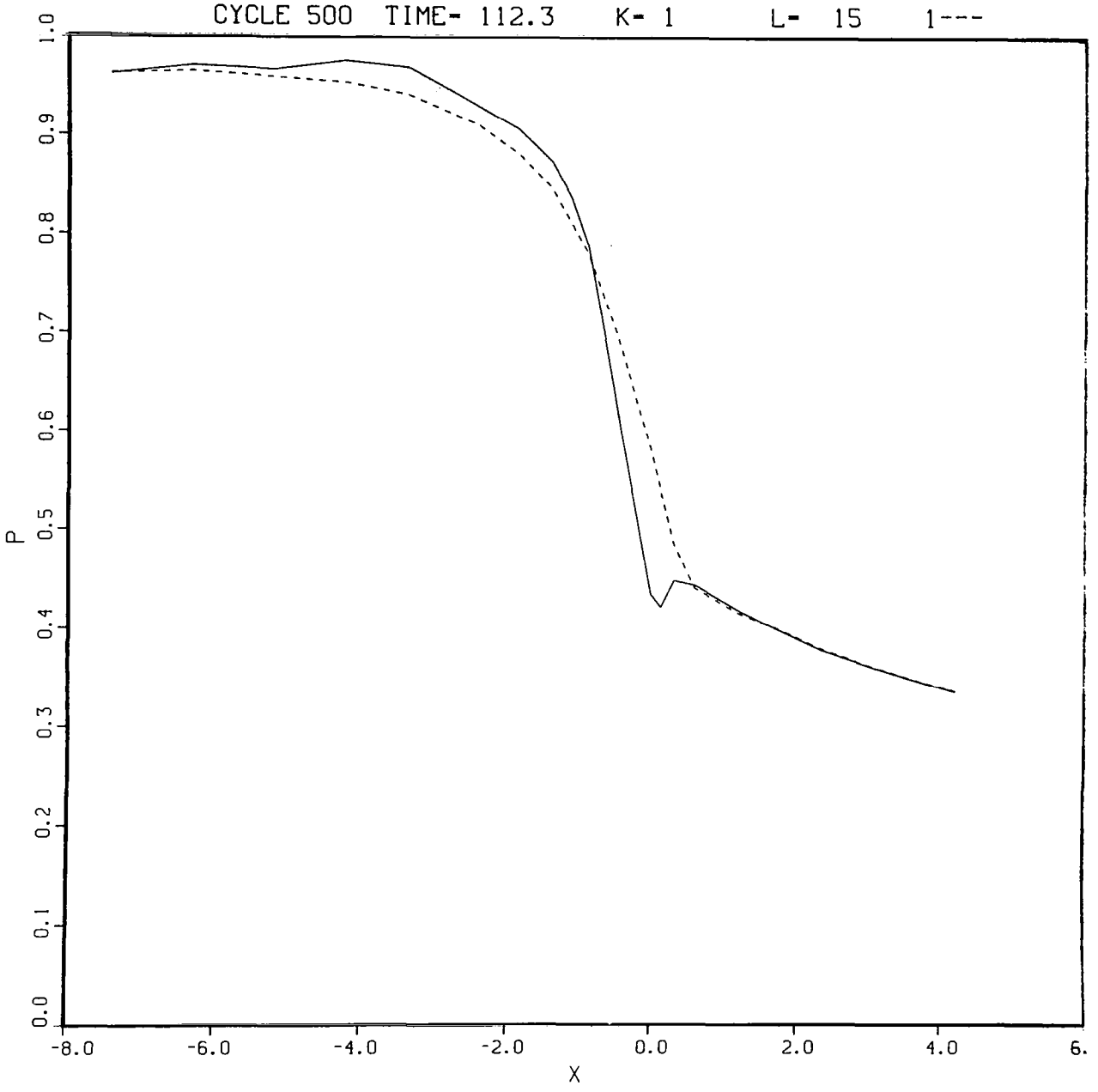

Figure 6-4 Computed Wall and Centerline Pressure Distributions for 2-D Laminar Flow. Solid Line: Wall. Dashed Line: Centerline.

although convergence was attained well before the end of the run. The computer time per step was about 13% greater than in the laminar flow calculation because of the extra computational labor involved in evaluating the turbulent viscosity.

The computed steady-state discharge coefficient is $C_W = 0.9961$, and the dimensionless thrust is 7.2922. The convergence history is displayed in Fig. 6-5 which shows the dimensionless net mass flux and thrust as a function of the time step index NC.

The computed wall pressure distribution displayed in Fig. 6-6 is in somewhat better agreement with the experimental data than the laminar flow results shown in Fig. 6-3. The computed wall and centerline pressure distribution are shown in Fig. 6-7. The vertical profiles of velocity and pressure across the nozzle throat are given in Fig. 6-8. Similar profiles across the nozzle exit plane (the outflow boundary) are given in Fig. 6-9. Figures 6-7 to 6-9 show that substantial flowfield gradients exist across the nozzle in the neighborhood of the throat. In the supersonic region downstream of the throat, however, the pressure becomes uniform across the nozzle. The velocity is also spatially uniform, except in the near-wall region occupied by the turbulent boundary layer.

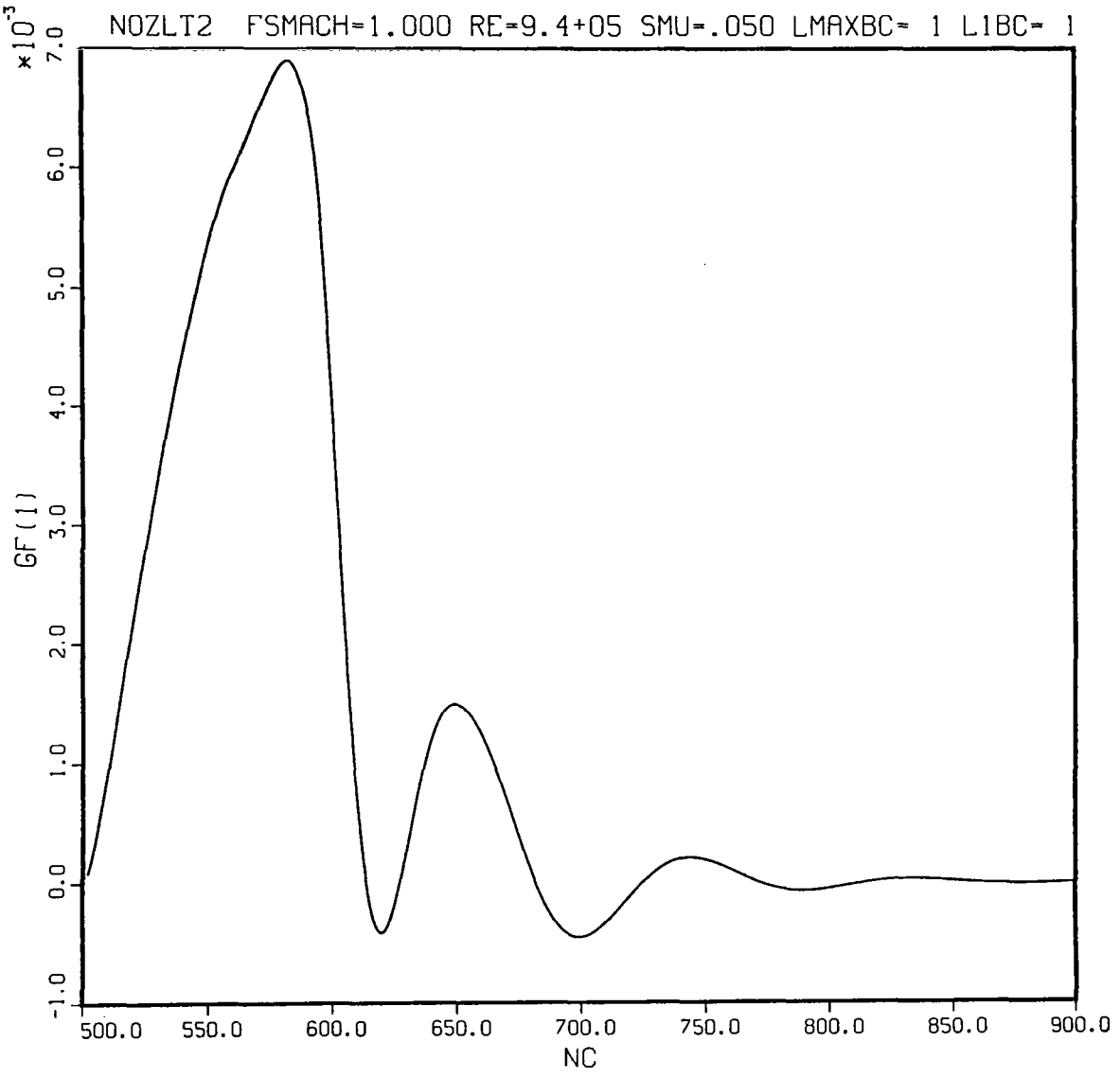

Figure 6-5a Convergence History for 2-D Turbulent Flow Computation Showing Net Mass Flow Rate Versus Time Step Index NC.

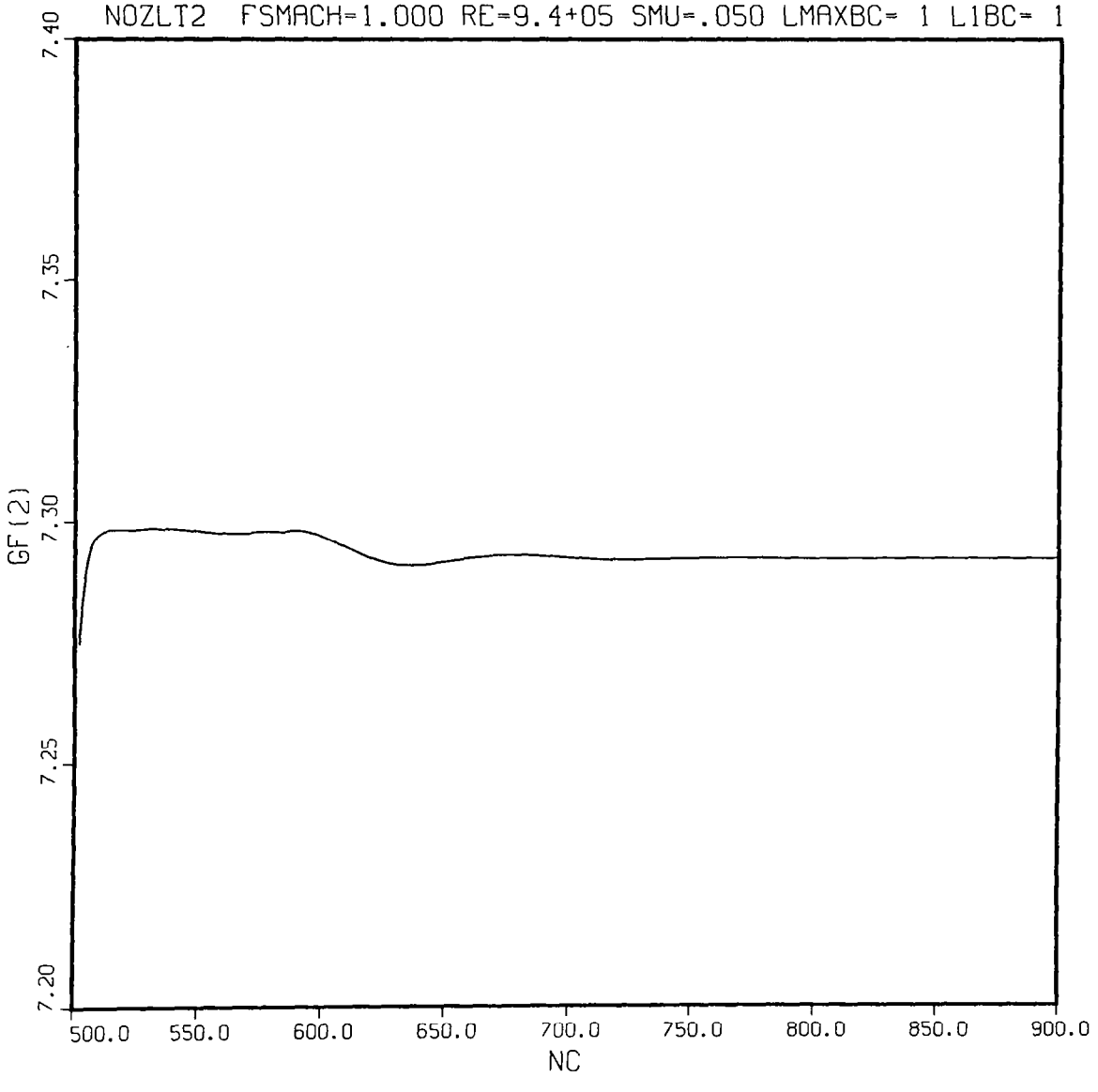

Figure 6-5b Convergence History of 2-D Turbulent Flow Computation Showing Net Thrust Versus Time Step Index NC.

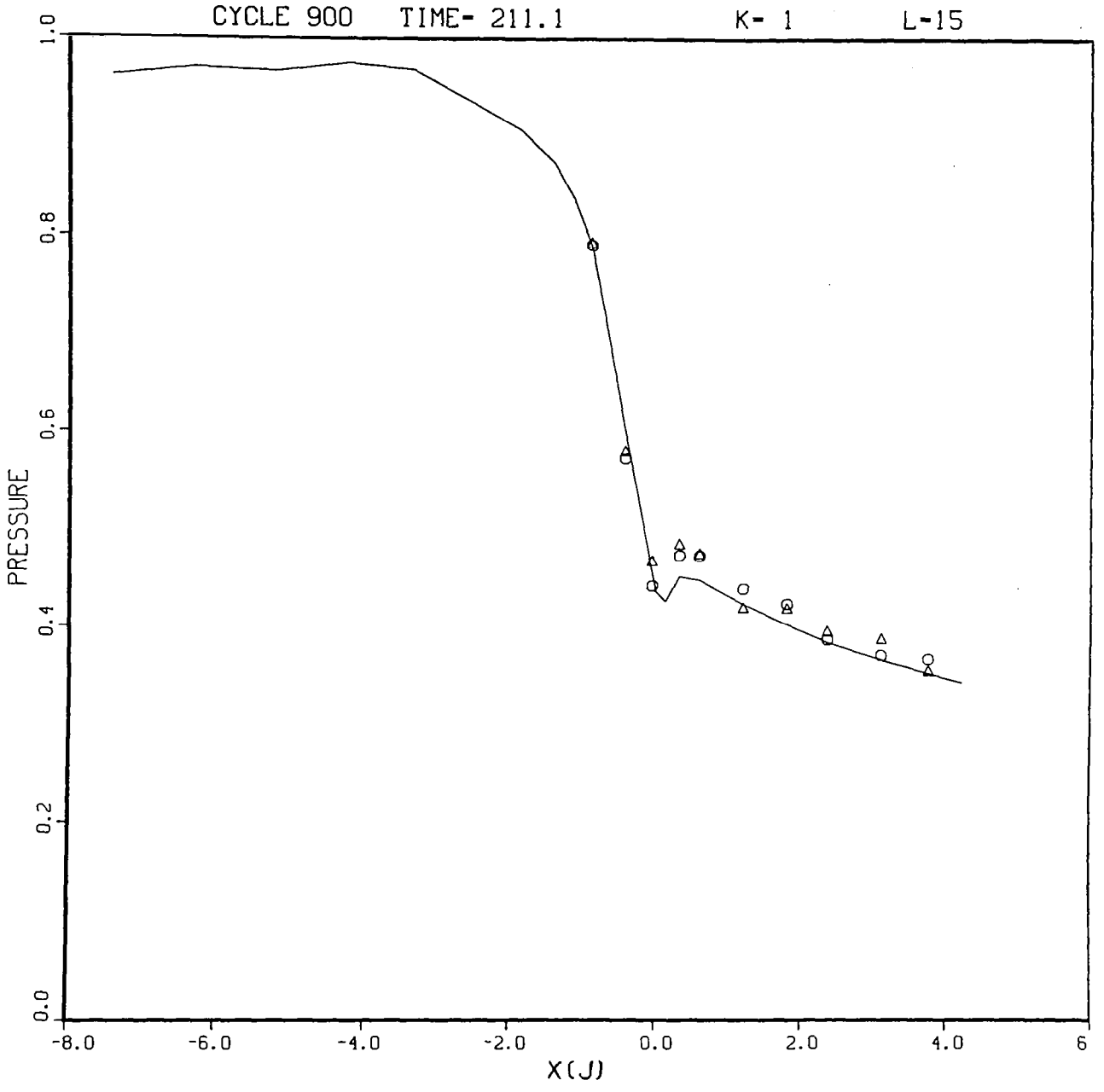

Figure 6-6 Comparison of 2-D Turbulent Flow Wall Pressure Distribution With Experimental Data of Ref. 10. Data Points: Circles, Upper Flap; Triangles, Lower Flap. Computation: Solid Line.

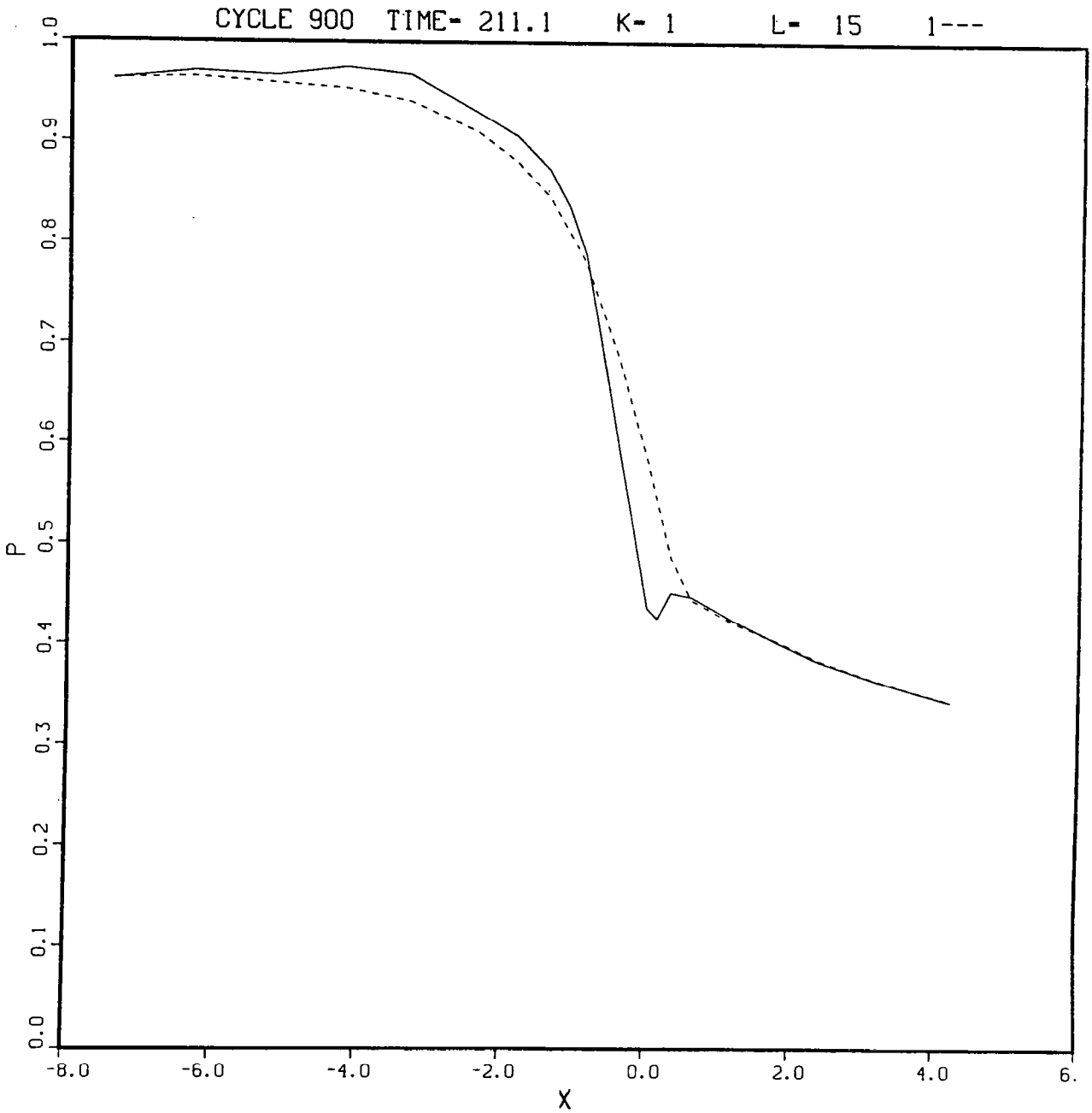

Figure 6-7 Computed Wall and Centerline Pressure Distributions for 2-D Turbulent Flow. Solid Line: Wall. Dashed Line: Centerline.

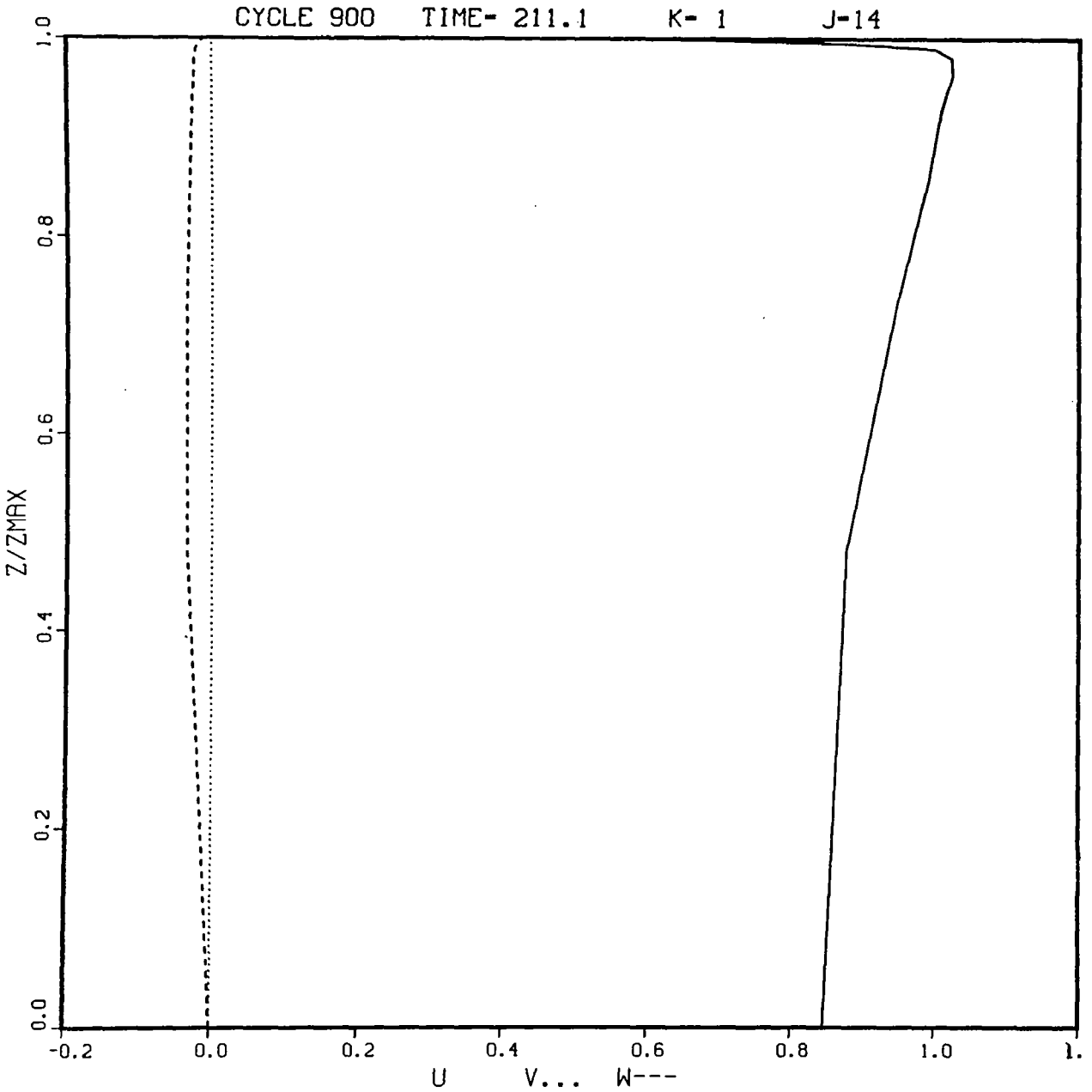

Figure 6-8a Velocity Profiles Across Throat for 2-D Turbulent Flow Computation

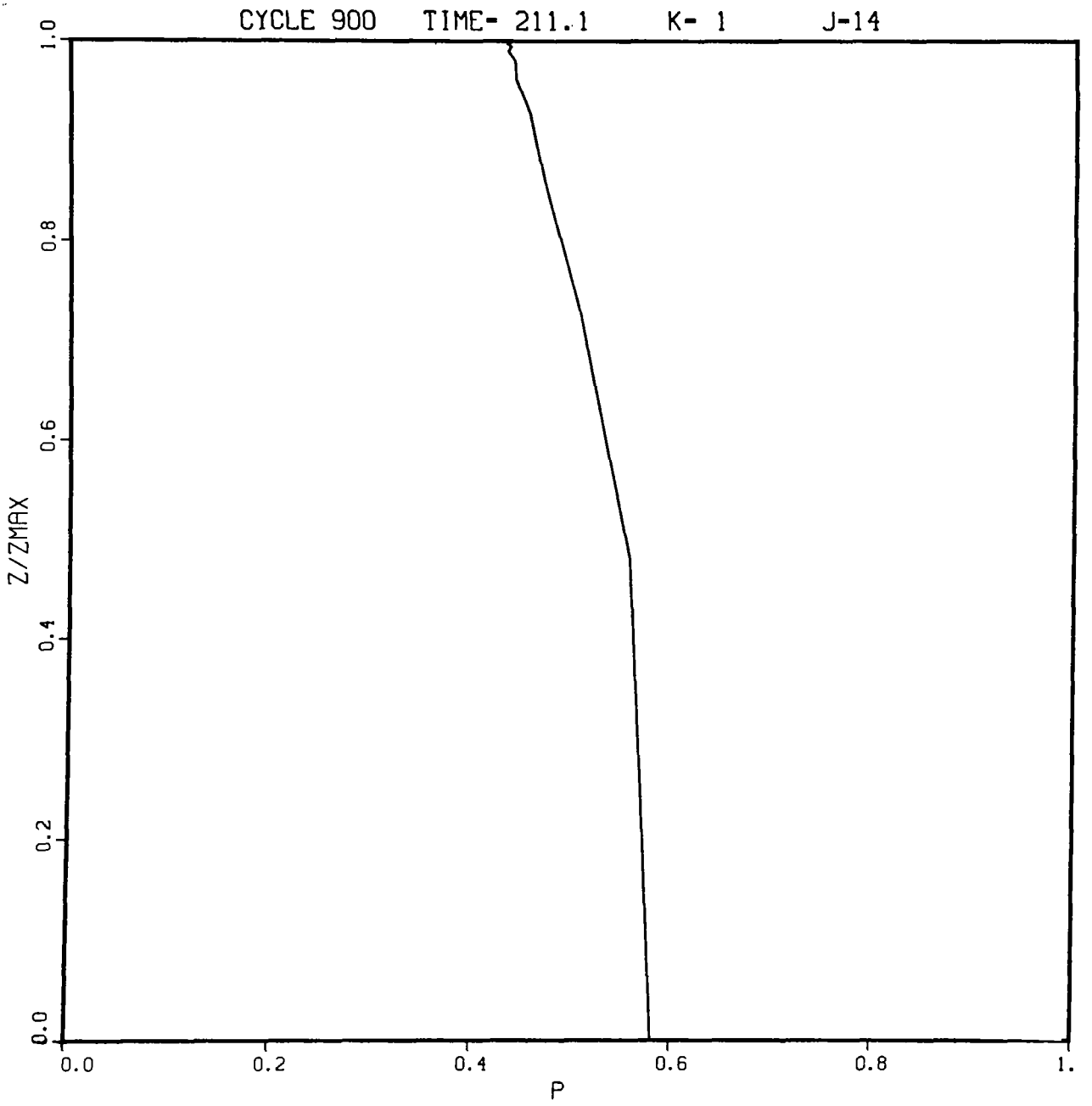

Figure 6-8b Pressure Profile Across Throat for 2-D Turbulent Flow Computation

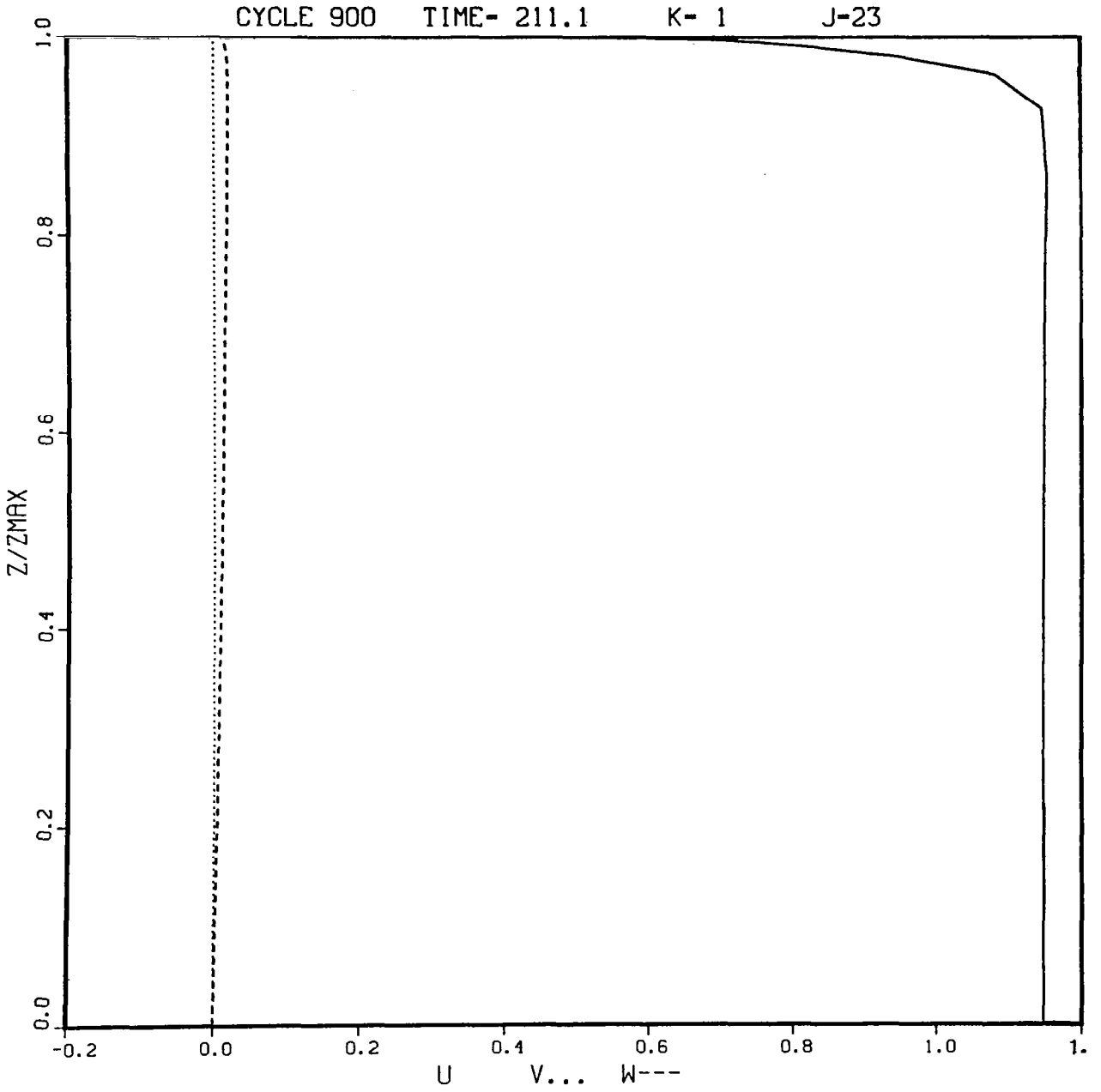

Figure 6-9a Velocity Profiles Across Exit Plane for 2-D Turbulent Flow Computation

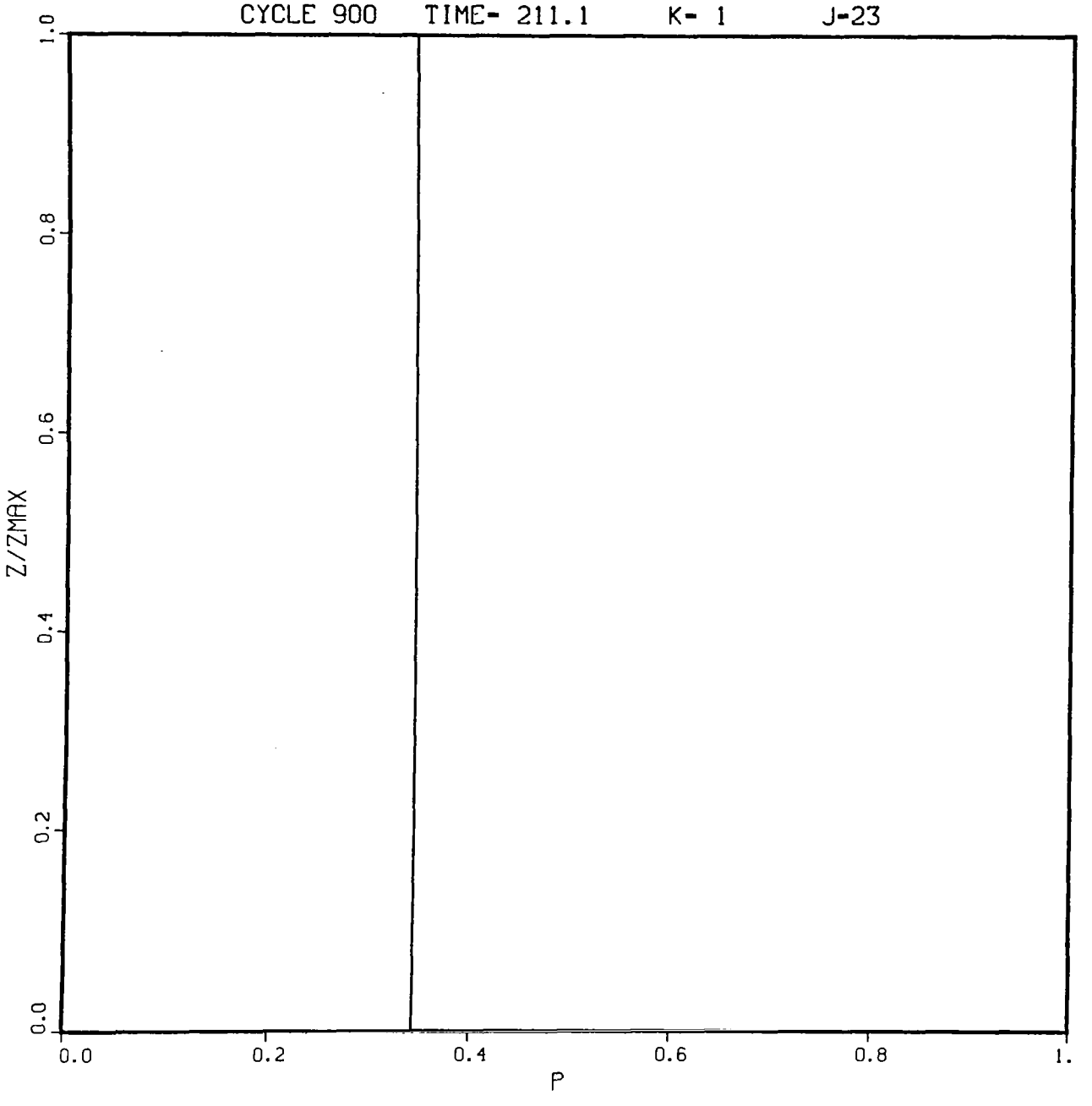

Figure 6-9b Pressure Profile Across Exit Plane for 2-D Turbulent Flow Computation

6.1.3 Three-Dimensional Flow Results

A three-dimensional laminar flow computation was performed on the grid shown in Fig. 6-2. The computation was run for 500 time steps, by which time the computed pressure field was essentially converged and was in agreement with the two-dimensional flow solution at the vertical plane of symmetry. The maximum Courant number (based on the minimum transverse mesh spacing) varied from 94 to 516 over the course of the run, which took approximately one hour of CDC 7600 computer time. The computed net thrust and discharge coefficient are 7.2197 and 0.9774, respectively. Both are somewhat lower than the two-dimensional flow predictions, which do not account for the sidewall.

Figure 6-10 shows a comparison of the computed wall pressures with experimental data. The pressure distribution along the upper nozzle wall at the vertical plane of symmetry is given in Fig. 6-10a. The corresponding pressure distribution along the sidewall at the horizontal plane of symmetry is displayed in Fig. 6-10b. As for the two-dimensional results, the computation tends to underpredict the data downstream of the throat, but agrees closely with the data in the subsonic and transonic regions upstream of the throat.

The computed flowfield is smooth, regular, and shows no evidence of boundary layer separation over most of the nozzle interior. However, the flowfield contains a strong secondary flow in the neighborhood of the axial corner where the upper wall and sidewall intersect. This secondary flow is localized in the throat region $-0.88 \lesssim x \lesssim 0.6$ (see Fig. 6-2a), and displays a flow reversal. Near the upstream and downstream ends of the described x interval, the velocity profiles near the axial corner display a slight flow reversal that is reminiscent of the reverse flow profile in a separated boundary layer. However, there is no flow reversal over the bulk of the upper wall or sidewall except in the immediate neighborhood of the corner. The peak reverse velocity exists at an axial station just upstream of the throat ($x = -0.186$), and is about 100% greater in magnitude than the general streamwise velocity $V_c \approx 0.8$ along the nozzle centerline at the same x station. The secondary flow thus is more properly characterized as a reverse jet rather than as a region of separated flow. The jet-like structure is readily apparent in Figs. 6-11a, b, which show the computed velocity profiles in the cross-sectional plane $x = -0.186$. Figs. 6-11a,b display the velocity profile along a vertical grid line Y = const. that passes approximately through the peak velocity point of the jet. Figs. 6-11c,d display a similar profile along a horizontal grid line Z = const. that passes approximately through the peak.

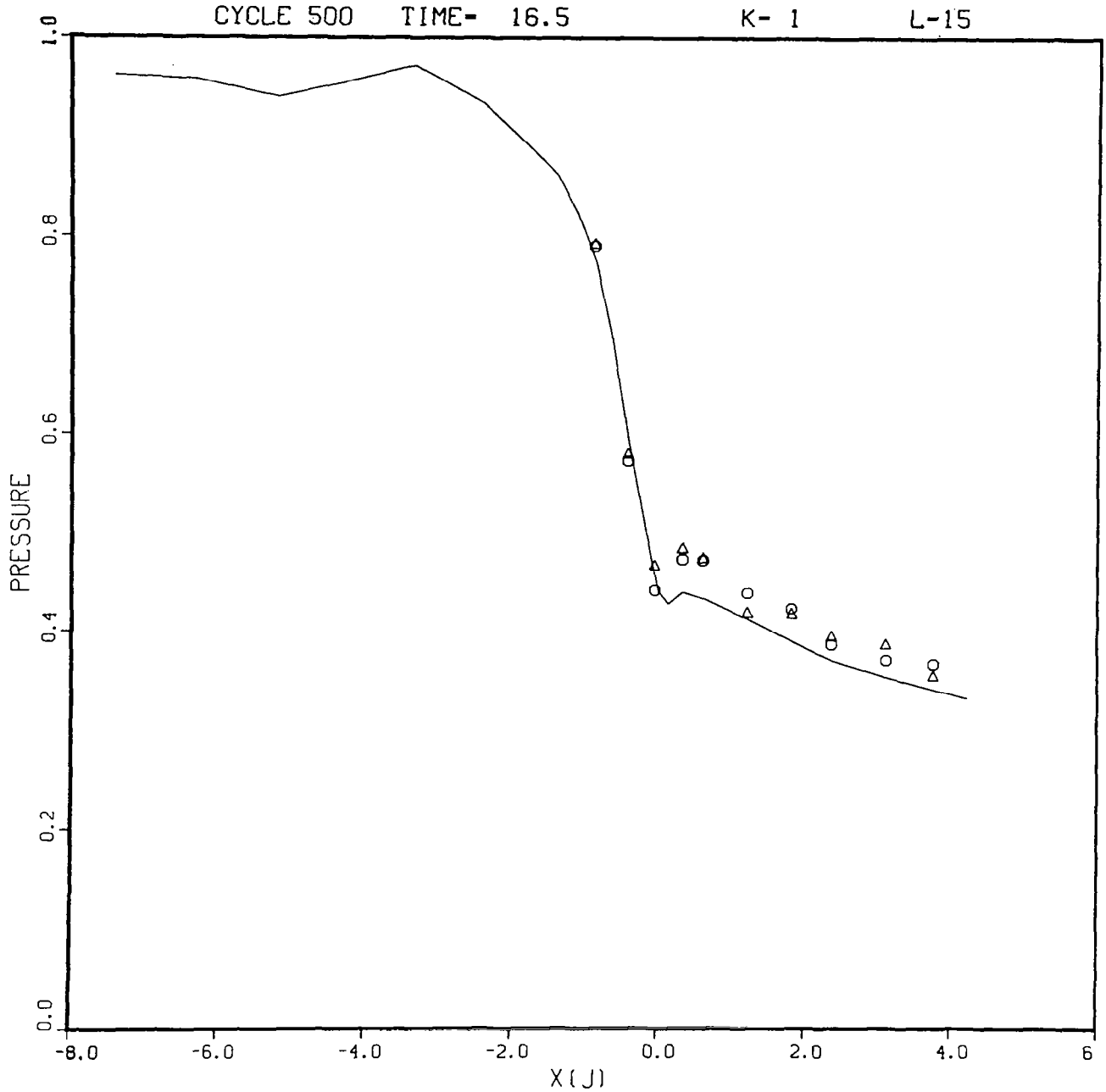

Figure 6-10a Computed Pressure Distribution Along Upper Nozzle Wall at Vertical Symmetry Plane Compared with Experimental Data

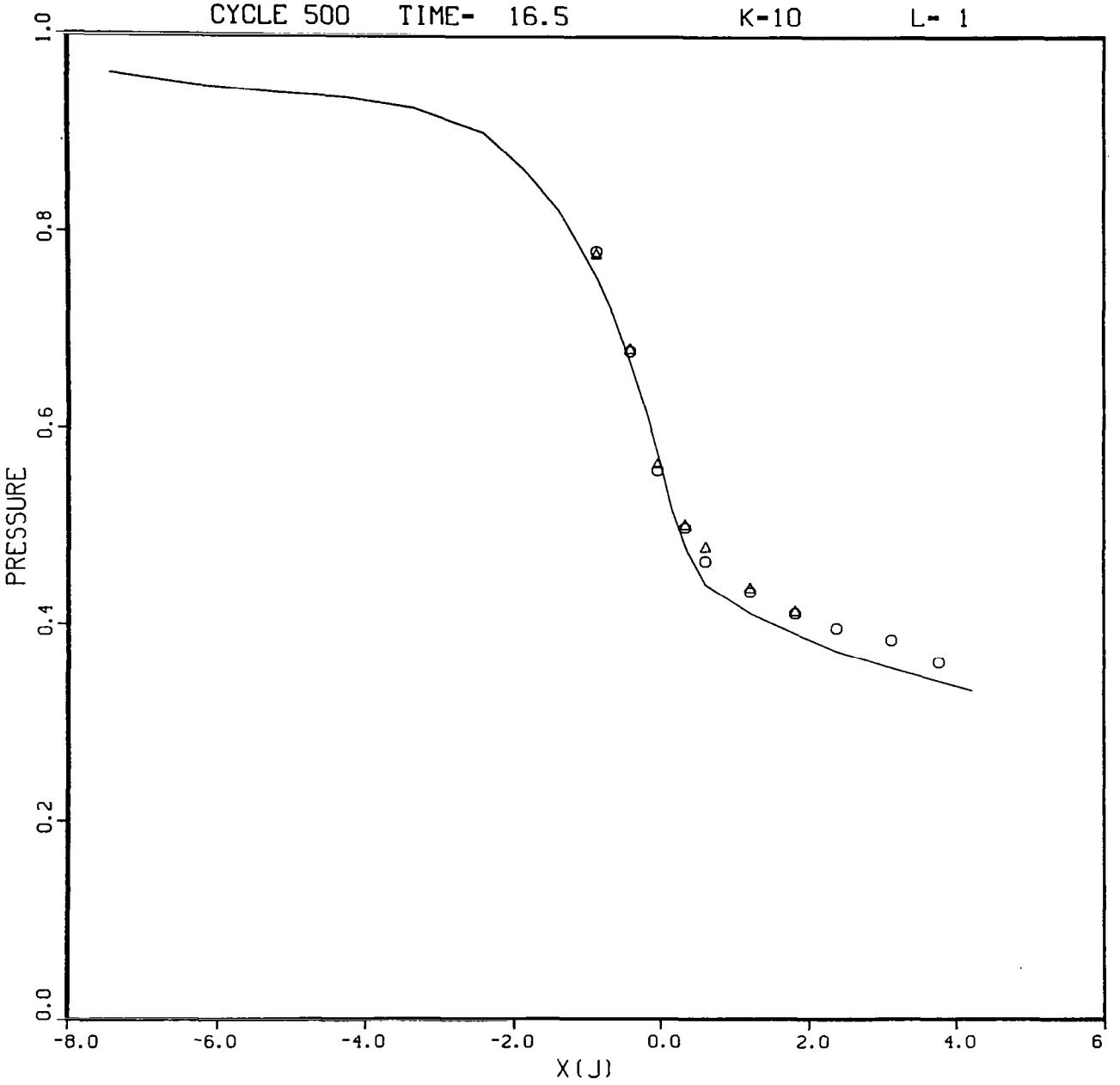

Figure 6-10b Computed Pressure Distribution Along Nozzle Sidewall at Horizontal Symmetry Plane Compared with Experimental Data

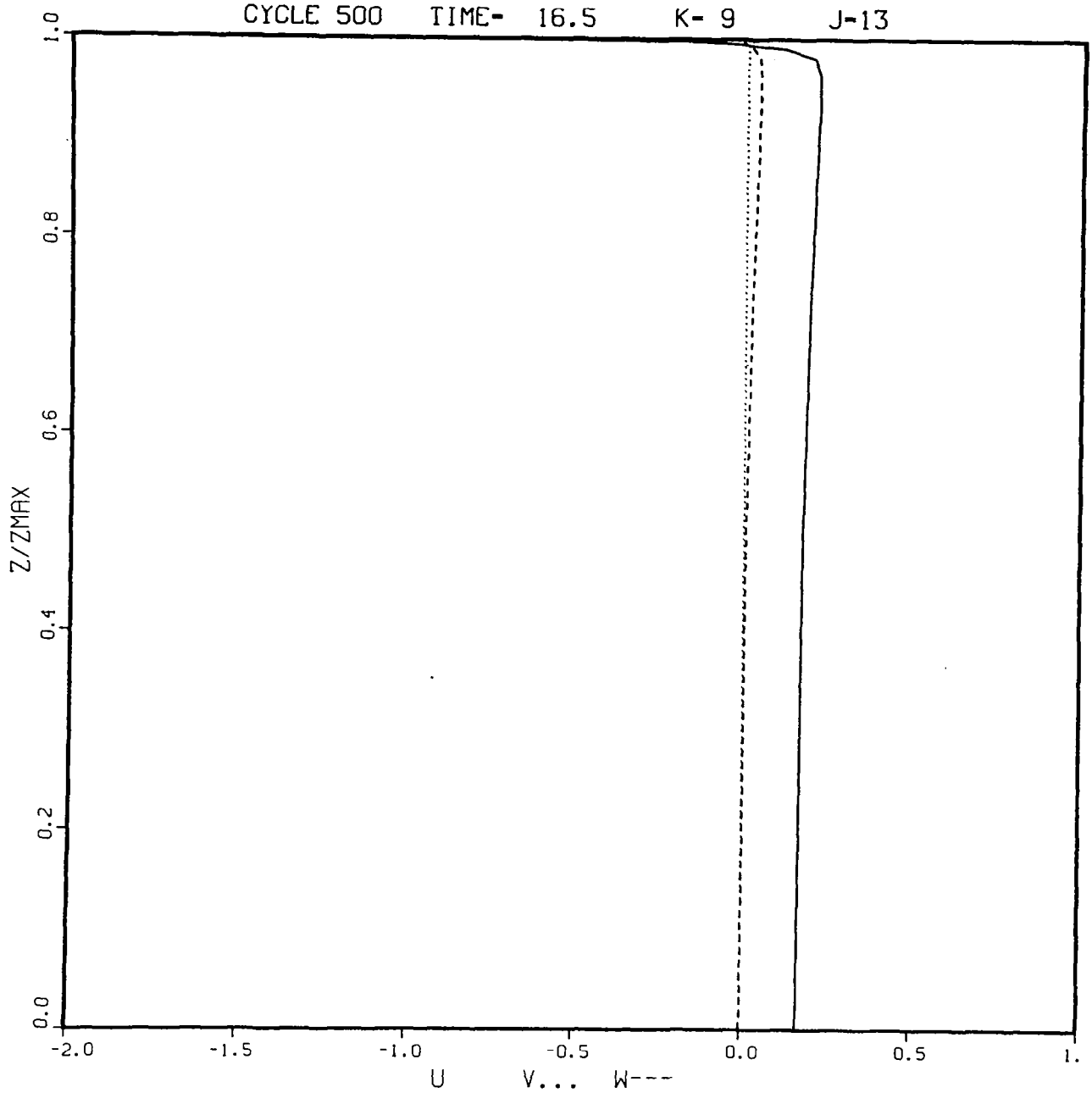

Figure 6-11a Velocity Profiles Along a Vertical Grid Line Passing Approximately Through Peak of Reverse Corner Jet

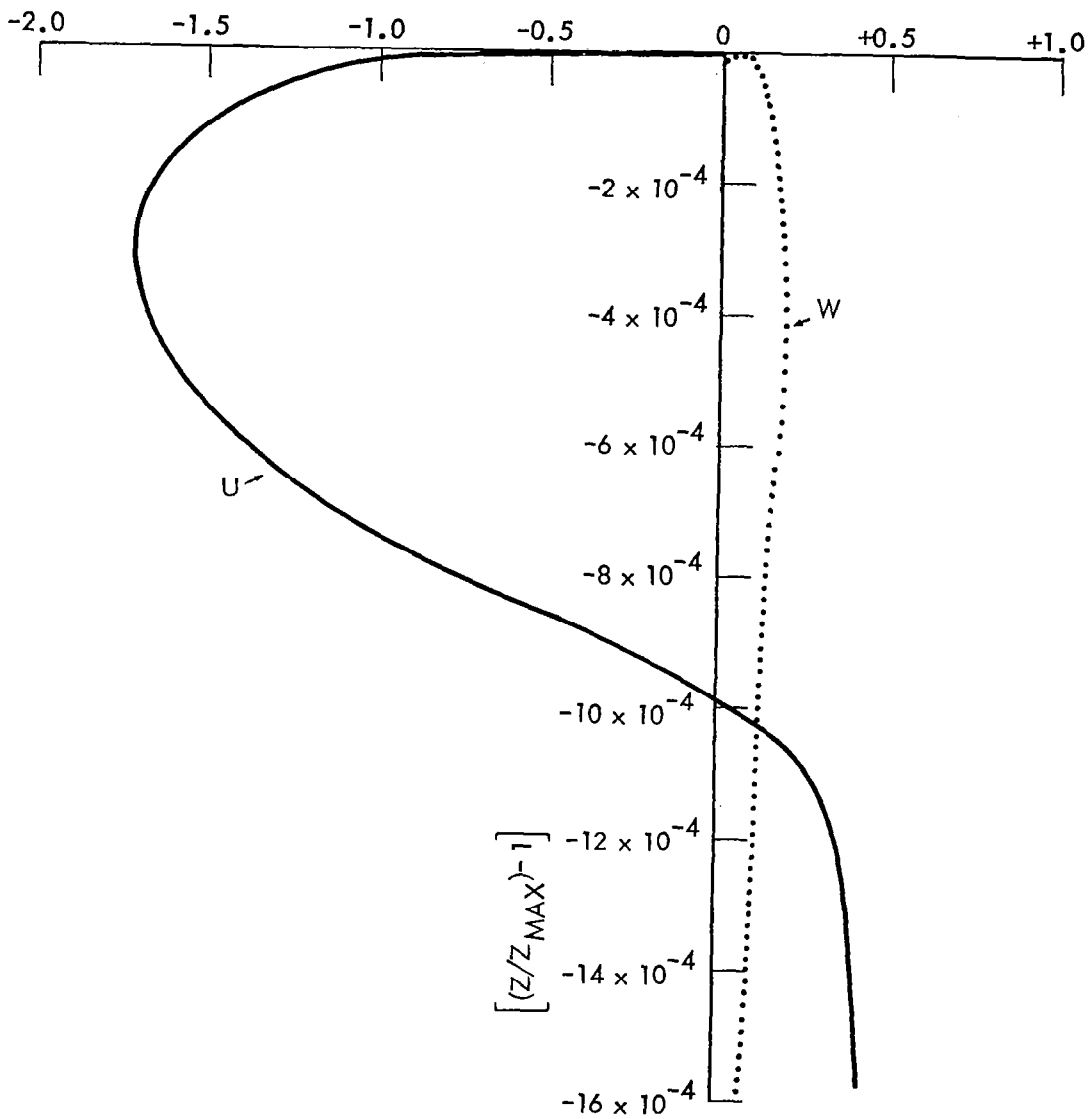

Figure 6-11b Magnified View of Near-Wall Portion of Velocity Profile Shown in Figure 6-11a

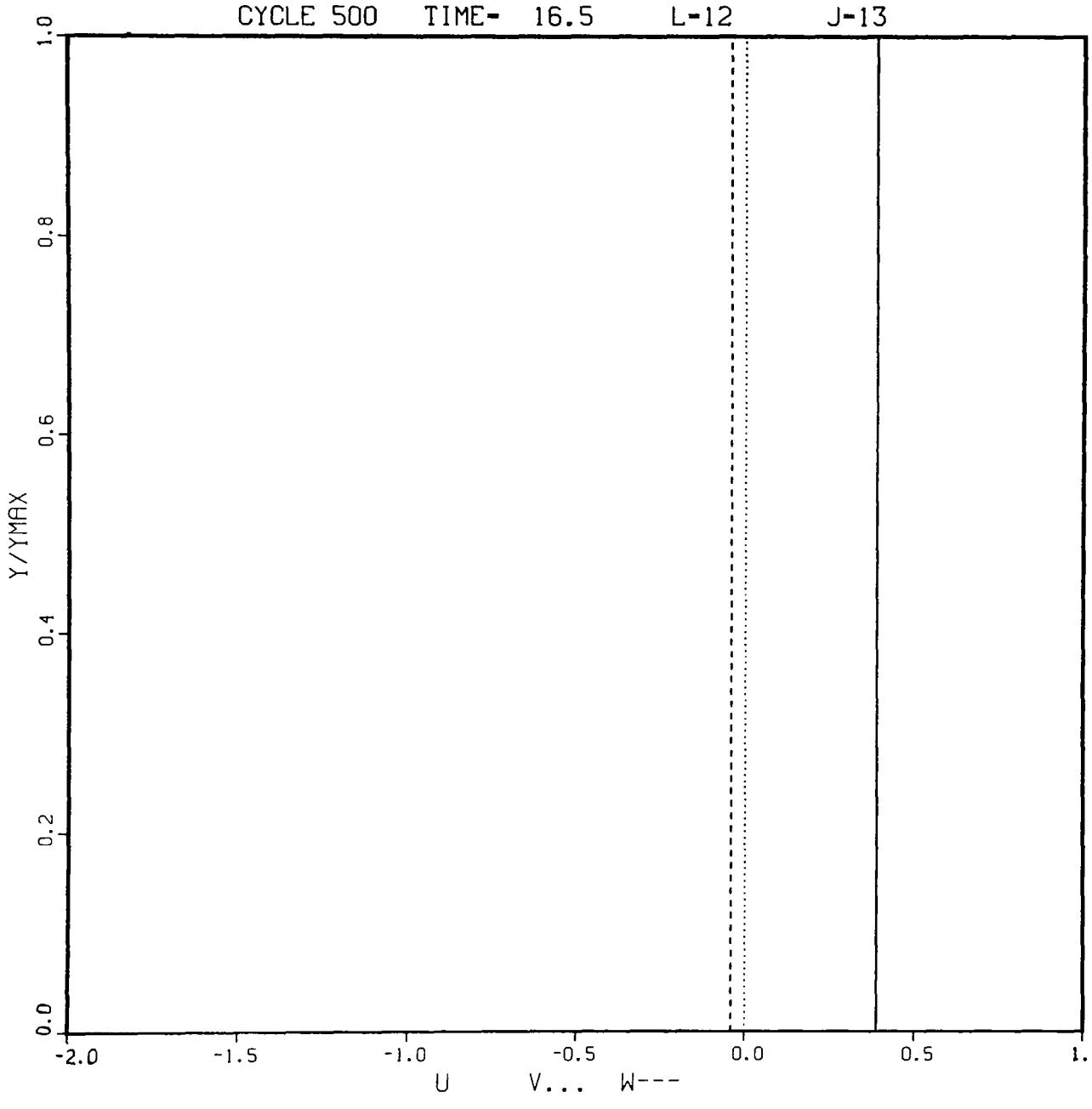

Figure 6-11c Velocity Profiles Along a Horizontal Grid Line Passing Approximately Through Peak of Reverse Corner Jet

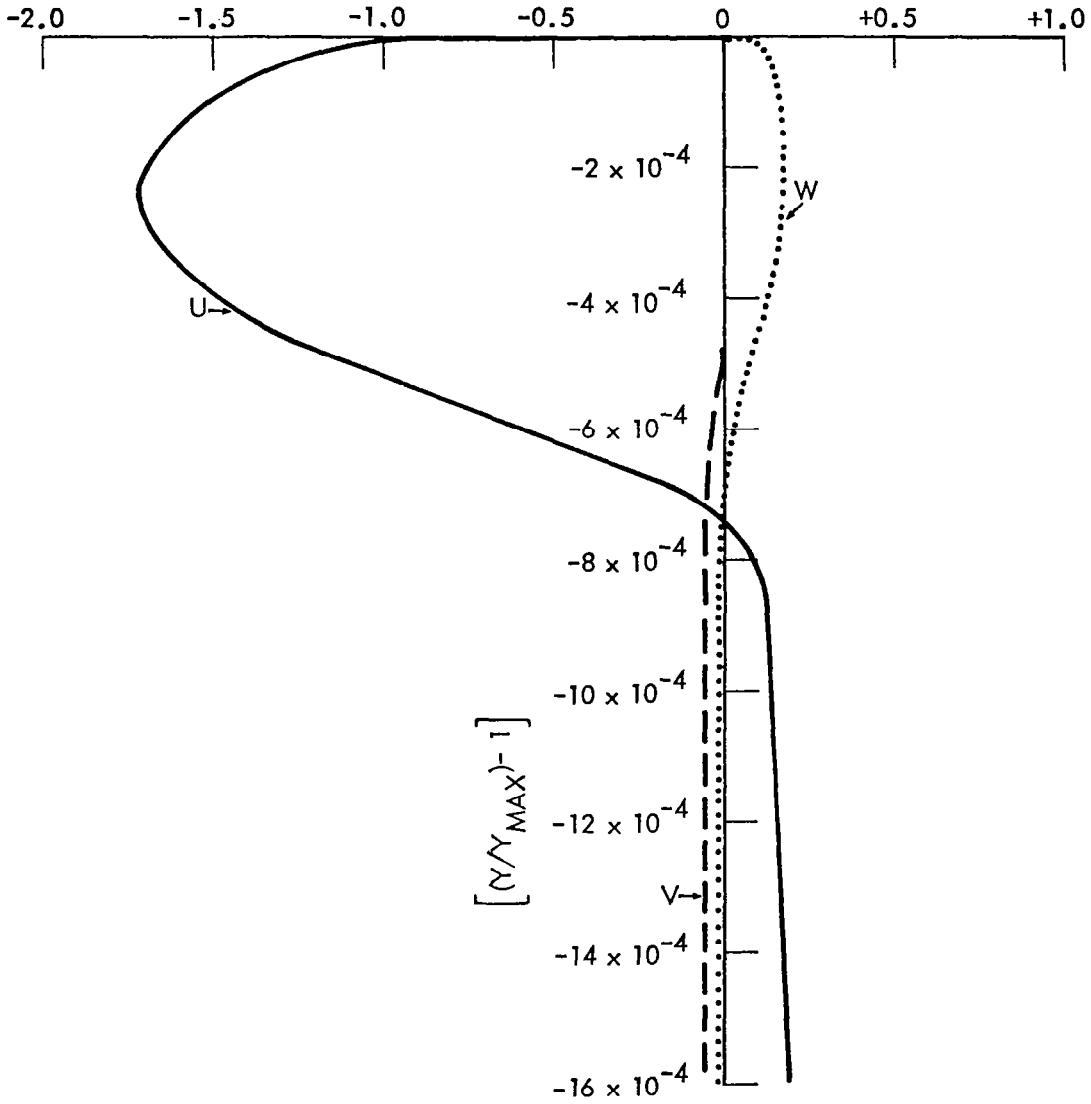

Figure 6-11d Magnified View of Near-Wall Portion of Velocity Profile Shown in Figure 6-11c

6.2 INTERNAL AND EXTERNAL FLOWFIELD OF A CIRCULAR NOZZLE

6.2.1 Configuration, Operating Conditions, and Computational Grid

The configuration of this axisymmetric nozzle is displayed in Fig. 6-12. The interior wall has an inlet section of constant radius, a convergent section, and an exit section of constant radius. The external wall consists of an initial section of constant radius, followed by a circular arc boattail. The internal and external surfaces do not meet at a sharp trailing edge at the exit. Rather, the trailing edge is squared off by a vertical cut. Because the numerical algorithm employs a Cartesian base coordinate system, axisymmetric flows must be treated as any other three-dimensional flow; that is by using a full three-dimensional grid. In the present case, the flow region about the nozzle is bounded by inflow and outflow planes normal to the symmetry axis, and by a cylindrical outer boundary (the freestream boundary) that is concentric with the nozzle and is located 5 cm away from the cylindrical initial section of the outer surface of the nozzle. The outflow boundary is placed about one exit diameter downstream of the nozzle exit so as to include the near-field exhaust jet and the wake of the nozzle wall in the computation. The first quadrant $y \geq 0$, $z \geq 0$ of the region between the inflow and outflow planes and within the outer cylindrical boundary is mapped onto a rectangular computational parallelepiped as shown in Fig. 6-13. The flow computation is carried out on a uniform 28x5x28 grid in this computational space. Note that the mapping is singular, inasmuch as the axis of symmetry maps onto the surface $\zeta=0$ in the computational space.

The image of this uniform grid in physical space consists of five meridional planes (including the symmetry planes y=0 and z=0) equally-spaced at intervals of 22.5 degrees; 28 cross-sectional planes along the x direction, of which the last five are downstream of the nozzle exit; 15 grid points distributed exponentially across the interior of the nozzle in the radial direction, and another 13 points distributed exponentially between the outer surface of the nozzle wall and the cylindrical outer boundary. Side and end views of the physical grid are displayed in Figs. 6-14a and 6-14b.

The wind tunnel test conditions are such that both the outer and internal flows are turbulent. The conditions are as follows (Ref. 11): Air is the medium for both the internal and external flows (γ = 1.4, Pr = 0.72). The internal flow stagnation pressure and temperature are 1.32 atm. and 300 Kelvin, respectively.

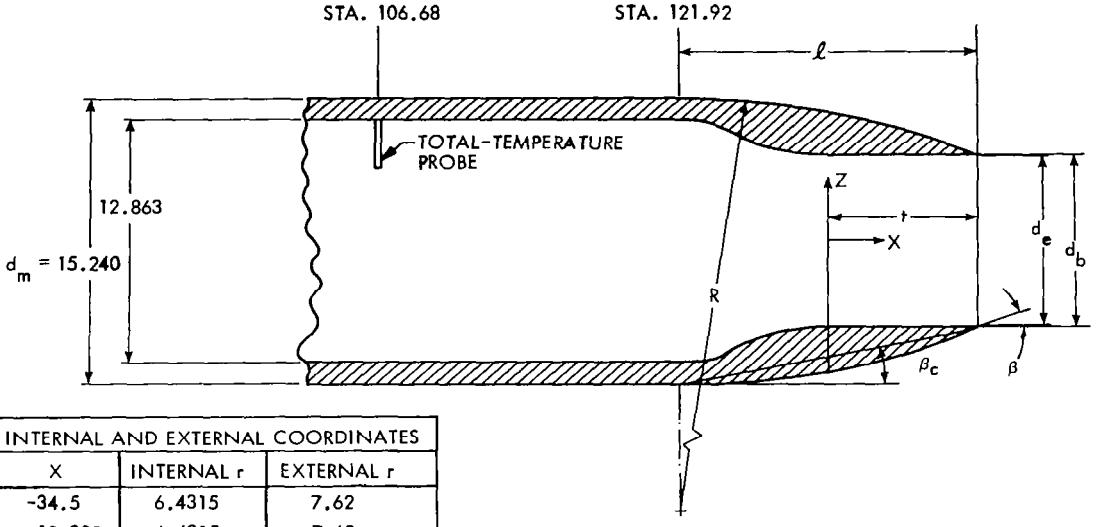

INTERNAL AND EXTERNAL COORDINATES		
X	INTERNAL r	EXTERNAL r
-34.5	6.4315	7.62
-19.322	6.4315	7.62
-15.5	6.336	CIRCULAR ARC
-12.5	6.194	
-10.1	5.996	
-8.4	5.820	
-7.0	5.653	
-5.842	5.436	
-4.953	5.019	
-4.064	4.585	
-3.048	4.229	
-2.032	3.993	
-1.016	3.856	
0	3.810	
7.62	3.810	3.886

(ALL DIMENSIONS IN CENTIMETERS)

GEOMETRIC PARAMETERS						
ℓ/d_m	d_e/d_m	d_b/d_m	R/d_m	t/d_m	β_1 deg	β_c, deg
1.768	0.50	0.51	6.50	0.50	15.773	7.886

EXTERNAL CIRCULAR ARC

$$r = r_o - R\,(1 - \cos\theta), \quad x_m \le x \le 7.62$$

$$\theta = \sin^{-1}\,(x - x_m)/R$$

$$R = 99.06, \quad r_o = 7.62, \quad x_m = -19.322$$

Figure 6-12 Configuration and Coordinates for Circular Nozzle

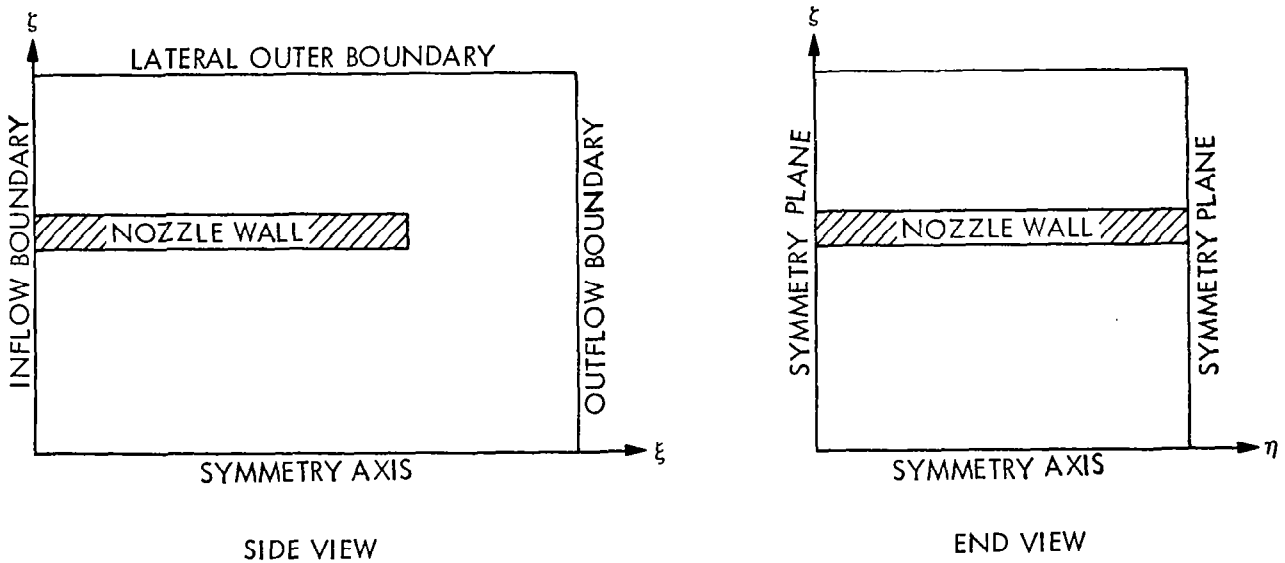

Figure 6-13 Illustration of Computational Space for Circular Nozzle

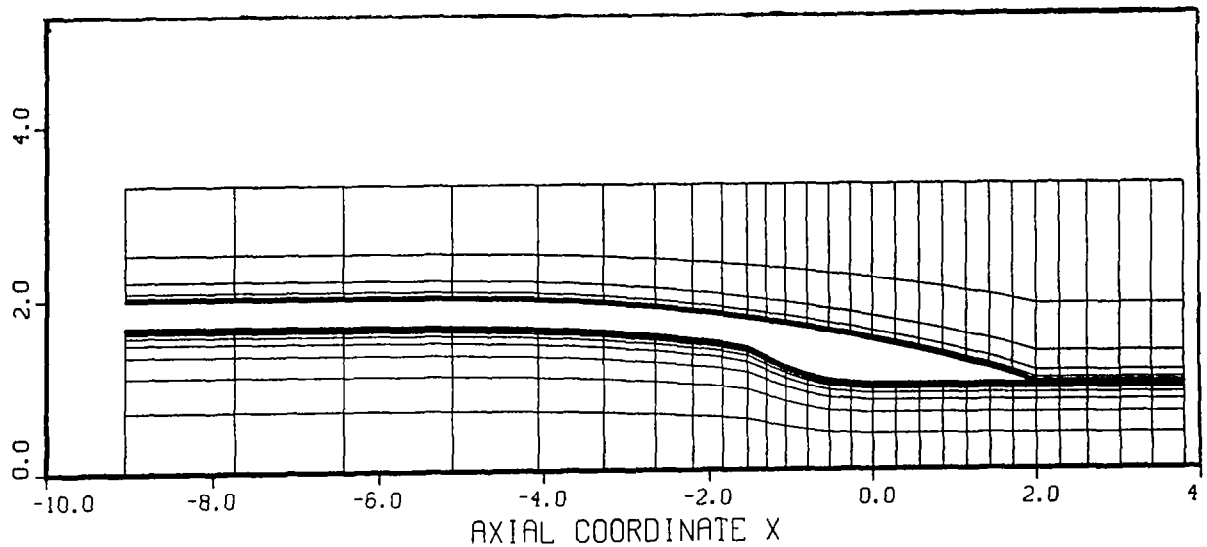

Figure 6-14a Side View of Computational Grid for Circular Nozzle

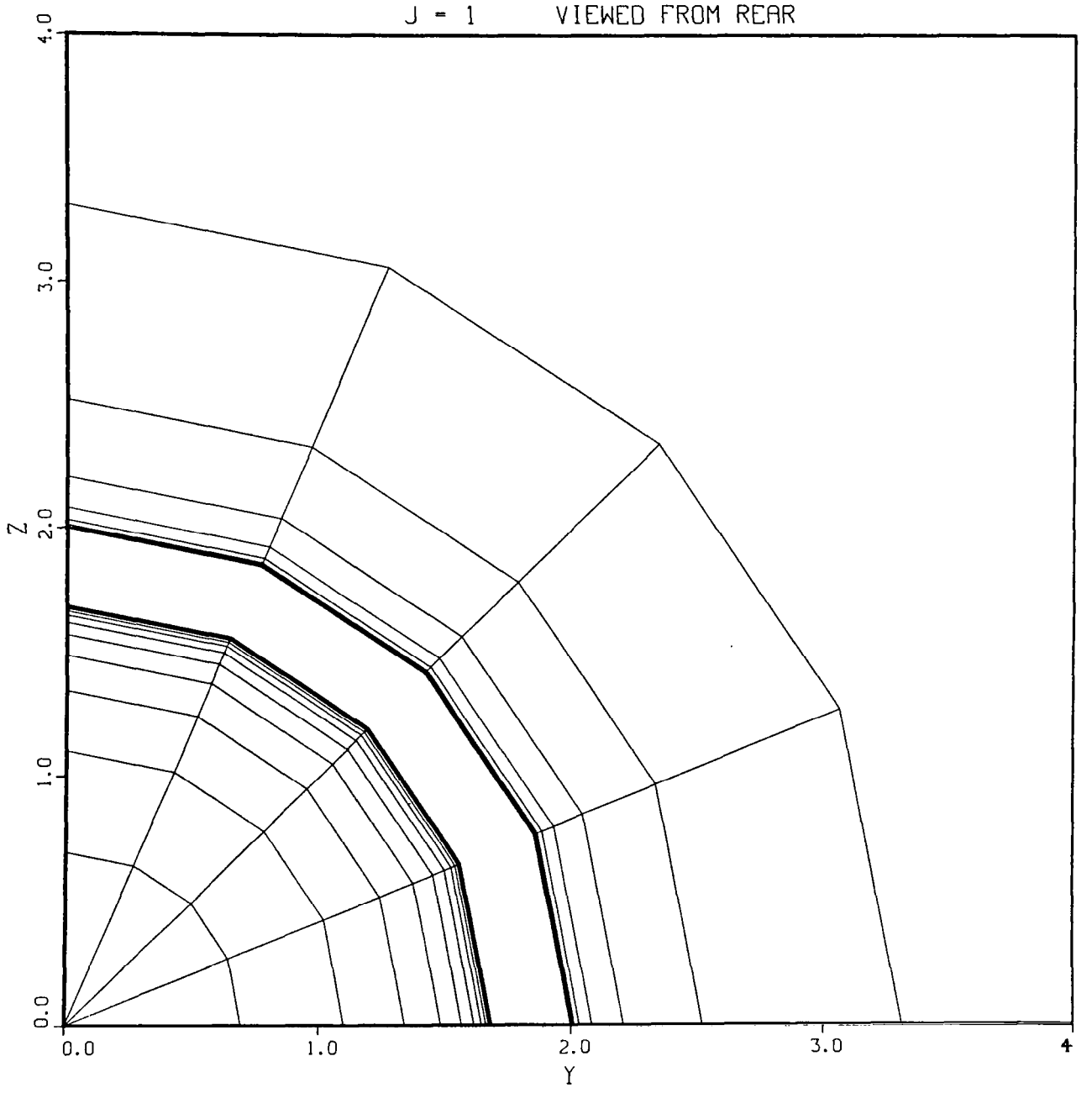

Figure 6-14b End View of Computational Grid for Circular Nozzle

The external flow has a freestream Mach number $M_\infty = 0.8$, a stagnation temperature of 275 Kelvin, and the freestream static pressure is half the internal flow stagnation pressure. The Reynolds number based on internal flow stagnation chamber conditions and on the nozzle exit radius is 1.1×10^6, using the Sutherland viscosity law.

The boundary conditions for the computation are as follows: Adiabatic wall boundary conditions are employed. The transverse velocity components are assumed to be small over the entire inflow boundary ($v = w = 0$), and the total temperature over the external flow portion of the inflow boundary is taken as uniform and equal to the freestream stagnation temperature. Static pressure surveys taken during the test showed no significant departure from the freestream pressure over the external flow part of the inflow plane (Ref. 12). This information, together with the measured external boundary layer velocity distribution has been used to calculate the remaining flow variables, which are held fixed over the external flow portion of the inflow plane during the flowfield computation.

On the portion of the inflow plane interior to the nozzle, probe surveys lacked the resolution to give information any more detailed than an estimate on the boundary layer thickness on the interior wall surface (Ref. 12). Consequently, the total temperature has been assumed uniform and equal to the measured stagnation temperature. A one-seventh power boundary layer velocity profile has been used together with the static pressure and core velocity predicted by one-dimensional isentropic flow theory to estimate the total pressure distribution across the part of the inflow plane interior to the nozzle. The described total pressure and total temperature are used as boundary conditions for the implicit flowfield computation (see Section 2.3.1).

The initial conditions for the region between the inflow plane and the nozzle exit plane are obtained as follows. Flow conditions in the interior of the nozzle are estimated in the same fashion as described in Section 5.1 for the cosine-shaped nozzle. Outside the nozzle, the transverse velocity components are set to zero ($v = w = 0$), and both the static pressure and the total temperature are assumed uniform and equal to their freestream values. Along each streamwise mesh line η = const., ζ = const., the total pressure is assumed constant and equal to its value at the inflow plane. The velocity u and static temperature T then are computed from the known total pressure, total temperature, and static pressure, and density follows from the equation of state. The initial conditions at grid points in the cross sectional planes downstream of the nozzle exit plane simply are set equal to the conditions at the corresponding

points in the exit plane itself.

Numerical results for turbulent flow are presented below in dimensionless form. The non-dimensionalization is as described at the end of subsection 6.1.1.

6.2.2 Numerical Results

The three-dimensional turbulent flow computation attained convergence in 500 time steps at maximum Courant numbers (based on the minimum transverse grid spacing) that ranged from 1400 to 6800. The computation took slightly less than one hour of CDC 7600 computer time, and yielded a final steady state value of 3.428 for the net thrust.

Figure 6-15 displays the computed static pressure distribution along the interior surface of the nozzle wall and along the continuation of the wall grid line into the downstream mixing region. A similar distribution of pressure along the exterior surface of the nozzle wall is given in Fig. 6-16. Pressure coefficients derived from the latter data are shown in Fig. 6-17, along with wind tunnel experimental data from pressure taps located along the boattail (Ref. 11). The qualitative character of the theoretical curve matches that of the data, but the two are in close quantitative agreement only near the aft end of the boattail. The theoretical prediction of the crossover point from negative to positive values of Cp lies somewhat downstream of the experimental crossover point, and the minimum value of Cp that occurs near the forward end of the boattail is lower in the experimental data. A similar quantitative discrepancy with data on the forward part of the boattail was found in an axisymmetric flow solution by investigators at the Langley Research Center (according to Lawrence Putnam). In that solution, the jet mixing region was modeled as a cylindrical sting, and only the external flow was computed. Numerical experimentation showed that the theoretical prediction could be brought into agreement with the data by moving the upper computational boundary (freestream boundary) farther away from the nozzle outer surface. In the present computation, that boundary is only about 1.3 nozzle exit radii above the forward end of the boattail, whereas the corresponding distance is 2.3 exit radii at the aft end of the boattail where the theory and experiment agree closely. This suggests that the disagreement in the forward region could be eliminated by shifting the freestream boundary outward a distance of about one exit radius.

The computed flowfield shows that the external boundary layer remains attached over the most of the boattail, although there is a small region of separated flow near the aft end; specifically, there is a slight flow reversal in the velocity profiles at the last two streamwise grid points on the boattail, as shown in Fig. 6-18. It should be noted that an earlier laminar flow computation for the same geometry and operating conditions displayed massive separation over most of the boattail.

In addition to the boattail pressure taps, the wind tunnel test data included total pressure probe surveys across several axial stations in the downstream jet mixing region (Ref. 13). Figure 6-19 shows a comparison of these data with the computed total pressure distributions along the radial grid lines that lie nearest the probe survey stations, normalized by the computed values at the outermost interior grid point. One can see that at each station the computed shear layer in the near wake of the nozzle wall is somewhat thinner than that measured experimentally. This suggests that the wake turbulence model described in Section 4 may tend to under-predict the magnitude of the turbulent eddy viscosity in such regions.

One can also see from Fig. 6-19 that the computation apparently over-predicts the total pressure in the inner core of the jet. This is a result of the coarse grid employed in the region near the symmetry axis. It is anticipated that the agreement between predicted and experimental results would be improved substantially with the same number of grid points by using a less highly stretched radial grid (the grid spacing at the symmetry axis is a factor of 5000 greater at the axis than at the interior nozzle wall in the present computation), and by shifting the freestream computational boundary outward by a distance of one nozzle exit radius.

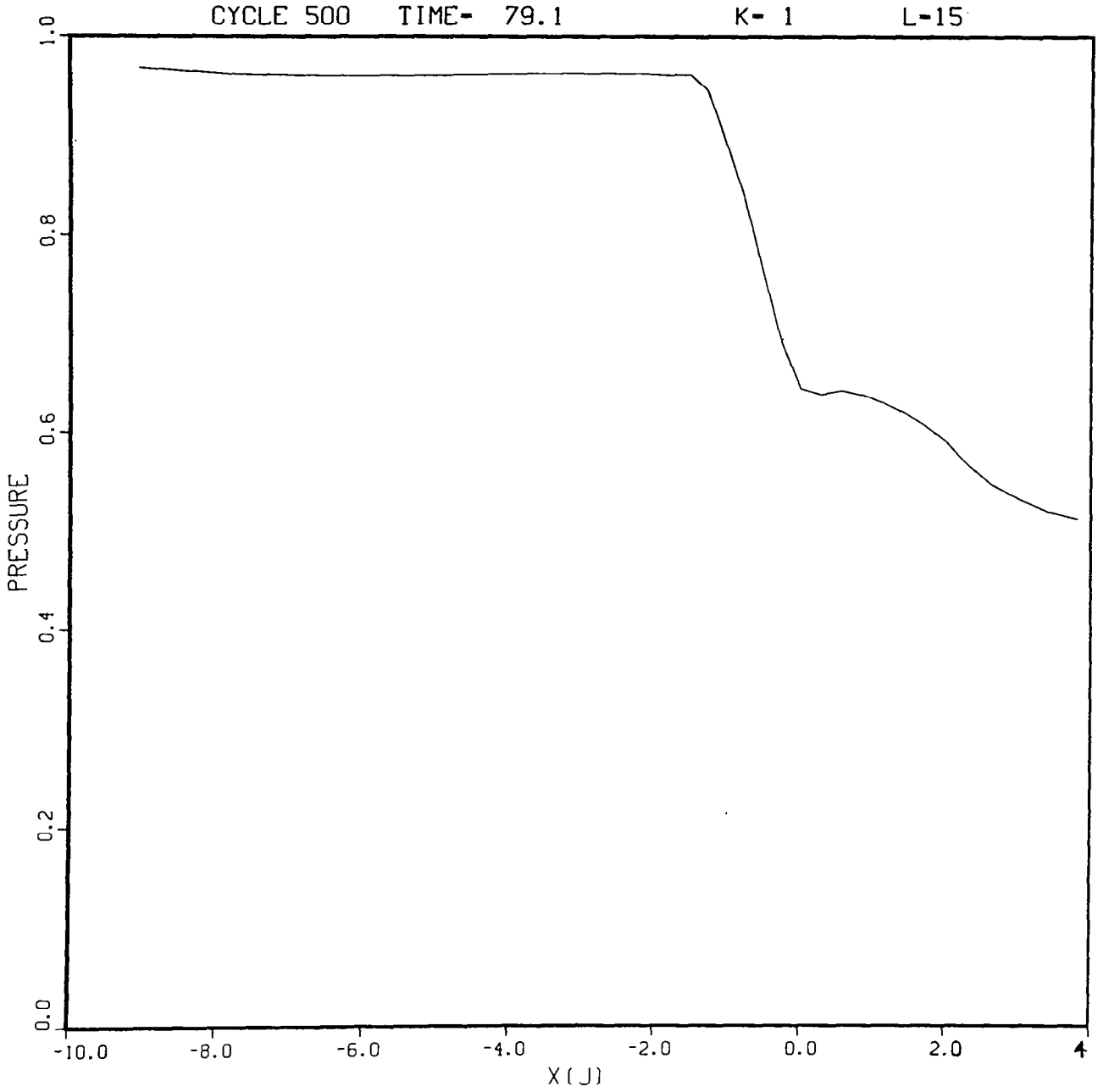

Figure 6-15 Computed Pressure Distribution Along Interior of Nozzle Wall and Along Continuation of Wall Grid Line into Downstream Jet Mixing Region

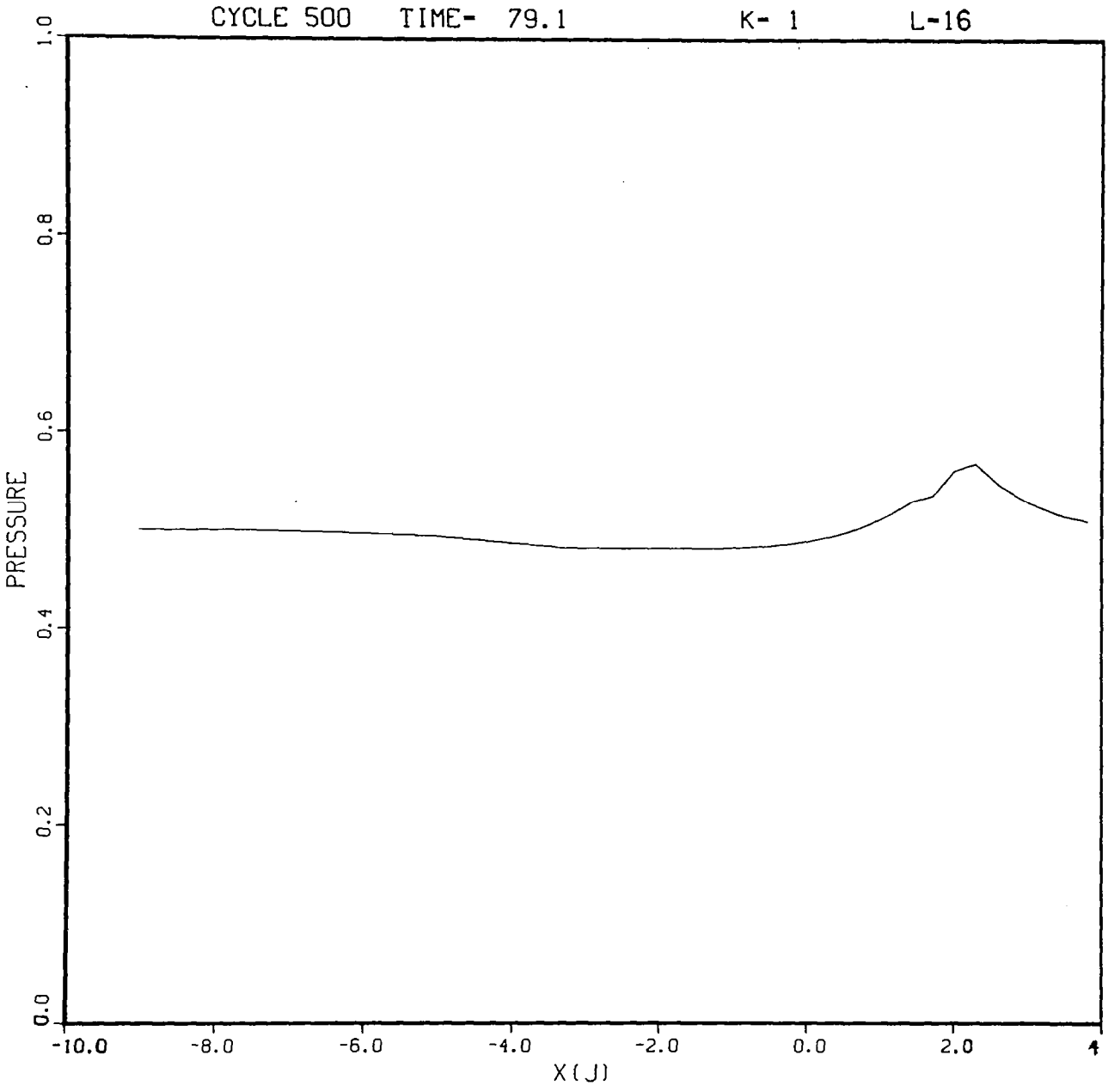

Figure 6-16 Pressure Distribution Along Exterior of Nozzle Wall and Along Continuation of Wall Grid Line into Downstream Jet Mixing Region

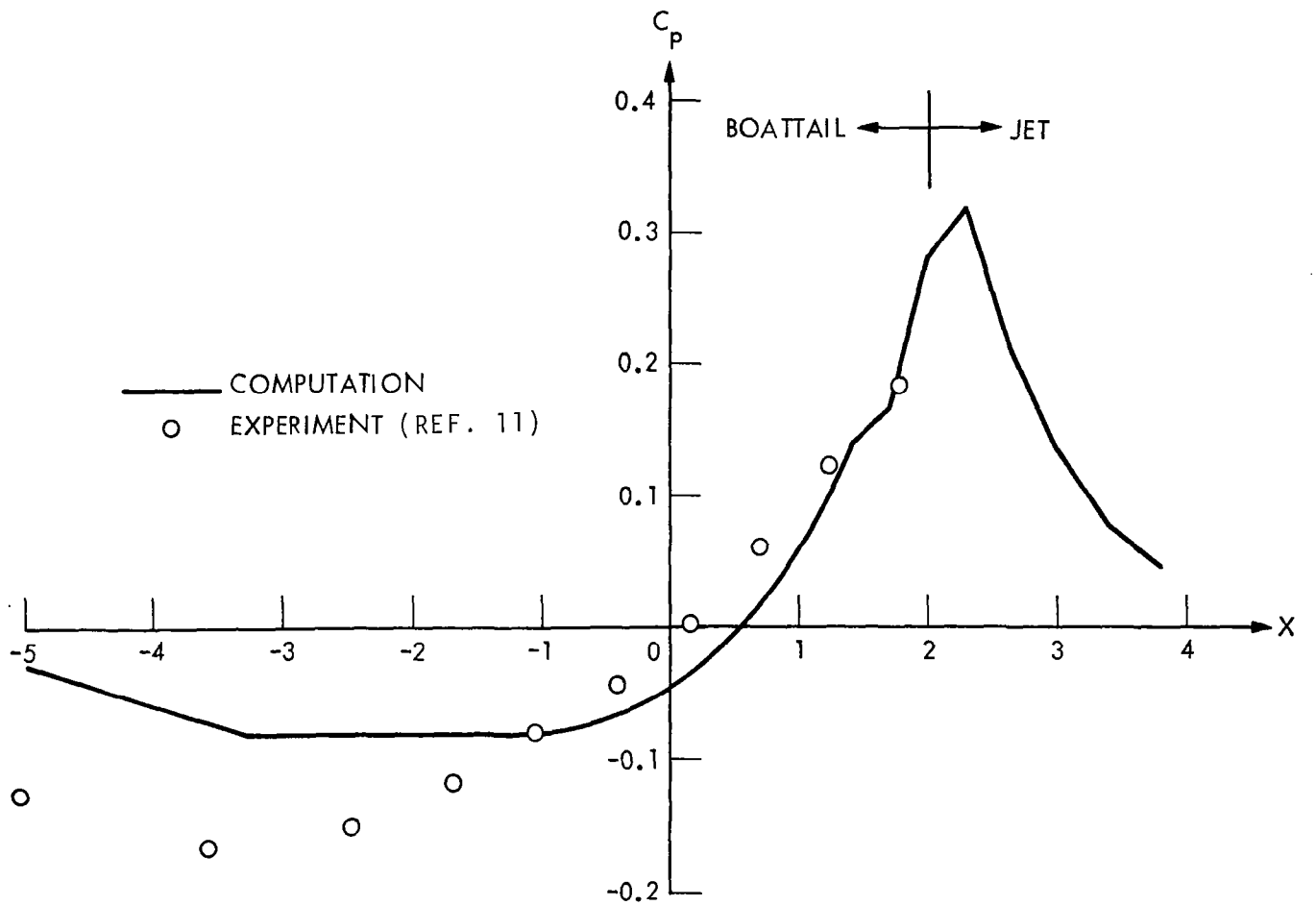

Figure 6-17 Pressure Coefficients Derived From Pressure Distribution of Figure 6-16 Compared with Wind Tunnel Data

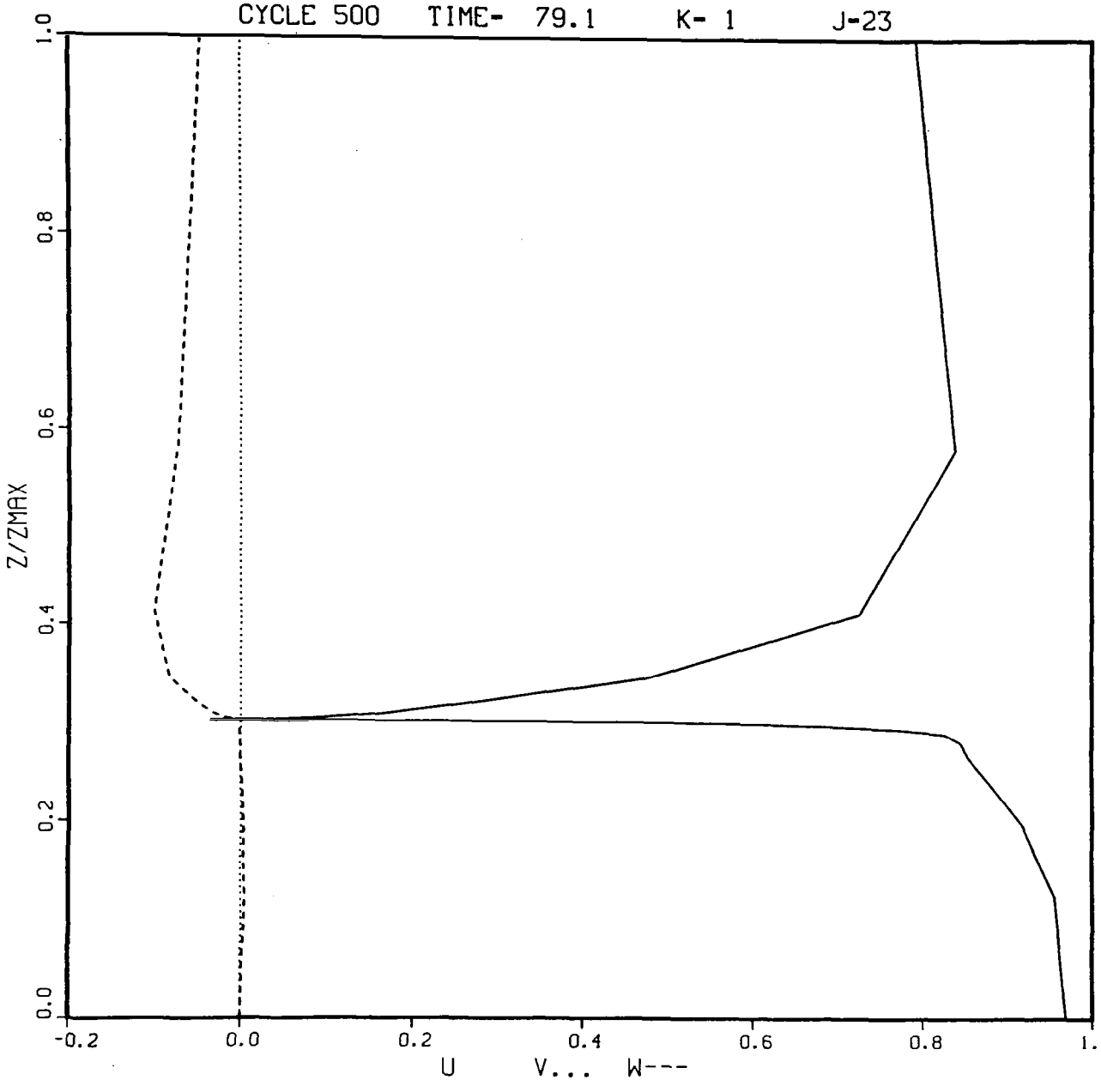

Figure 6-18 Velocity Profiles Along a Vertical Grid Line at Nozzle Exit Plane, x = 2.0

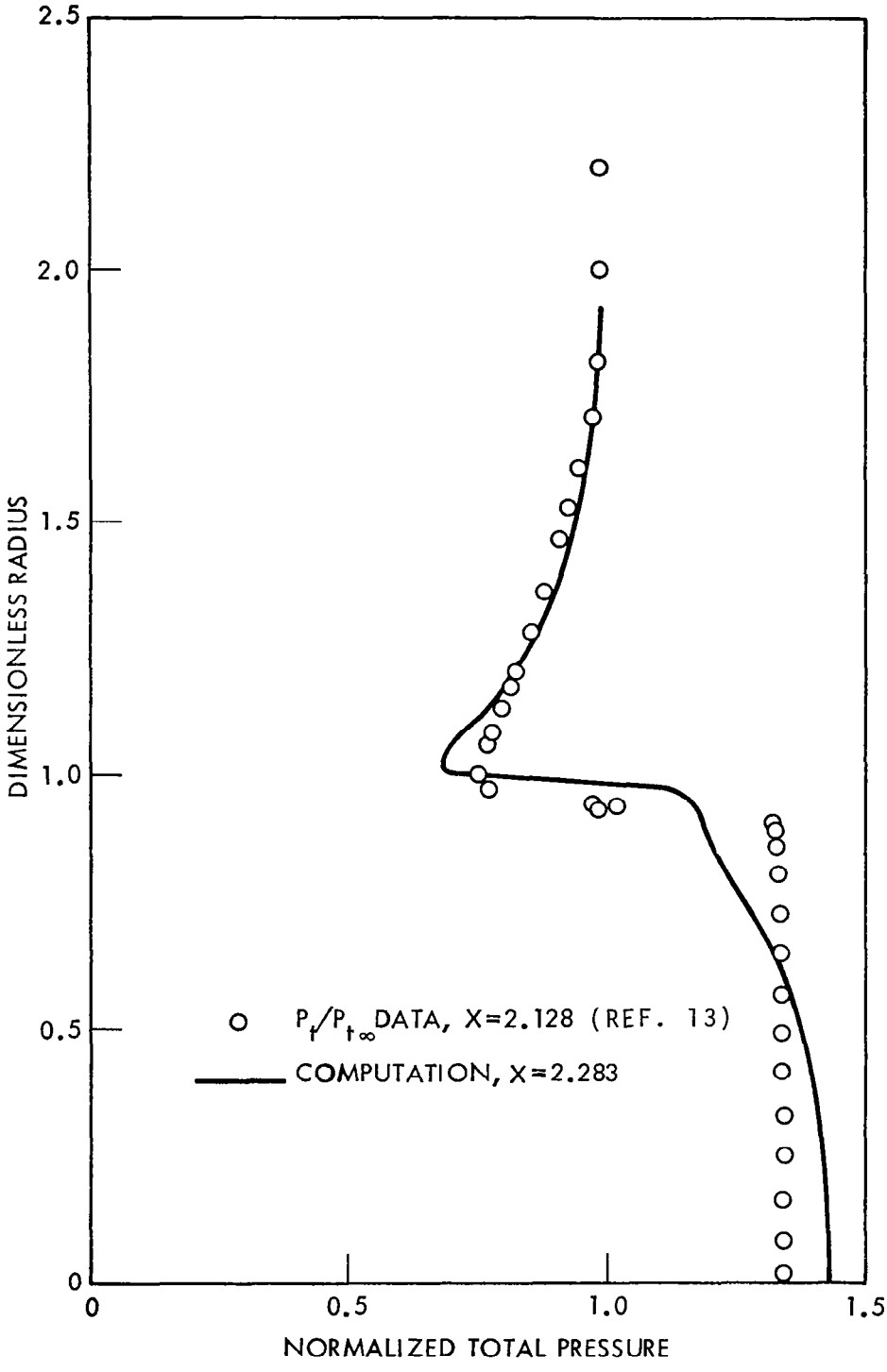

Figure 6-19a Comparison Between Experimental Total Pressure Probe Survey at x=2.128 With Normalized Total Pressure Profile Along the Nearest Vertical Grid Line

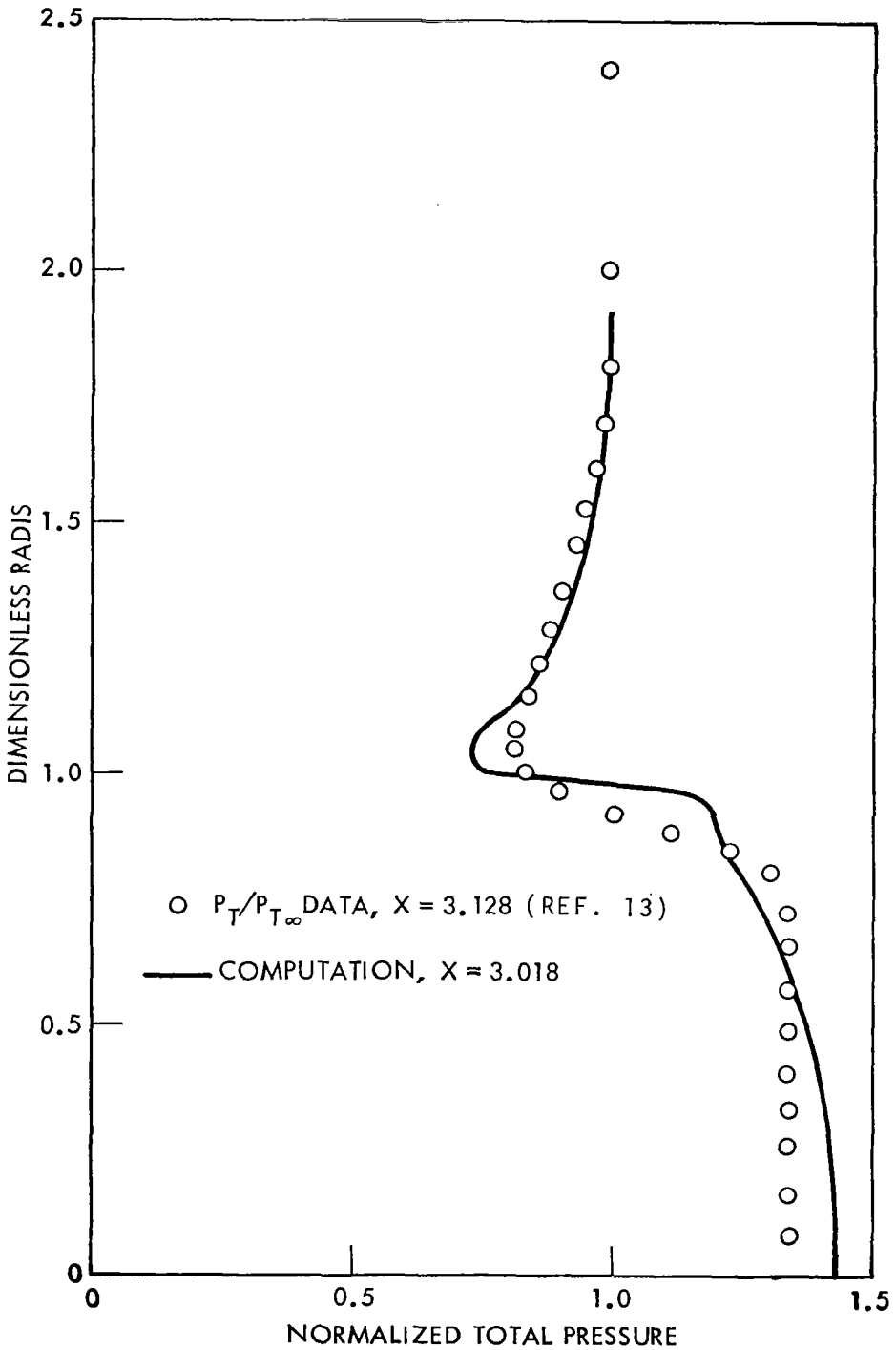

Figure 6-19b Comparison Between Experimental Total Pressure Probe Survey at x=3.128 with Normalized Total Pressure Profile Along the Nearest Vertical

Section 7

REFERENCES

1. Thomas, P. D.: Numerical Method for Predicting Flow Characteristics and Performance of Nonaxisymmetric Nozzles - Theory. NASA CR-3147, 1979.

2. Thomas, P. D.; and Lombard, C. K.: Geometric Conservation Law and Its Application to Flow Computations on Moving Grids. AIAA Journal, vol. 17, no. 10, Oct. 1979, pp. 1030-1037.

3. Steger, J. L.: Implicit Finite-Difference Simulation of Flow About Arbitrary Geometries. AIAA Journal, vol. 16, no. 7, July 1978.

4. Shapiro, Ascher H.: The Dynamics and Thermodynamics of Compressible Fluid Flow. Vol. I. Ronald Press Co., c.1953.

5. Franklin, P.: Methods of Advanced Calculus. McGraw-Hill, 1944, p. 123.

6. Baldwin, B. S.; and Lomax, H.: Thin Layer Approximation and Algebraic Model for Separated Turbulent Flows. AIAA Paper 78-257, Jan. 1978.

7. Schlichting, H.: Boundary Layer Theory. Fourth Ed. McGraw-Hill, 1970.

8. Thomas, P. D.; Neier, K. L.; and Middlecoff, J. F.: User's Guide for the NOZL3D Computer Program. NASA CR-159173, 1980.

9. Thomas, P. D.: Boundary Conditions for Implicit Solutions to the Compressible Navier-Stokes Equations on Finite Computational Domains. AIAA 4th Computational Fluid Dynamics Conference, Williamsburg, Va., July 1979.

10. Mason, Mary L.; Putnam, Lawrence E.; and Re, Richard J.: The Effect of Throat Contouring on Two-Dimensional Converging-Diverging Nozzles at Static Conditions. NASA TP-1704, 1980.

11. Reubush, David E.; and Runckel, Jack F.: Effect of Fineness Ratio on the Boattail Drag of Circular-Arc Afterbodies Having Closure Ratios of 0.50 With Jet Exhaust at Mach Numbers up to 1.30. NASA TN D-7192, 1973.

12. Abeyounis, William K.; and Putnam, Lawrence E.: Investigation of the Flow Field Surrounding Circular-Arc Boattail Nozzles at Subsonic Speeds. NASA TP-1633, 1980.

13. Mason, Mary L.; and Putnam, Lawrence E.: Pitot Pressure Measurements in Flow Fields Behind Circular-Arc Nozzles With Exhaust Jets at Subsonic Free-Stream Mach Numbers. NASA TM-80169, 1979.

1. Report No.	2. Government Accession No.	3. Recipient's Catalog No.
NASA CR-3264		

4. Title and Subtitle	5. Report Date
NUMERICAL METHOD FOR PREDICTING FLOW CHARACTERISTICS AND PERFORMANCE OF NONAXISYMMETRIC NOZZLES PART 2 - APPLICATIONS	October 1980
	6. Performing Organization Code
7. Author(s)	8. Performing Organization Report No.
P. D. Thomas	LMSC-D678888
	10. Work Unit No.
9. Performing Organization Name and Address	
Lockheed Palo Alto Research Laboratory 3251 Hanover St. Palo Alto, California 94304	11. Contract or Grant No. NAS1-15084
	13. Type of Report and Period Covered Contractor report
12. Sponsoring Agency Name and Address	
National Aeronautics and Space Administration Washington, DC 20546	14. Sponsoring Agency Code

15. Supplementary Notes

Contract Monitor: Lawrence E. Putnam, NASA Langley Research Center
Final Report

16. Abstract

The report summarizes work performed during the second phase of an effort to develop a computer-implemented numerical method for predicting the flow in and about an isolated three-dimensional jet exhaust nozzle. The approach is based on using an implicit numerical method to solve the unsteady Navier-Stokes equations in a boundary-conforming curvilinear coordinate system. Recent improvements to the original numerical algorithm are summarized. Equations are given for evaluating nozzle thrust and discharge coefficient in terms of computed flowfield data. The final formulation of models that are used to simulate flow turbulence effect is presented. Results are presented from numerical experiments to explore the effect of various quantities on the rate of convergence to steady state and on the final flowfield solution. Detailed flowfield predictions for several two-and three-dimensional nozzle configurations are presented and compared with wind tunnel experimental data.

17. Key Words (Suggested by Author(s))	18. Distribution Statement
Three Dimensional Flow Nonaxisymmetric Nozzles Numerical Flowfield Computation Navier-Stokes Equations	Unclassified-Unlimited Subject Category 02

19. Security Classif. (of this report)	20. Security Classif. (of this page)	21. No. of Pages	22. Price
Unclassified	Unclassified	115	A06

For sale by the National Technical Information Service, Springfield, Virginia 22161

NASA-Langley, 1980